

CURRENT FLOW THROUGH DISORDERED
NANOWIRE NETWORKS



Colin J. O'Callaghan

A THESIS SUBMITTED FOR THE DEGREE OF
DOCTOR OF PHILOSOPHY

SCHOOL OF PHYSICS
TRINITY COLLEGE DUBLIN

2018

CONTENTS

List of Figures	v
Acronyms	viii
1 INTRODUCTION	1
1.1 Nanowire Networks	2
1.2 Mathematical Description of Electrical Networks	6
1.2.1 Overview of Network Theory	6
1.2.2 Overview of Percolation Theory	7
1.3 Memristive Behaviour of Nanowire Networks	10
1.3.1 Overview of Memristance	10
1.3.2 Overview of Resistive Switching	13
1.3.3 Potential for Neuromorphic Computing	17
1.4 Thesis Scope	19
2 GENERAL THEORY AND MATHEMATICAL METHODS	21
2.1 Resistive Network Theory	22
2.2 Lattice Green's function for infinite resistive networks	27
2.3 Effective Medium Theory	36
2.4 Percolation Theory and Critical Wire Density	39
2.5 Junction density as a function of wire density and length	42
2.6 Chapter Summary	44
3 COMPUTATIONAL MODELS FOR DISORDERED NANOWIRE NETWORKS AND THEIR APPLICATIONS	46
3.1 Graphical Representations of Nanowire Networks	48
3.2 The Impact of Inner-wire Resistance	52
3.2.1 The Relationship Between Junction and Network Resistances .	53

3.2.2	The Effect of Nanowire Resistivity and Diameter on Network Resistance	56
3.2.3	The Impact of Wire Density on Nanowire Network Resistance	58
3.3	Digital Representation of Physical Nanowire Networks	61
3.4	Impact of Junction Resistance Disorder	68
3.5	Chapter Conclusion	70
4	EFFECTIVE MEDIUM THEORY FOR NANOWIRE NETWORKS	73
4.1	Inter-nodal Resistance in a Nanowire Network	76
4.2	Effective Medium Theory of a Nanowire Network	79
4.3	Inter-Electrode Resistance in a Nanowire Network	86
4.4	Application of the Effective Square Lattice	93
4.5	Conclusion	99
5	MEMRISTIVE PROPERTIES OF NANOWIRE NETWORKS	101
5.1	Modelling the Memristive Response of a Nanowire Junction	104
5.2	Memristance in a Nanowire Network	110
5.3	Current Colour Maps	118
5.4	Multi-terminal	122
5.5	Chapter Summary	126
6	COMPARISON OF A CAPACITIVE AND MEMRISTIVE JUNCTION ACTIVATION PROCESS	129
6.1	Capacitive Junction Model	132
6.2	Path Formation in Capacitive and Memristive Models	135
6.3	Scale Free Dynamics in Capacitive Activations	143
6.4	Fault Tolerance	146
6.5	Conclusion	152
A	DIGITISED NETWORK PARAMETERS	155
B	MULTI-NODAL ELECTRODES IN A SQUARE LATTICE	157
	BIBLIOGRAPHY	161

LIST OF FIGURES

Figure 1.1	Image: An SEM image of an Ag/PVP NWN	3
Figure 1.2	Sketch:	5
Figure 1.3	Sketch: A visualisation of a square lattice above and below the critical bond value	8
Figure 1.4	Plot: The memristance of a circuit element demonstrated by a hysteresis I-V curve and a tunable memristance where q is a state variable	13
Figure 1.5	Sketch: Bipolar and unipolar switching.	15
Figure 1.6	Sketch: Filament growth in an Ag ECM memristor cell.	16
Figure 1.7	Sketch: Filament growth in an Ag ECM memristor cell.	17
Figure 2.1	Sketch: network sketch	22
Figure 2.2	Sketch: Kirchhoff Sketch	25
Figure 2.3	Sketch: square lattice	28
Figure 2.4	Plot: Comparison between lattice integral and its approximation	35
Figure 2.5	Sketch: square Kirchhoff Integral	36
Figure 2.6	Sketch: emt theory sketch	37
Figure 2.7	Sketch: Binary Distribution	40
Figure 2.8	Sketch: cluster sketch	41
Figure 2.9	Plot: The relationship between junction density with wire density and a demonstration of finite-size effects.	44
Figure 3.1	Schematic: JDA and MNR Sketch	49
Figure 3.2	Sketch: Visualisation of simulated nanowire network.	52
Figure 3.3	Plot: Junction Resistance	53

Figure 3.4	Plot: Resistivity Parameters	57
Figure 3.5	Plot: Wire density	60
Figure 3.6	Plot: Digitised NWN	62
Figure 3.7	Plot: MNR JDA	64
Figure 3.8	Plot: Junction Resistance Distribution	66
Figure 3.9	Plot: Gamma Junction Resistance	67
Figure 3.10	Plot:	69
Figure 4.1	Sketch: NWN image to effective mapping	74
Figure 4.2	Sketch: Nodal Separation	77
Figure 4.3	Plot: Inter-node Resistance	78
Figure 4.4	Sketch: Types of resistors in a nanowire network.	80
Figure 4.5	Plot: EMT Relative Percentages	82
Figure 4.6	Plot: Inter-nodal Resistance EMT	85
Figure 4.7	Plot: Inter-electrode Resistance versus electrode nodal separation	88
Figure 4.8	Plot: Ny Dependence	90
Figure 4.9	Plot: N_x versus electrode separation and wire density	92
Figure 4.10	Plot: EMT applied to wire density and length scaling	95
Figure 4.11	Plot: Resistance parameters	96
Figure 4.12	Plot: Effective Square Lattice Applied to a NWN	98
Figure 4.13	Plot: Effective Square Lattice Applied to Optimization-Capacity Coefficient	99
Figure 5.1	Plot: Conductance of a nanowire junction and network versus increasing current compliance.	105
Figure 5.2	Plot: Single Junction Parameter Response	108
Figure 5.3	Diagram: Workflow diagram of memristive model simulation	112
Figure 5.4	Plot: SEM and digitised Image of a NWN	113
Figure 5.5	Plot: Exponent fit	115
Figure 5.6	Plot: Scaling Regimes	118

Figure 5.7	Plot: Conductance curves and Current Maps for Difference Exponents	120
Figure 5.8	Plot: Current maps	121
Figure 5.9	Image: A Passive Voltage Contrast image of a NWN evolved to a plateau in conductance	123
Figure 5.10	Plot: Multi Terminal Sketch	124
Figure 5.11	Plot: Memory state in multi-terminal	125
Figure 6.1	Sketch: A sketch of memristive and capacitor nanowire junctions in a network along with passive voltage contrast images of nanowire networks displaying a capacitive and memristive response.	130
Figure 6.2	Schematic: A work-flow diagram of the capacitive junction model.	134
Figure 6.3	Plot:	135
Figure 6.4	Plot:	137
Figure 6.5	Sketch:	139
Figure 6.6	Plot:	141
Figure 6.7	Sketch:	142
Figure 6.8	Sketch:	144
Figure 6.9	Sketch:	148
Figure 6.10	Sketch:	150
Figure 6.11	Sketch:	151

COMMON ACRONYMS

NWN Nanowire Network

1

INTRODUCTION

In this thesis the nature of current flow through randomly orientated nanowire networks is studied with computational and theoretical techniques, all of which are described in detail. This current flow is examined in two main cases; first where the network resistors are static and are relatively homogeneous in nature, this is discussed in chapters three and four of the thesis. In the second case, the networks change in resistance according to the current flow through the network according to a phenomenon known as memristance, and is detailed in chapters five and six.

Due to the random nature of nanowire network connectivity numerical simulations are necessary to achieve an understanding of the properties of nanowire networks and feature heavily in this thesis. Although numerical analysis provides an excellent lens through which the nanowire networks can be examined, some of the relationships between parameters of a network are best articulated with a mathematical framework. As such this thesis strives to develop comprehensive theoretical descriptions of nanowire networks in places and uses them in conjunction with numerical simulations to illustrate various properties of nanowire networks.

In this chapter an introduction to nanowire networks is provided by discussing their fabrication, properties, and applications. A common application of a nanowire network is as a transparent conductor and the potential of nanowire networks is discussed in section 1.1. In section 1.2 an introduction to the mathematical descriptions of nanowire networks is presented, namely network and percolation the-

ory. The potential memory and computing applications of nanowire networks is then introduced in section 1.3 through a discussion of the exciting field of resistive switching and memristive materials and how these properties have been noted in nanowire networks. Finally the scope of the thesis is described in more detail in section 1.4.

1.1 NANOWIRE NETWORKS

The ability to manipulate our environment and materials to achieve a desired functionality is a human trait that has driven the ever increasing complexity of our society for milenia. Over the past several thousand years the pace of societal and technological innovation has grown exponentially, requiring ever more sophistication to continue this growth. Today advancement continues in nearly every aspect of our lives at a rate unfathomable to our ancestors. Central to our current technological development is our ability to create the necessary tools, linking technological advancement with the current level of material manipulation we are capable of. That being the case we are truly living in the nano-materials age, were we have controlled and deliberate manipulation of materials on the nanometer scale. Nanoscience's reach is vast, covering disciplines as diverse as cellular biology to renewable energy.

Nanomaterials are known to have very different physical properties to their bulk counterparts. The source of this difference is essentially due to confinement of electrons in the material to a small crystall lattice resulting in a behaviour not seen in a large continuous medium. Confined nanoparticles can be grouped into three classes; pseudo zero dimensional materials of a small number of atoms referred to as quantum dots¹, one dimensional objects that are extended in two dimensions and referred to as nanowires or nanotubes^{2,3}, and two dimensional objects that are a plane a few atoms thick such as graphene⁴ and MoS₂^{5,6}.

The first report of a metallic nanowire network was made by Adelung et al in 1999, reporting in their seminal work the ease, speed and scale of the fabrication technique used to create the nanowire network. Networks were formed by adsorbing nanowires onto areas of induced strain on an extremely flat surface resulting in networks only bounded by the size of the surface². The reports of networks comprised of one dimensional nanomaterials has grown quickly since then, the variety in the comprising material and fabrication techniques expanding alongside this. Among the common materials used in nano-networks are metallic core-insulating shell nanowires⁷⁻⁹, semiconducting nanowire¹⁰ and Carbon nanotubes^{11,12}. The fabrication techniques include, but are not limited to; spray deposition¹³⁻¹⁵, drop casting¹⁶, spin coating¹⁷, Mayer rod coating¹⁸, inkjet printing¹⁹, and roll to roll printing²⁰. Each technique has its merits but spray coating in particular leads to a very homogeneous network, is scalable and can be performed under normal atmospheric conditions²¹. Figure 1.1 presents an SEM image of an Ag/PVP core shell NWN that was spray deposited between two electrodes that span the network on both sides.

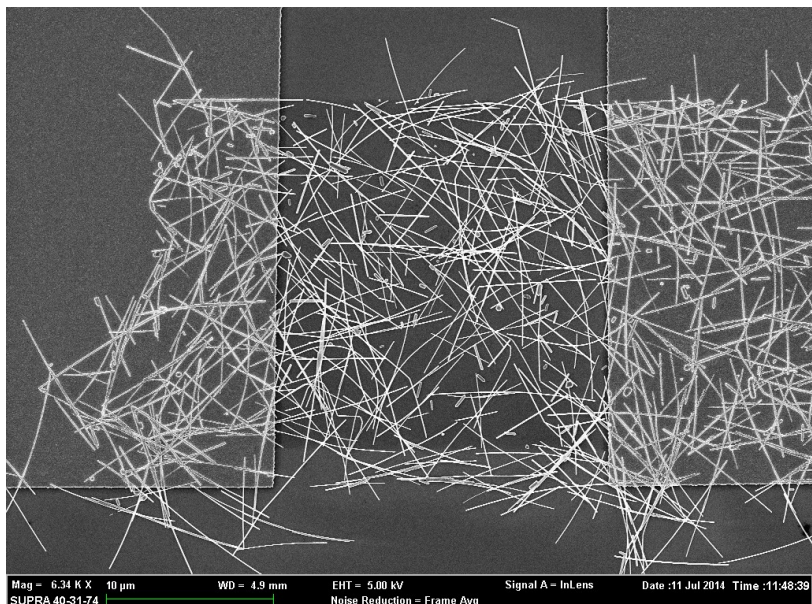


Figure 1.1: An SEM image of an Ag/PVP NWN that was spray deposited between two electrodes. NOTE, GET ONE FROM OUR PAPERS.

Thin films that couple high electrical conductivity and optical transparency are crucial in a number of applications. Currently the market is dominated by transparent conducting oxides, in particular Indium Tin Oxide and Florine doped Tin oxide²². There are three major drawbacks with incorporating Indium Tin Oxide into transparent conductors. Firstly Indium itself is relatively scarce. Though it has a similar abundance in the Earths crust as Silver, roughly 50 parts per billion, it has few common minerals and is produced as a by product of Zinc refinement. The second issue with Indium Tin Oxide is brittleness, a limiting factor in its inclusion in flexible transparent conductors a market that is expected to grow in the coming years. Finally the deposition of Indium Tin Oxide onto a substrate is performed using sputtering techniques, where material is deposited onto a target substrate as a vapor. This requires high temperatures and results in slow deposition rates. Furthermore a large deal of the vaporised Indium Tin Oxide does not deposit on the target substrate requiring recapture methods that further add to the expense and time in transparent conductor production. Metallic nanowire networks address many of these issues.

A particularly exciting property of nanowire networks is their high transparency and high attainable conductivity^{23,24}, with properties similar to those of Indium Tin Oxide attainable^{25,26}. Fabrication techniques of nanowire networks are scalable and inexpensive, and nanowire networks have been shown to be very flexible while maintaining their desired properties. It is unsurprising that their potential as transparent conductors has largely driven their development over the past two decades^{21,27,28}. This development has lead to nanowire networks being incorporated into and LED displays^{29,30}, and thin film solar cell^{24,31–33} where they have been shown to have excellent performance similar to Indium Tin Oxide devices.

It has been shown by Madaria et al that Silver NWNs can remain conductive when bent up to 160 degrees and returned to their original sheet resistance when the bending stress was removed³⁴. Lim et al⁷ examined various mechanical properties of Ag NWNs. NWNs were bent, twisted and put under torsional stress

with little change in sheet resistance. This flexibility of nanowire networks makes them ideal candidates for the development of flexible transparent conductors which could be used to develop flexible displays or incorporated into wearable devices^{21,28}.

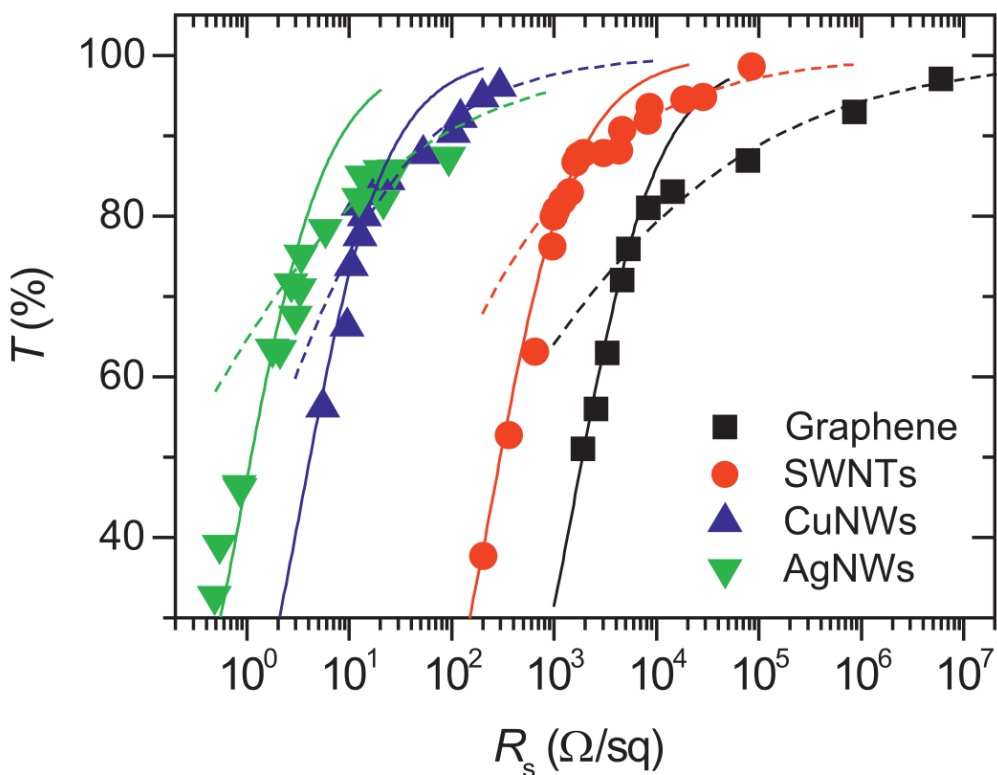


Figure 1.2: The transmittance of a number of different transparent conductors made from different materials was compared with their respective sheet resistance by De et al³⁵. Points are fit to expressions describing the percolation regime (dashed line), or low wire density regime, and the bulk regime (solid line). NOTE: Do a plot that puts the transmission/resistance needed on this plot.

Besides their applications as transparent conductors nanowire networks have properties that allow for various applications. Many examples of nanowire network based transparent heaters, necessary for anti-fog windows, are found in the literature^{36–38}. The scalable fabrication processes such as spray deposition enable large scale surface deposition of nanowires meaning that large curved surfaces can easily be coated in nanowires to form a transparent heater. Nanowire networks have also been successfully applied to non-optical devices such as sensors^{39,40}, and

fuel cells^{41–43}. The many applications of one-dimensional nanomaterial networks has necessitated theoretical descriptions of their properties in order to understand the required alterations to a network such that a desired property is achieved.

1.2 MATHEMATICAL DESCRIPTION OF ELECTRICAL NETWORKS

Here an overview to some of the mathematical fields that are used to calculate the resistances of nanowire networks are discussed. Not much detail on the mathematics are given in this section, see chapter 2 for a more comprehensive discussion.

1.2.1 *Overview of Network Theory*

Network theory has its roots in the early 18th century where, unsurprisingly for the time, Euler played a key role in its early development. A well known problem of the day was the "Seven Bridges of Königsberg", where it hypothesised if a route was possible that crossed the seven bridges in the city exactly once. Euler solved the problem using a method that sowed the seeds to what would become graph theory, of which network theory is a subset.

A network is a collection of nodes that are connected in some way by network edges, the network may represent some physical entity such as bridges and routes between them as in the seven bridges of königsberg problem, or a more abstract construction such as people and their inter-personal relationships in a social network or agents and transactions in an economic network⁴⁴. Network theory is concerned with the study of these representaions of relations between objects. Among the many applications of network theory, we shall focus on transport of an entity through a network. In this thesis the transported entities are current and charge,

the associated mathematics are given in chapter 2 and can be applied to other transport problems such as heat and mass.

A host of many-body problem can be abstracted into a network form where nodes are individual particles and edges are the inter-body interactions. These class of problems can be simplified massively by making use of underlying system symmetries. For example, consider a tight-binding model applied to an infinite periodic lattice, the electron density of states of such a system is solved using Fourier transforms along the directions of symmetry. The same thinking can be applied to resistive lattices and in chapter 2 Cserti's method for calculating the inter-node resistance in an infinite resistive lattice is presented⁴⁵.

Network theory can be applied to NWNs to calculate their electrical properties with an appropriate mapping between the NWN and the mathematical network. In chapter 3 mapping's between a nanowire network and a mathematical network are introduced and are then solved using the network transport mathematics layed out in chapter 2. Due to the spatial randomness associated with nanowire networks, there are no symmetries to exploit in order to create an analytic function capable of solving the resistive properties of a network like the method outlined by Cserti⁴⁵. As shown in the previous section many applications of nanowire networks require specific sheet resistances and optical transmission values. Traditionally the use of empirical models derived from percolation theory has been used to approximate the average effect of changing say wire density on the sheet resistance of an ensemble of networks⁴⁶.

1.2.2 *Overview of Percolation Theory*

Percolation theory is concerned with the behaviour of connected clusters in a network. In 1957 Broadbent and Hammersley introduced the concept of modeling how a fluid percolates through a porous medium, drawing analogy with electrons flowing through a lattice or disease through a population. As opposed to a diffu-

sive process, where the particles themselves are a source of stochasticity as they move through a medium, they defined a percolative process as where the medium is the source of stochasticity and completely determine the movement of particles through them⁴⁷. To model the porous material as a percolative process consider a square lattice of size $n \times n$ nodes, each node has four nearest neighbours. The nearest neighbour edges were connected with some probability p or no connection existed with some probability $1 - p$. There exists some bond probability p_c at which there exists a connecting path between the two extreme ends of a network, below $p_c = 0.5$ no path exists. Figure 1.3 is a visualisation of a percolative square lattice the $p > p_c$ and $p < p_c$. The blue lines on either side of the two lattices represent the two edges between which we wish percolation to occur and the blue lines between nodes are connecting edges.

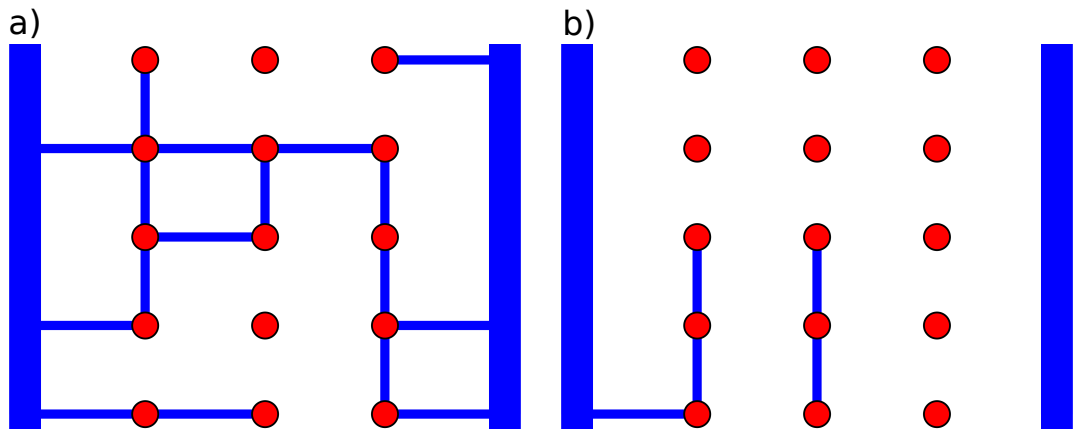


Figure 1.3: (a) A sure lattice with nodes depicted as red circles and connecting edges as blue lines. The edges between nearest neighbours exist with a probability $p = 0.6$ which is greater than the critical probability $p_c = 0.5$ for a square lattice. (b) a square lattice where the edges between nearest neighbours exist with a probability $p = 0.3$ which is less than the critical value and so a percolating path across the network does not exist.

In a 1973 paper, Pike and Seager extended the concept of percolation theory to random networks formed by different objects that were randomly distributed and connected over a defined two dimensional area⁴⁶. This is a departure from previous works where the positioning of nodes and edges were fixed but their

existence was given by some probability distribution. Among the many types of objects studied the percolative characteristics of one dimensional objects (sticks) were studied. Here the requirement for a connection to form between two sticks requires their centers to lie within a distance ℓl of one another, ℓl being the length of the sticks, and that their orientations are such that they intersect. Pike and Seagar used percolation theory showed that the critical density of 2D randomly oriented sticks ($(n_w)_c$) is calculated using the expression expression

$$(n_w)_c l^2 = Q \quad (1.2.1)$$

Where Q is a constant. The stick percolation model is a direct description of percolation in nanowire networks.

Percolation theory has been used to explain the global properties of a network of conducting wires, much the same as a nanowire network. The scaling between sheet conductance Γ_s and the wire density follows a power law in the following form

$$\Gamma_s \propto (n_w - (n_w)_c)^{-t} \quad (1.2.2)$$

This scaling only holds for wire densities near to the critical value $(n_w)_c$. For wire densities in the criticality region, where $n_w \approx (n_w)_c$, Li and Zhang have shown $t \approx 1.280 \pm 0.014$. For wires densities beyond the criticality region, Li and Zhang have shown that the conductivity exponent t depends on both the junction resistance R_j and the intra-wire resistance $R_i = \rho l$ where l is the length of each wire in the system, and ρ is the resistivity per unit cross sectional area⁴⁸. At large wire densities Žeželj and Stanković⁴⁹ have shown that exponents also have a dependence on wire density as well as the ratio of R_j and R_i and can vary between $1 < t < 2$ for large wire densities.

The empirical nature of percolation scaling laws are a central frustration with using percolation theory to describe the conductive properties of nanowire net-

works. The relationship between the sheet resistance and the base properties of the nanowire such as wire length, junction resistance, wire resistivity and so on, are not clear. Empirical models specific to one parameter that hold over a certain range of wire densities and wire lengths are not suitable for a field poised to play a large role in many industries. This brings us to a goal of this thesis, that is to develop an approximation for the sheet resistance of a nanowire network in terms of all of the nanowire properties. This approximation is presented in chapter 4.

1.3 MEMRISTIVE BEHAVIOUR OF NANOWIRE NETWORKS

Until now the discussion of NWNs has considered static networks where the resistive elements are unchanged by current flow. Recently it was shown that under certain circumstances NWNs have a memristive response to current-flow⁵⁰, that is their resistance changed according to the current flow through the network. Here is an overview of memristance and how it pertains to NWNs.

1.3.1 *Overview of Memristance*

In 1971 Leon Chua introduced the concept of a memristor, a memory-resistor, by characterising the relationship between the charge $q(t) = \int_{-\infty}^t I(\tau) d\tau$ and the flux-linkage $\phi(t) = \int_{-\infty}^t V(\tau) d\tau$ where I and V are the current and voltage respectively⁵¹. Chua argued that by symmetry there ought to be a fourth nonlinear fundamental circuit element, the others being a resistor, capacitor and an inductor,

and that the memristor was the fourth such element. The memristance of a system M is related to the voltage and magnetic flux-linkage as

$$M = \frac{d\phi}{dq} \quad (1.3.1)$$

$$M(q(t)) = \frac{d\phi/dt}{dq/dt} = \frac{V(t)}{I(t)} \quad (1.3.2)$$

Here by expanding on the definition of a memristor one finds that it will take the form of resistance and since $q(t)$ and $\phi(t)$ are time dependent integrals, M is not constant and is in fact a tunable resistance depending on the history of applied current and voltage.

For example⁵², consider the relationship between charge and flux in a memristive device and a sinusoidal applied current

$$\phi(q) = q + \frac{q^3}{3} \quad (1.3.3)$$

$$I(t) = A \sin(\omega t) \quad (1.3.4)$$

Performing the time integral for the cumulative charge we obtain

$$q(t) = \int_{-\infty}^t A \sin(\omega \tau) d\tau = \frac{A}{\omega} (1 - \cos(\omega t)) \quad (1.3.5)$$

The link-flux is then obtained from equation 1.3.3.

$$\phi(t) = \frac{A}{\omega} (1 - \cos(\omega t)) \left(1 + \frac{A^2}{3\omega^2} (1 - \cos(\omega t))^2\right) = \quad (1.3.6)$$

The voltage across the system is the time derivative of the flux.

$$V = \frac{d\phi}{dt} = M(q(t))I(t) \quad (1.3.7)$$

After performing the time derivative the memristance of the circuit element can be isolated as $M(q) = 1 + q^2$ or

$$M(q(t)) = 1 + \left(\frac{A}{\omega} (1 - \cos(\omega t)) \right) \quad (1.3.8)$$

An I-V curve of a memristive system from this example with $\omega = A = 1$ can be seen in Figure 1.4(a), the non-constant memristance is captured by the hysteresis curve. The relationship $M(q) = 1 + q^2$ which is plot in Figure 1.4(b) and shows that memristance is finite for finite charge, which in turn means for finite current flow. Taken in conjunction with equation 1.3.2 the voltage over a memristor is zero for zero current flow, giving the pinched hysteresis I-V curve seen in Figure 1.4(a). This relationship between the memristance and charge is also shows that the memristance can be tuned to any level⁵². Since charge is the deciding factor in the elements memristance it is referred to as a state variable and by simply sending current pulses through the memristor its value can change accordingly. Here the memristance of an element can be captured with the state equations;

$$V = M(w)I \quad (1.3.9)$$

$$\frac{dw}{dt} = I \quad (1.3.10)$$

where the state variable w is the charge in what shall be referred to as an ideal memristor.

Chua and Kang generalised the concept of a memristor to have a number of state variable that need not be the charge through the system

$$V = M(w, I)I \quad (1.3.11)$$

$$\frac{dw}{dt} = f(w, I) \quad (1.3.12)$$

where w is the set of state variables and the functions $M()$ and $f()$ can be explicit functions in time⁵³. With this generalised definition of memristance that did not

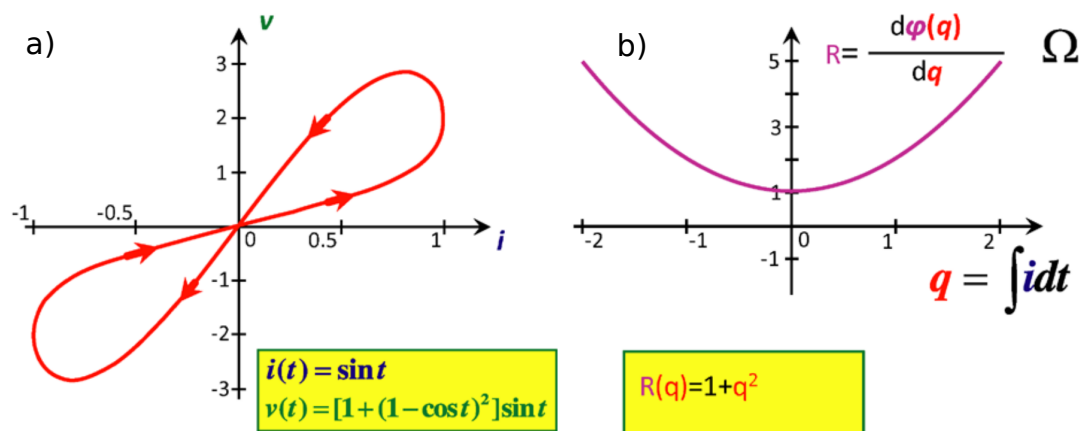


Figure 1.4: (a) An I-V curve for the memristor determined by equations 1.3.3 and 1.3.4 with $A = \omega = 1$ that displays the pinched hysteresis curve characteristic of memristors . (b) Visualisation of relationship 1.3.8 and shows the tunability of the resistance in a network. Adapted from Chua⁵².

explicitly depend on the charge as a state variable a host of materials undergoing a phenomena known as resistive switching were classified as memristors⁵².

1.3.2 Overview of Resistive Switching

The concept of a non-constant resistive devices not an entirely novel idea in physics. Resistive switching devices, capable of cycling between a High Resistance State (HRS) and a Low Resistance State (LRS), is a rich and active field of research. In 2008 Strukov et al first identified that a resistive switching material could be related to a memristor⁵⁴ for the first time, linking the two fields. The force driving much of the development of redox reaction resistive switching devices is their potential for memory devices, which have come to be labeled as ReRAM devices. ReRAM devices have been shown to have excellent physical properties for memory applications^{55,56}; high area compaction^{40,57}, high state switching speeds (< 100 ps)⁵⁸, good state retention times (100's years)^{59,60}, high switching endurance ($> 10^{12}$)⁶¹, and low power consumption^{55,62}. Perhaps the most important listed property of the

resistive switching, or memristive, devices is their scalability. Traditional silicon transistor technology is fast reaching the natural barriers that quantum mechanics pose, thus threatening the exponential growth in memory storage the industry has strived for over the past decades and ReRAM devices could exceed these spatial limitations.

A common architecture for a memristor is two metallic layers separated by an insulating barrier, referred to as a metal-insulator-metal (MIM) device. The mechanism that regulates the memristive response depends on the material characteristics of the device. Examples of memristive materials⁵⁵ are transition metal oxides, amorphous-to-crystal phase materials such as GeSbTe, and polymeric matrices sandwiched by metals (e.g. Ag/PVP plates). During the breakdown of a MIM junction, the growth of a conducting filament bridging the metal plates takes place and this can be regulated by distinct mechanisms^{57,63–66} including thermochemical (TCM), electrochemical metallisation (ECM), and valence change (VCM). With the gradual filament growth, a drastic reduction in the characteristic resistance of the junction can be measured. By controlling the current flow through the device the conductive filament can be forced to rupture and is the source of the reversability in resistive switching devices.

Two common switching dynamics of a memristive junction are unipolar and bipolar resistive switching. Figure 1.5 presents I-V sweeps for ideal unipolar and bipolar switching devices. Unipolar switching occurs when the transitions between HRS and LRS have the same polarity, whereas in bipolar switching the opposite polarity is required to rupture the filament. Also shown in Figure 1.5 is the current compliance, I_{cc} , that is set in experiments as an upper limit to current flow in I-V sweeps. This is to protect the junction from large current flows which can cause an irreversible change to the junction.

In electromechanical metallisation (ECM) memristors the conductive filament is built between the metallic layers by means of cation transport. Various other names have been associated with this form of memristor, mainly conductive bridge ran-

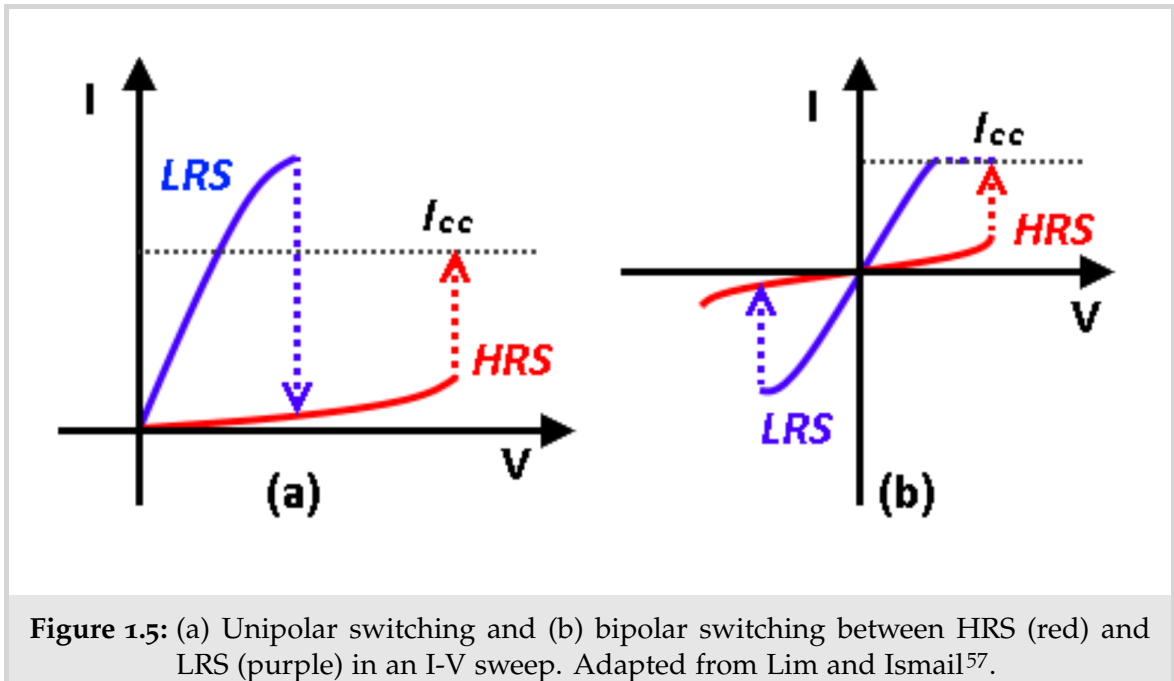


Figure 1.5: (a) Unipolar switching and (b) bipolar switching between HRS (red) and LRS (purple) in an I-V sweep. Adapted from Lim and Ismail⁵⁷.

dom access memory (CBRAM) and programmable metallisation cell (PMC). Here a highly electromobile metal electrode such as Cu or Ag, known as the active electrode, acts as the source of material for the conductive filament that nucleates on the opposite electrode and grows back towards the cathode. Figure 1.6 presents a sketch of an Ag/Pt ECM cell at various stages of conductive filament growth and the associated I-V sweep for the device⁶⁶. In panel (a) the electric field is sufficient to cause Ag cations to begin to migrate through the insulating layer to the counter electrode and grow a conductive filament back towards the active electrode. This is referred to as the SET procedure. The device is limited to a current compliance shown as the dashed horizontal line and a conductive filament that has bridged the inter-electrode insulator is shown in panel (b), the memristor is now in an ON state. The current is driven at the opposite polarity and the conductive filament ruptures with some of the Ag atoms returning to the active electrode in the RESET procedure, a visualisation of this is in panel (c). The pristine memristor is shown in panel (d) that shows no filament formation has begun, and is labelled as the OFF state.

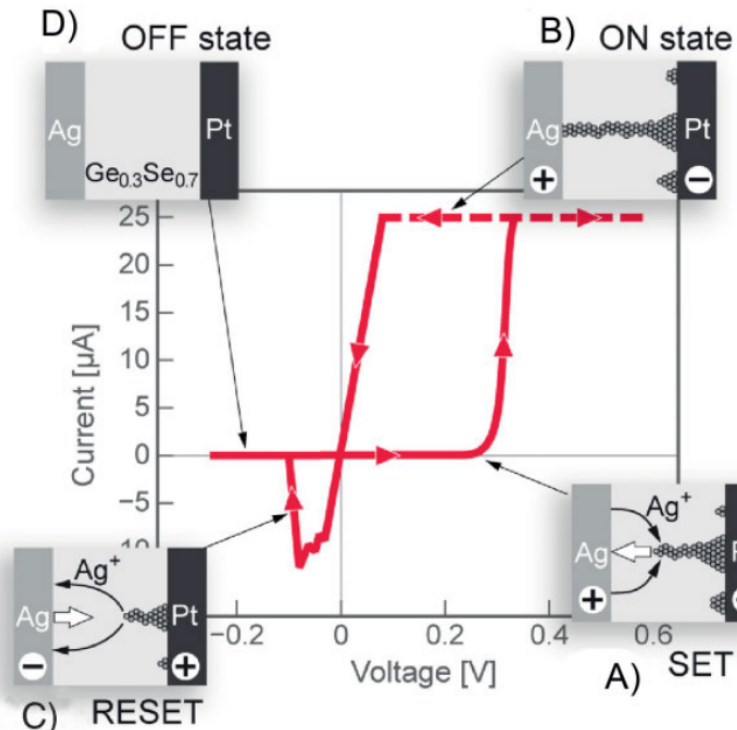


Figure 1.6: An I-V sweep measurement taken on a bipolar Ag/Pt memristor ECM cell with a $\text{Ge}_{0.3}\text{Se}_{0.7}$ inter-electrode insulator. The panels (a)-(d) are sketches of the state of the conductive filament at various stages in the I-V curve. Adapted from Waser⁶⁶

The observation of a conductive filament growth was reported by Yang et al where Ag filaments were observed in an Ag active electrode, Pt inert electrode system and are shown in Figure ??⁶⁷. In panel (a) the device is imaged after a forming process, and in the insulating gap between electrodes several distinct filaments are observed, most notably the topmost filament which appears to span the insulator. A zoomed image is presented in the red square of this particular filament at the inert electrode interface. In panel (b) the filament was ruptured electrically which is evidenced in the zoomed area of the filament near the electrode which are no longer connected.

In valance change mechanism (VCM) devices the memristanc is mediated by field-assisted migration of oxygen anions in transition metal oxides and the resulting valance change of the cation sublattice⁶⁶. The active material are transition

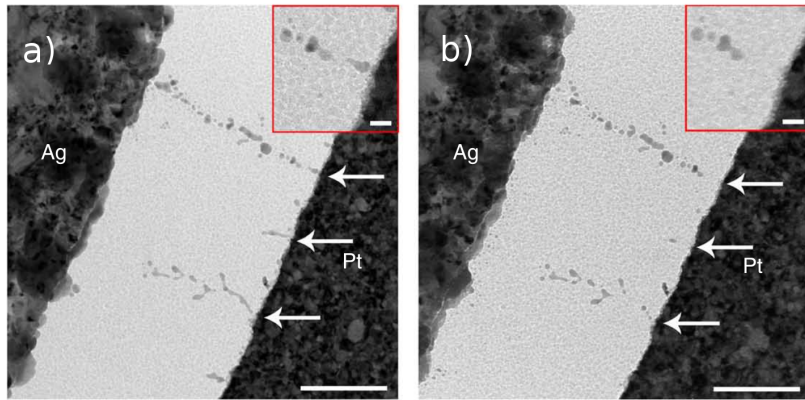


Figure 1.7: Experimental observations of conductive filament growth in an Ag/Pt memristive ECM cell. The thin linear structures highlighted by arrows in (a) are the Ag filaments growing from the Pt electrode towards the Ag electrode. A zoomed image of the top filament is shown in the red square showing a connection with the Pt electrode. (b) The filament after a RESET operation was performed on the device. The filaments have shrunk and in the case of the longest has ruptured the connection between electrodes. The zoomed area shows no connection with the Pt electrode. Adapted from Yang et al⁶⁷.

metal oxides, common examples are HfO_x , SrTiO_3 , ZNO, AlO_2 , and TiO_2 ^{62,68}, in fact it was a TiO_2 based device that was first linked to memristance by Strukov et al⁷. The thermochemical mechanism (TCM) for memristance is based on stoichiometry change and redox reactions in the oxide layer due to current induced heating⁶⁹. As it is predominantly Ag nanowire networks that shall be discussed in this thesis we shall focus on conductive filament formation as the mediator of a memristive response in a NWN.

1.3.3 Potential for Neuromorphic Computing

Asides from ReRAM applications, memristors have potential as central components in other novel devices such as multi-bit memory storage and neuromorphic computation due to their tunable resistance levels. Neuromorphic computing aims to mimic brain-like computation. The brain is a highly complex machine formed by

billions of neurons which are disorderly interconnected by trillions of synapses. Our brain has unique abilities that outperform by far the fastest computers on the planet such as ultra-fast sensory processing, high-level pattern recognition, and the ultimate skill of learning from experience. Brain activity is also incredibly energy-efficient; it consumes about 20 W, equivalent to a dim light bulb⁷⁰. To date there has been numerous attempts to mimic biological computation through simulation on traditional Von Neumann computer architectures⁷¹. However this approach is computationally expensive and thus energy intensive. Another approach to achieve biological computation is through the use of neuromorphic computing architectures^{55,72}. These are decentralized networks of memristor or analogue synapses. While these architectures are much more energy efficient, the fabrication of such devices can be quite difficult, often requiring exact engineering of individual memristor components and connections. A high level of component homogeneity and regularity in neuromorphic networks may not be required as the variability, stochasticity and component reliability which are becoming increasingly difficult to overcome in traditional computing technologies do not pose as big a problem to biological computing systems⁷³. Indeed the variability of individual synapses and the complexity of the global synapse network are exploited to perform robust and reliable computations, all while using a fraction of the power that a Von Neumann computer would need for similar performance. Such attributes have inspired the creation of the neuromorphic devices that have the potential to revolutionize computing technology with the next-generation of microprocessors that will mimic brain functions⁷⁴⁻⁷⁸.

A nanowire network is essentially a collection of highly connected metal-insulator-metal junctions. As stated previously nanowires are coated in a insulating material to prevent flocculation in solution. Usually NWNs are annealed to remove the insulating barrier separating the metallic nanowire cores in order to maximise the optoelectrical properties of the network leaving a NWN with a non-varying high conductance⁷⁹. However this discussion on memristance suggests that nanowires

have a memristive response to current flow and should lead to interesting collective behaviour in a NWN. In fact the dynamic response of NWNs to current has been previously reported, Nirmalraj et al reported the tunability of Ag NWN conductivity with current flow⁸⁰ but the link with memristive devices was not made at the time. A memristive NWN has much potential for memory devices as discussed above and in brain-like neuromorphic computing, and their properties are discussed in more detail in chapters 5 and 6.

1.4 THESIS SCOPE

A brief overview of the field of nanowire networks has been presented in this chapter and provides context for the work that will be discussed in subsequent chapters. The main goal of this thesis is to describe how current flows through disordered nanowire networks at various current levels and how various properties of nanowire and their junctions impact this. The nanowire networks can either be static, i.e. unchanging, in response to current flow or have a dynamic response to electrical current.

In chapter 2 the background theory and mathematical methods used throughout this thesis are introduced. The rest of the thesis can be broken into two sections, the first of which deals with annealed networks with very low fixed junction resistances towards their use as transparent conductors. Chapter 3 presents two mappings between a nanowire network onto a graphical representation such that the electrical properties of a network can be calculated using network theory. One of the mappings only considers inter-wire junctions as a source of resistance in a network while the other also considers the resistance of nanowires themselves and so its impact on network conductance can be examined. A method to digitise nanowire network geometry is also introduced, removing the spatial randomness from comparisons between experimental measurements and computer simulations.

These comparisons were used to approximate the junction resistance of Ag/PVP nanowires. In chapter 4 an approximation for the sheet resistance of a nanowire network in terms of all of the nanowire properties is presented. To achieve this analytical expressions are derived to determine the number of resistive elements in a network which is used to calculate an effective medium for a NWN. The approximation is successfully used to estimate the ultimate conductivity attainable if the network's junctions are annealed to perfect conductors, highlighting the speed of estimating such network properties compared with previous simulation techniques.

The second part to this thesis deals with unannealed nanowire networks whose inter-wire junctions are extremely resistive in low current regimes but can respond dynamically to current flow. In chapter 5 the junctions are shown to behave as memristive elements in response to low currents. The properties of a network of such memristive junctions is shown to behave similarly to the nanowire, representing an emergent self-similarity between the network and the junctions. A multi-electrode device is simulated operating in the memristive model and highlights some important properties that could be exploited for neuromorphic applications. The memristive response is compared with a capacitive junction model that applies to negligible current ranges in chapter 6. The two models for the activation of models are shown to be very different with the capacitive model displaying scale-free complex dynamics and both having different levels of fault tolerance. Chapter 7 contains a thesis conclusion as well as future research that follows the results of this work.

2

GENERAL THEORY AND MATHEMATICAL METHODS

In this chapter, the general methodology and theory that will be used to study nanowire networks throughout this thesis will be introduced. To frame the mathematical description of nanowire networks some fundamental aspects of network theory is presented in section 2.1. A method to calculate resistances in electrical networks is also given in this section. A Green's function approach is discussed which provides an analytical calculation method of the equivalent resistance between nodes in ordered infinite networks in section 2.2. In most cases, the Green's function approach results in integrals that are not in a closed form, in particular that of the two-dimensional square lattice that must be solved numerically. An analytic approximation to the two dimensional square lattice Green's function is presented in section 2.2. An Effective Medium theory particular to resistive lattices is presented in section 2.3. It provides a mapping between a lattice with a known resistor distribution and a homogeneous effective medium lattice. A discussion of percolation theory for conductive wire networks is given in section 2.4, in particular an expression for the critical wire density is presented. A relationship between wire and junction density is presented in section 2.5. Finally a chapter summary is given in section 2.6

2.1 RESISTIVE NETWORK THEORY

A graph is defined as a collection of N nodes, also called vertices, connected by E edges, also called links⁴⁴. As discussed in chapter 1, graph theory has applications to a wide range of natural and human-made networks, and in this section the definitions fundamental to electrical networks are presented. The terms graph and network will be used interchangeably in this thesis, the latter will refer to graphs applied to a particular system⁴⁴, electrical networks in our case. Figure 2.1 shows a sketch of a simple graph with $N = 5$ nodes and $E = 6$ edges.

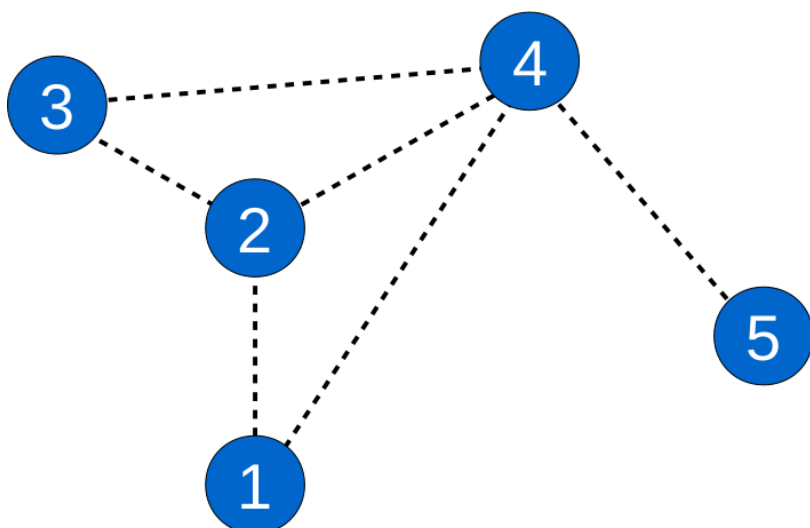


Figure 2.1: A sketch of a simple graph. Nodes are represented by blue circles and are numbered from 1 to 5. The six dotted lines connecting nodes represent the graph edges consisting of links connecting node pairs (1,2), (2,3), (3,4), (2,4), (1,4), and (4,5).

The connectivity of a graph can be described by the so-called Adjacency matrix \mathcal{A} . $\mathcal{A}_{ij} = \mathcal{A}_{ji} = 1$ if nodes i and j are connected and is zero otherwise, essentially

storing the nearest neighbours of each node. The Adjacency matrix for the graph shown in Figure 2.1 is

$$\mathcal{A} = \begin{pmatrix} 0 & 1 & 0 & 1 & 0 \\ 1 & 0 & 1 & 1 & 0 \\ 0 & 1 & 0 & 1 & 0 \\ 1 & 1 & 1 & 0 & 1 \\ 0 & 0 & 0 & 1 & 0 \end{pmatrix} \quad (2.1.1)$$

The degree of each node d_i is defined as the number of edges, or nodes, to which it is connected and can be constructed from the Adjacency matrix as

$$d_i = \sum_{j=1}^N \mathcal{A}_{ij} \quad (2.1.2)$$

The degrees of a graph are represented in diagonal matrix format \mathcal{D} as $\mathcal{D}_{ii} = d_i$ and zero elsewhere. Combining this with the adjacency matrix the Laplacian matrix \mathcal{L} of a graph is defined as

$$\mathcal{L} = \mathcal{D} - \mathcal{A} \quad (2.1.3)$$

and the Laplacian matrix for the graph displayed in Figure 2.1 is given by

$$\mathcal{L} = \begin{pmatrix} 2 & -1 & 0 & -1 & 0 \\ -1 & 3 & -1 & -1 & 0 \\ 0 & -1 & 2 & -1 & 0 \\ -1 & -1 & -1 & 4 & -1 \\ 0 & 0 & 0 & -1 & 1 \end{pmatrix} \quad (2.1.4)$$

A weighed edge is one that has a scalar value associated to it and a weighed graph is one that contains such edges. Consider a graph where the edges between

nodes are weighed with unique values. Let g_{ij} be the weight of the edge connecting nodes i and j , which is zero if they are not connected. Figure 2.2 shows an example weighted graph. The weighed adjacency matrix $\tilde{\mathcal{A}}$ for this graph is

$$\tilde{\mathcal{A}} = \begin{pmatrix} 0 & g_{12} & 0 & g_{14} & 0 \\ g_{12} & 0 & g_{23} & g_{24} & 0 \\ 0 & g_{23} & 0 & g_{34} & 0 \\ g_{14} & g_{24} & g_{34} & 0 & g_{45} \\ 0 & 0 & 0 & g_{45} & 0 \end{pmatrix} \quad (2.1.5)$$

The weighed Adjacency matrix contains the connectivity information of the graph and the weight of each connection. The weighed degree of node i is $\tilde{d}_i = \sum_{j=1}^N \tilde{\mathcal{A}}_{ij}$. Again a diagonal matrix $\tilde{\mathcal{D}}$ can be constructed such that $\tilde{\mathcal{D}}_{ii} = \tilde{d}_i$. The weighed Laplacian matrix is then defined as $K = \tilde{\mathcal{D}} - \tilde{\mathcal{A}}$ and is shown for the example graph of Figure 2.2. For conciseness the diagonal elements shall be left as \tilde{d}_i .

$$K = \begin{pmatrix} \tilde{d}_1 & -g_{12} & 0 & -g_{14} & 0 \\ -g_{12} & \tilde{d}_2 & -g_{23} & -g_{24} & 0 \\ 0 & -g_{23} & \tilde{d}_3 & -g_{34} & 0 \\ -g_{14} & -g_{24} & -g_{34} & \tilde{d}_4 & -g_{45} \\ 0 & 0 & 0 & -g_{45} & \tilde{d}_5 \end{pmatrix} \quad (2.1.6)$$

The weighed graph Laplacian is commonly referred to as the Kirchhoff matrix. It is referred to as such because Kirchhoff's circuit laws for a resistive network are in this form when written as a system of linear equations. By identifying the edge weights g_{ij} as the conductance between voltage nodes i and j , the Kirchhoff matrix can be used to solve current transport in an electrical network in a method known as nodal analysis. Consider two nearest neighbour nodes, l and m , separated by a

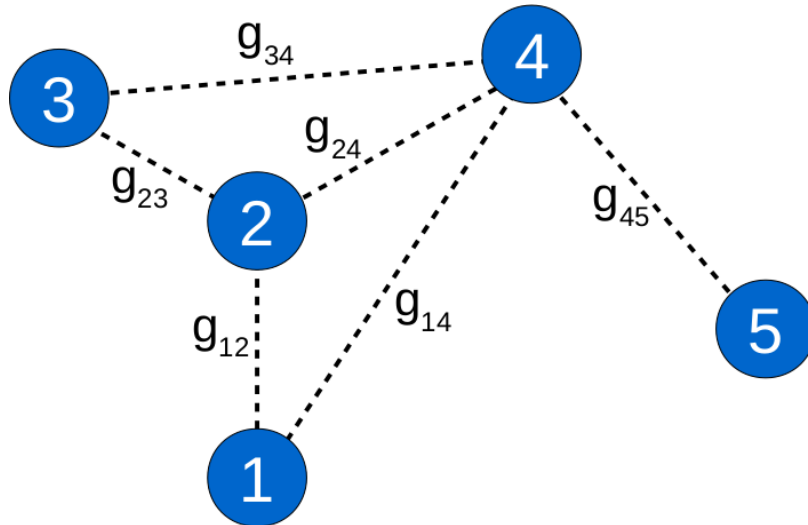


Figure 2.2: A sketch of a simple weighed graph. Nodes are represented by blue circles and are numbered 1 to 5. The dotted lines connecting nodes represent the graph edges. The weight of the edge connecting nodes i and j are represented by g_{ij}

single conductor with weight g_{ml} . Associate a voltage V_m with the node m and V_l with node l . Using Ohm's law, the current flowing from node m to l is

$$\mathcal{I}_{ml} = g_{ml}(V_m - V_l) \quad (2.1.7)$$

For a node where no external current is injected or extracted from the network, the sum of current flowing in and out of a node must be zero according to Kirchhoff's current law. Thus for a node m one has

$$\sum_{j \in n.n}^N \mathcal{I}_{mj} = \sum_{j \in n.n}^N g_{jm}(V_m - V_j) = 0 \quad (2.1.8)$$

where the index j is summed over the indices of node m 's nearest neighbours ($n.n$), of which there are N in total. At nodes where current is sourced or extracted the network must be connected to an external source or drain. This is captured in the

mathematical network by having a non-zero net current at these nodes. If node m is connected to a current source I_m then equation 2.1.8 generalises to

$$\sum_{j \in n.n}^N g_{jm}(V_m - V_j) = I_m \quad (2.1.9)$$

Applying equation 2.1.9 to a network one obtains a series of equations, one per node, that can be expressed in the Kirchhoff matrix notation. In this notation scheme, equation 2.1.9 is written as

$$\sum_{j \in n.n}^N g_{jm}(V_m - V_j) = K_{mm}V_m + \sum_{j \in n.n}^N K_{jm}(V_j) = I_m \quad (2.1.10)$$

Where K is the Kirchhoff matrix, or the weighed Laplacian matrix. Equation 2.1.10 can be written in matrix form as

$$K\vec{V} = \vec{I} \quad (2.1.11)$$

here \vec{V} is the voltage vector containing the voltages at each node and \vec{I} is the current vector, elements of which are nonzero only at the nodal sources and sinks.

The equivalent resistance (R_{eq}) between two nodes m and n is calculated by injecting a current i_0 into node m and extracting i_0 at node n . The vector \vec{I} is written as $\vec{I}_j = i_0(\delta_{jm} - \delta_{jn})$ where δ_{ij} is the Kronecker Delta. Equation 2.1.11 is solved for \vec{V} . The equivalent resistance between the nodes is then

$$(R_{eq})_{mn} = \frac{1}{i_0} |\vec{V}_m - \vec{V}_n| \quad (2.1.12)$$

Consider the conductive network shown in Figure 2.2, equation 2.1.6 is the Kirchhoff matrix associated with this network. We wish to calculate the resistance between nodes 1 and 5 for example. Then the current matrix \vec{I} is given by $\vec{I} = (i_0, 0, 0, 0, -i_0)$ where i_0 is the value of current that is injected or drained. The volt-

ages are calculated in equation 2.1.11 and the resistance is calculated using equation 2.1.12.

2.2 LATTICE GREEN'S FUNCTION FOR INFINITE RESISTIVE NETWORKS

The Kirchhoff matrix technique introduced in the previous section requires a numerical routine to calculate the equivalent resistances between nodes in a network. This involves linear algebra operations on a sparse matrix that is computationally expensive. In some systems an analytical expression can be used to calculate equivalent resistances between nodes in the network, thus making the computational routines unnecessary. Cserti developed such a technique to calculate the resistances of an ordered infinite lattice using its underlying translational symmetries⁴⁵, and is discussed in this section.

The equivalent resistance and the separation between nodes in large but finite sized square lattices were calculated to understand the relationship between the two. This was performed using two simulated square networks of size 500×500 and 300×300 nodes, where each resistive edge x has a resistance $R_x = 1\Omega$. The equivalent resistance between two nodes can be calculated using Ohm's and Kirchhoff's laws outlined in section 2.1. The probing nodes were confined to central regions of the network in order to minimise finite-size effects caused by the change in connectivity at the boundaries of the networks. The results of which are presented in Figure 2.3. There is a log-like trend as the separation between probing nodes increases which is highlighted by the black dashed line meant as a guide to the eye and is proportional to $\ln(x)$. At a large nodal separation finite-size effects begin to cause the equivalent resistances to deviate from the log trend. It is clear the deviation is a finite-size effect as the smaller lattice with 300×300 nodes deviates at a lower separation than the 500×500 lattice.

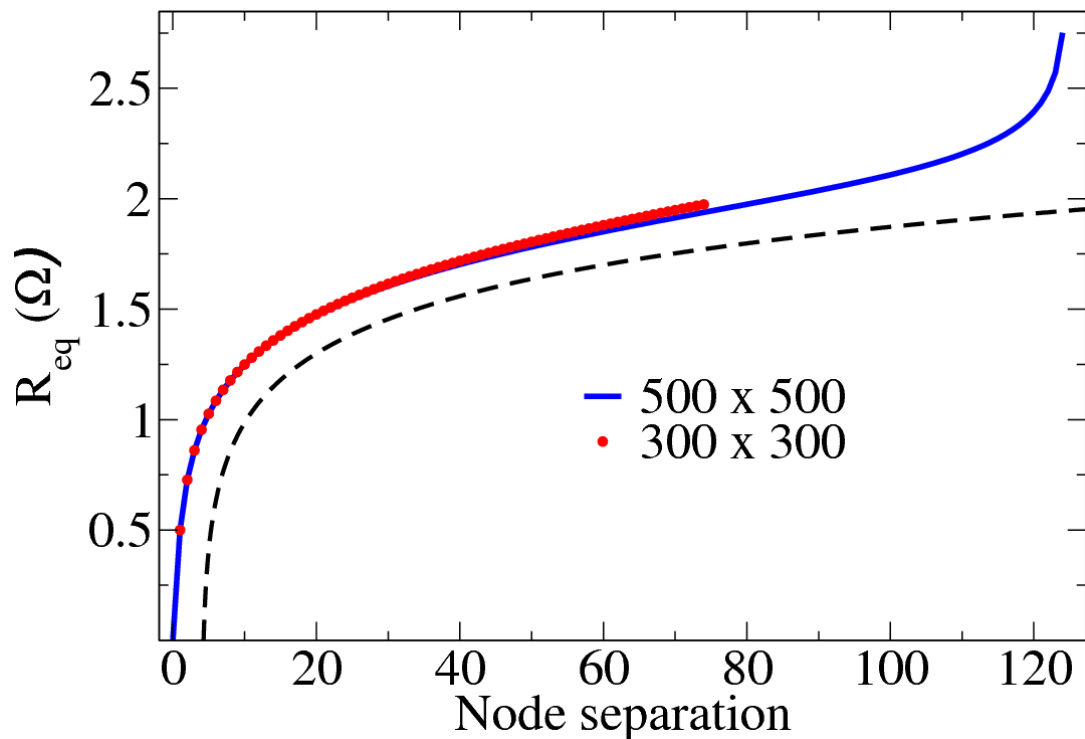


Figure 2.3: Equivalent resistance (R_{eq}) between two nodes on a square lattice with a node separation defined on the x axis. Two finite sized square lattices are simulated, 500×500 nodes (blue) and 300×300 nodes (red). Finite-size effects are observed at the extremes of node separations where the resistance deviates from the log-like trend that exists for smaller separations. It is clear the deviation is a finite-size effect as the smaller lattice with 300×300 nodes deviates at lower separations. The black dashed line is an offset curve proportional to $\ln(x) + \kappa$ where κ is a constant and is meant as a guide to the eye.

In the limit of infinite nodes in the square lattice one would expect the log-like trend to continue indefinitely. To derive a mathematical approximation for the relationship between the equivalent resistance and inter-nodal separation, Cserti made use of Kirchhoff's and Ohms laws along with the translational symmetry of a regular lattice⁴⁵. Consider an infinite and regular resistive lattice. Points on the lattice are defined by spatial vectors of the form

$$\vec{r} = l_1 \vec{a}_1 + \dots + l_d \vec{a}_d \quad (2.2.1)$$

\vec{a}_i are the primitive lattice vectors and $l_i \in \mathbb{Z}$. When $|\vec{a}_1| = |\vec{a}_2| = \dots = |\vec{a}_d| = a$, a d -dimensional hyper-cube with lattice constant a is realised. The primitive vectors \vec{a}_i have reciprocal lattice vectors \vec{k}_i defined such that $\vec{a}_i \cdot \vec{k}_j = 2\pi\delta_{ij}$ where δ_{ij} is the Kronecker Delta.

Resistors, the edges connecting nodes in the lattice, have the same value R_x , and let the potential at the site \vec{r} be $V(\vec{r})$. Current can be injected and extracted at certain nodes. The injected/extracted current is given by the function $I(\vec{r})$; $I(\vec{r}) \neq 0$ if current is extracted or injected at nodal site \vec{r} similar to the current vector in the Kirchhoff's matrix formalism. As in the previous section, in order to measure the resistance between two nodes, inject a current i_0 at one site and extract i_0 at another. At site \vec{r} , by combining Ohm's and Kirchhoff's laws one can write

$$I(\vec{r})R_x = \sum_{\vec{n} \in n.n} (V(\vec{r}) - V(\vec{r} + \vec{n})) \quad (2.2.2)$$

\vec{n} are the vectors connecting the site at \vec{r} to its nearest neighbours (n.n). The right hand side can be described using the Discrete Laplace Operator $\Delta_{\vec{r}}$ defined as

$$-\Delta_{\vec{r}}f(\vec{r}) = \sum_{\vec{n} \in n.n} (f(\vec{r}) - f(\vec{r} + \vec{n})) \quad (2.2.3)$$

Equation (2.2.2) thus becomes

$$\Delta_{\vec{r}}V(\vec{r}) = -I(\vec{r})R_x \quad (2.2.4)$$

The equivalent resistance between the origin ($\vec{0}$) and point \vec{r}_0 is calculated by injecting current i_0 at $\vec{0}$ and extract i_0 at site \vec{r} . $I(\vec{r})$ can be written as

$$I(\vec{r}) = i_0(\delta(\vec{r} - \vec{0}) - \delta(\vec{r} - \vec{r}_0)) \quad (2.2.5)$$

Bringing this together, the equivalent resistance between the two nodes in terms of Green's functions is:

$$R_{GF}(\vec{0}, \vec{r}_0) = \frac{V(\vec{0}) - V(\vec{r}_0)}{i_0} \quad (2.2.6)$$

Equation (2.2.4) is a Poisson-type equation and so can be solved using the lattice Green's function.

$$V(\vec{r}) = R_x \sum_{\vec{r}'} [G(\vec{r} - \vec{r}') I(\vec{r}')] = R_x (G(\vec{r} - \vec{0}) - G(\vec{r} - \vec{r}_0)) \quad (2.2.7)$$

where the Green's function $G(\vec{r} - \vec{r}')$ is defined as follows

$$\Delta_{(\vec{r}')} G(\vec{r} - \vec{r}') = -\delta(\vec{r} - \vec{r}') \quad (2.2.8)$$

Combining equation (2.2.6) and (2.2.7) and the fact that the lattice greens function is even, one can calculate the resistance between the two points as

$$R_{GF}(\vec{r}_0) = 2R_x[G(\vec{0}) - G(\vec{r}_0)] \quad (2.2.9)$$

Consider a hyper-cube with periodic boundary conditions with L lattice points along each dimension. The total number of nodes in the d -dimensional hyper-cube is L^d . The Fourier transform of the system is thus

$$G(\vec{r}) = \frac{1}{L^d} \sum_{\vec{k} \in BZ} G(\vec{k}) e^{i\vec{k} \cdot \vec{r}} \quad (2.2.10)$$

Due to the periodic boundary conditions, the reciprocal vector \vec{k} is confined to the first Brillouin zone (BZ), or the primitive cell of the reciprocal lattice.

$$\vec{k} = \frac{m_1}{L} \vec{k}_1 + \frac{m_2}{L} \vec{k}_2 + \dots + \frac{m_d}{L} \vec{k}_d \quad (2.2.11)$$

Combining this with equation 2.2.8 we find

$$G(\vec{k}) = \frac{1}{\epsilon(\vec{k})} = \frac{1}{2 \sum_{i=1}^d (1 - \cos(\vec{k} \cdot \vec{a}_i))} \quad (2.2.12)$$

where $\epsilon(\vec{k})$ is the dispersion relation of the resistive lattice Green's function propagator. The Green's function now takes the form

$$G(\vec{r}) = \frac{1}{L^d} \sum_{k \in BZ} \frac{e^{i\vec{k} \cdot \vec{r}}}{\epsilon(\vec{k})} \quad (2.2.13)$$

In the limit where the hyper-cube becomes infinite in all directions, the number of points in the hyper-cube L^d tends to infinity. The summation over the Brillouin zone becomes an integral in this limit

$$\frac{1}{L^d} \sum_{k \in BZ} \rightarrow v_0 \int_{k \in BZ} \frac{d^d \vec{k}}{(2\pi)^d} \quad (2.2.14)$$

where $v_0 = a^d$ is the volume of the unit cell of the hyper-cube. In the limit of the infinite hyper-cube the Greens function takes the form

$$G(\vec{r}) = v_0 \int_{k \in BZ} \frac{d^d \vec{k}}{(2\pi)^d} \frac{e^{i\vec{k} \cdot \vec{r}}}{\epsilon(\vec{k})} \quad (2.2.15)$$

Let one of the points be the origin and the other point be described by the vector \vec{r}_0 . Let the resistance of each edge in the network be R_x . Returning to equation 2.2.9 the Green's function for the equivalent resistance in a lattice is

$$R(\vec{0}, \vec{r}_0) = 2R_x v_0 \int_{k \in BZ} \frac{d^d \vec{k}}{(2\pi)^d} \frac{1 - e^{i\vec{k} \cdot \vec{r}_0}}{\epsilon(\vec{k})} \quad (2.2.16)$$

Equation 2.2.16 is a general form for a d-dimensional hyper-cube. However this lattice Green's function method can be applied to other lattice structures.

For some lattices the resulting Green's function can be solved exactly and in others can be approximated quite well. A one dimensional hyper-cube is merely

an infinite linear chain of resistors and is the simplest form of lattice to consider. Let one of the electrodes be placed at the origin and another at a site b nodes away. The equivalent resistance between the two points where each resistor has a value of R_x is

$$R_{1D}(b) = R_x \int_{-\pi}^{\pi} \frac{dk}{2\pi} \frac{1 - e^{ibk}}{1 - \cos(k)} \quad (2.2.17)$$

Using the Residue method the resistance reduces to $R_{1D}(b) = b \times R_x$, which is what one would expect.

In the case of a 2 dimensional square lattice with a lattice spacing set to 1, equation 2.2.16 reduces to

$$R_{\square}(\vec{r}_0) = R \int_{\vec{k} \in BZ} \frac{d\vec{k}}{(2\pi)^2} \frac{1 - e^{i\vec{k} \cdot \vec{r}_0}}{2 - \cos(b_1) - \cos(b_2)} \quad (2.2.18)$$

where $\vec{k} = b_1 \vec{k}_1 + b_2 \vec{k}_2$. Let $\vec{r} = l_1 \vec{a}_1 + l_2 \vec{a}_2$. The final integral, while being an elegant formalism, does not have a simple analytical solution. One of the integrals in equation 2.2.18 can be removed with the method of residues. The residue theorem states that $\oint_{\gamma} f(z) dz = 2\pi i \sum_{\zeta_k} \text{Res}(f, \zeta_k)$ where γ is a closed path and the function $f(\zeta_k)$ is undefined at all complex poles ζ_k . The residue of a function at a simple pole ζ can be calculated as

$$\text{Res}(f, \zeta) = \lim_{z \rightarrow \zeta} (z - \zeta) f(z) \quad (2.2.19)$$

If the function $f(z)$ can be written as a quotient of two other functions, $f(z) = \frac{g(z)}{h(z)}$, the Residue at a simple pole can be written as $\text{Res}(f, \zeta) = \frac{g(\zeta)}{h'(\zeta)}$

Consider the resistance given by $R_{\square}(m\vec{a}_1 + n\vec{a}_2)$, here we derive the approximation to equation 2.2.18 first given by Cserti⁴⁵. The integral is of the form $R \int_{-\pi}^{\pi} \frac{dy}{2\pi} I(y)$ with $I(y)$ given by

$$I(y) = \int_{-\pi}^{\pi} \frac{dx}{2\pi} \frac{1 - e^{inx} e^{imy}}{2 - \cos(x) - \cos(y)} \quad (2.2.20)$$

Introduce a complex variable $z = e^{ix}$ and performing the integral with the method of residues

$$I(y) = -2i \oint \frac{dz}{2\pi} \frac{1 - z^n e^{imy}}{2z(2 - \cos(y)) - z^2 - 1} \quad (2.2.21)$$

The path of integration is the unit circle. The roots of the denominator are given by $z = e^{\pm i\theta}$ with $\theta = \cos^{-1}(2 - \cos(y))$. Since $2 - \cos(y) > 1$ for y in the range $[-\pi, \pi]$, θ is imaginary. Introduce s such that $\theta = is$, therefore s satisfies the equation $\cosh(s) = 2 - \cos(y)$. Since $\cos(i\alpha) = \cosh(\alpha)$ the roots can be rewritten as $z_{\pm} = e^{\pm s}$. Note that $e^{-s} < 1$ and $e^s > 1$ so there is only one pole of the integral $I(y)$ inside the unit circle. Thus the integral can be solved as

$$I(y) = 4\pi \frac{1}{2\pi} \frac{1 - e^{-ns} e^{imy}}{2 - \cos(y) - 2e^{-s}} = \frac{1 - e^{-ns} e^{imy}}{\sinh(s)} \quad (2.2.22)$$

The remaining integral is thus

$$R_{\square}(m, n) = R \int_{-\pi}^{\pi} \frac{dy}{2\pi} \frac{1 - e^{-ns} e^{imy}}{\sinh(s)} = R \int_0^{\pi} \frac{dy}{2\pi} \frac{1 - e^{-ns} \cos(my)}{\sinh(s)} \quad (2.2.23)$$

The integral cannot be solved exactly but an approximation can be made for large values of m and n . Breaking the integral into three parts we get

$$\begin{aligned} R_{\square}(n, m) &= R \int_0^{\pi} \frac{dy}{2\pi} \left(\frac{1 - e^{-ns} \cos(my)}{y} \right) + \left(\frac{1}{\sinh(s)} - \frac{1}{y} \right) + \\ &\quad + \left(\frac{e^{-ns} \cos(my)}{y} - \frac{e^{-ns} \cos(my)}{\sinh(s)} \right) \end{aligned} \quad (2.2.24)$$

The second integral can be solved exactly

$$\int_0^{\pi} \frac{dy}{2\pi} \left(\frac{1}{\sqrt{(2 - \cos(y))^2 - 1}} - \frac{1}{y} \right) = \frac{1}{2\pi} \left(\frac{\ln(8)}{2} - \ln(\pi) \right) \quad (2.2.25)$$

The integrand in the last integral is close to zero for small values of y and s as $\sinh(s) \approx s \approx y$ for small values of y . For large values of y the integrand decays

exponentially. Thus the contribution of the third integral is negligible. The first integral is in the form of the Ein function $\text{Ein}(z) = \int_0^z \frac{1-e^{-x}}{x} dx$. For large values of z , one obtains $\text{Ein}(z) \approx \log(z) + \gamma$ where $\gamma = 0.57721\dots$ is the Euler-Mascheroni constant. Therefore

$$\frac{1}{2\pi} \text{Re} \left(\int_0^\pi dy \frac{1 - e^{ny - imy}}{y} \right) = \frac{1}{2\pi} \text{Re} (\text{Ein}(\pi(n - im))) \approx \frac{1}{2\pi} (\ln(\sqrt{n^2 + m^2} + \gamma + \ln(\pi))) \quad (2.2.26)$$

The full approximation for the resistance on an infinite square lattice is thus

$$R_{\square}(m, n) \approx \frac{R}{\pi} \left(\ln \sqrt{m^2 + n^2} + \gamma + \frac{\ln 8}{2} \right) \quad (2.2.27)$$

Figure 2.4 (a) plots the resistance between two nodes in an infinite square resistive network as the separation between nodes is increased according to the Kirchhoff method (brown line) and the approximation to the lattice integral (red dashed curve). Note that the resistance of each resistor in the network is set to 1Ω . There is excellent agreement between the approximation and the numerical solutions to the integral given in equations 2.2.27 and 2.2.18 respectively. The relative error was calculated as the relative error of the approximation with the integral solution and is plot in Figure 2.4 (b). As the separation between the nodes is increased the relative error decreases towards zero. This is due to the approximation of the integral being best for large electrode separation, as mentioned before.

A large square resistive network was simulated in order to determine the accuracy of the lattice Greens function. Each resistor in the network has the same resistance of 1Ω and the simulated network was made very large (500×500 nodes) and the equivalent resistance was measured between pairs of nodes near the centre of the network in order to mitigate finite-size effects. The resistance between nodes is calculated using the Kirchhoff matrix method. Figure 2.5 shows the equivalent resistance between two nodes in the simulated network and is compared with the approximation to the lattice Greens function in equation 2.2.27. The approximation

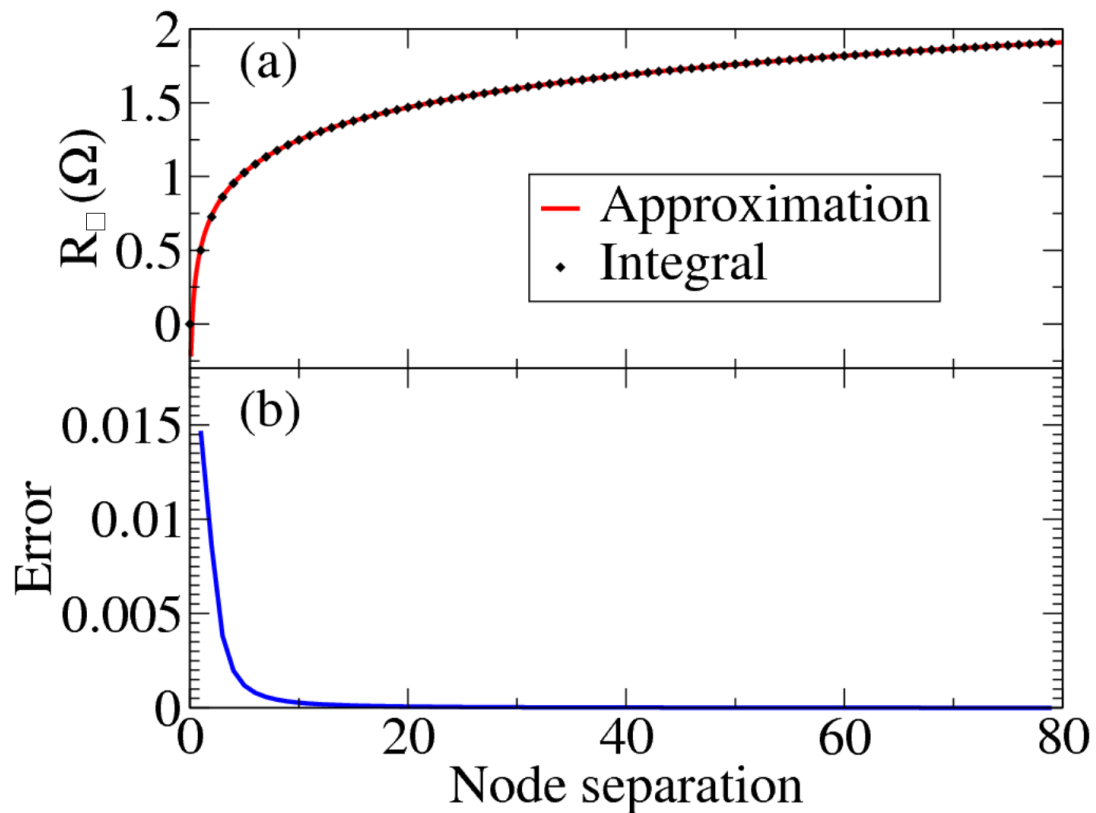


Figure 2.4: (a) The numerical solutions to the resistance lattice Green's function R_{\square} given in equation 2.2.18 is shown as black diamonds. All resistors in the network are identical at 1Ω . The approximation of the integral given by equation 2.2.27 is plot as red dashed line. (b) The relative error of the approximation with respect to the numerical solution of the lattice Green's function. The error converges to zero at increasing nodal separation.

does indeed match the values given by the simulated network and accounts for the log-trend that was identified in Figure 2.3.

While this analysis was focused on square resistive lattices, it can be applied to d-dimensional hyper-cube lattices and other periodic lattices. In particular Cserti also derived lattice resistance integrals for triangular and hexagonal lattices⁴⁵.

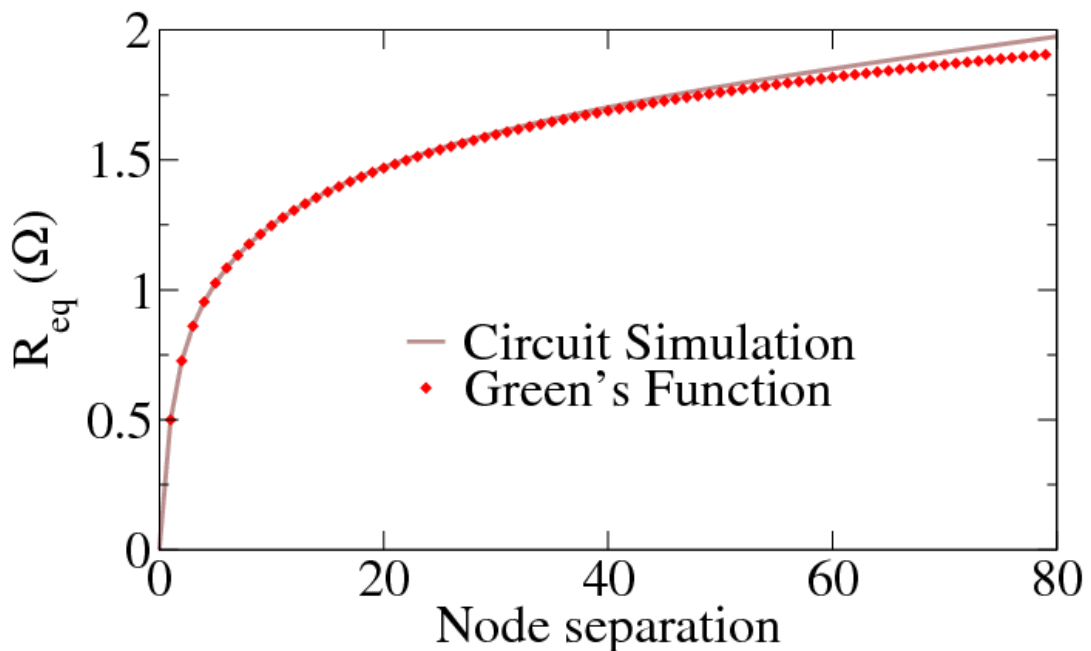


Figure 2.5: The brown represents the equivalent resistance between two nodes in a simulated square lattice resistive network. The simulated network contained 500×500 nodes in total and the resistance between nodes at the centre of the network was measured in order to minimise finite-size effects. The red diamonds represents the approximation of the lattice Greens function given in equation 2.2.27.

2.3 EFFECTIVE MEDIUM THEORY

Here an overview of resistive lattice effective medium theory and the associated mathematical framework is presented. A novel effective medium for nanowire networks is derived in chapter 4 that utilises the theory outlined in this section.

Effective medium theories (EMTs) for resistive lattices have been used extensively to model their properties for many decades. Kirkpatrick first generalised effective medium theory, previously used to approximate the conductance of mixed materials such as alloys, for resistive lattices in the 1970's⁸¹. Consider a finite ordered square lattice whose resistive edges follow a given distribution with an external voltage applied along one of the primitive axis of the network. The potentials at each node in the network is then due to the external field (V_{ext}), which increases

incrementally per row of nodes, and a fluctuating local field (\bar{V}) caused by local deviations in resistors from the distributions mean. The average internal field is identical to that of the external and the local field fluctuations average out to zero. The average internal field of the network is captured by the effective medium network and is defined such that the internal field of the network is the same as the external field. To realise the effective medium network each conductor is replaced with an effective conductance g_m .

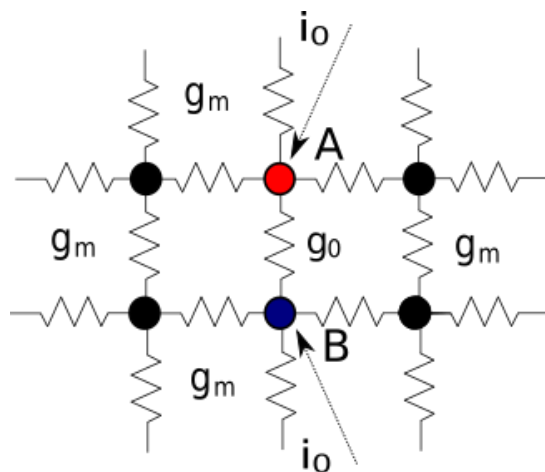


Figure 2.6: A sketch of a regular lattice of resistors each with a conductance of g_m . The conductor between nodes A and B has its conductance changed to g_0 causing a fluctuation in the voltage across it. A fictitious current is injected at A and extracted at B which is tuned to counteract this fluctuation of the voltage.

In order to calculate the effective conductance consider a network where the conductor between nodes A and B has a conductance $g_{AB} = g_0$ and is surrounded by the effective medium, a visualisation of which can be seen in Figure 2.6. Due to current conservation the sum of currents in and out of a node in the network is zero unless an external source of current is injected or extracted there as discussed previously. For node A specifically;

$$\sum_l g_{Al}(V_A - V_l) = I_A \quad (2.3.1)$$

$V_A - V_B$ being the potential difference between the two nodes. The voltage between nodes A and B is due to the external field V_{ext} and the fluctuation voltage \bar{V} . Introduce a fictitious current i_0 which is injected at node A and extracted at node B which counteracts the fluctuating voltage. We can thus write

$$V_{\text{ext}}(g_m - g_0) = i_0 \quad (2.3.2)$$

Let Γ'_{AB} be the equivalent conductance between nodes A and B where the conductor $g_{AB} = 0$ in Figure 2.6. The fluctuating voltage can be written as

$$\bar{V} = \frac{i_0}{g_0 + \Gamma'_{AB}} \quad (2.3.3)$$

The equivalent conductance between nodes A and B in the effective network is $\Gamma_{AB} = g_m + \Gamma'_{AB}$. Γ_{AB} can be calculated using a superposition of current extraction/injection. Inject a current i_0 at node A and extract it at a large distance away in all directions such that the current $\frac{i_0}{z}$ flows through each of node A's z edges. At the same time inject a current i_0 at infinity in all directions and extract at node B, causing a current $\frac{i_0}{z}$ flowing through B's z edges. Performing both operations simultaneously, the current flowing between nodes A and B is then $\frac{2i_0}{z}$ and currents at infinity cancel to zero. It follows that the conductance $\Gamma_{AB} = \frac{z}{2}g_m$. Thus $\Gamma'_{AB} = (1 - \frac{z}{2})g_m$. Combining equations 2.3.2 and 2.3.3 we have

$$\bar{V} = \frac{V_{\text{ext}}(g_m - g_0)}{g_0 + (\frac{z}{2} - 1)g_m} \quad (2.3.4)$$

We want the average of fluctuations of the potential to go to zero. Since the conductances g_0 follow a distribution $f(g)$ we write

$$\int dg f(g) \frac{(g_m - g)}{g + (\frac{z}{2} - 1)g_m} = 0 \quad (2.3.5)$$

For example, consider a square resistive lattice ($z = 4$) and a binary resistor distribution where the respective proportions are $P_1 = P$ and $P_2 = 1 - P$ and conductances g_1, g_2 . The conductance distribution is thus

$$f(g) = P_1\delta(g - g_1) + P_2\delta(g - g_2) = P_1\delta(g - g_1) + (1 - P_1)\delta(g - g_2) \quad (2.3.6)$$

where $\delta()$ is the Dirac delta function. Solving equation 4.2.4 the effective conductance g_m is given as

$$(g_m)_\pm = \frac{g_2 - g_1}{2} + 2p(g_1 - g_2) \pm \left(4g_1g_2 + (g_1 - g_2)^2(1 - 2p)^2\right)^{\frac{1}{2}} \quad (2.3.7)$$

Figure 2.7 plots the two roots as a function of P with $g_1 = 1$ S and $g_2 = 0.1$ S. Clearly one of the roots is not an appropriate choice as it is negative for every value of P . This root corresponds to $(g_m)_-$ and so the solution is $(g_m)_+$. For $P = 0$ there are no g_1 conductors and so the effective conductance matches that of $g_1 = 0.1$, the opposite is the case when $P = 1$.

Note that the effective medium theories work best where the fluctuations in the current flow through the network are relatively small. Where the current is funneled through a few critical paths the EMT will not work well. Similarly as the EMT is an averaging theory, the larger the network the more accurate the EMT.

2.4 PERCOLATION THEORY AND CRITICAL WIRE DENSITY

Earlier in this chapter the Kirchhoff matrix and Greens's function methods were introduced to calculate the resistance of a network, however these methods required the knowledge of the exact layout of the networks. Large-scale nanorod devices contain countless components making it difficult to accurately capture the layout of the network. Percolation theory⁴⁷ has been used for many decades to understand

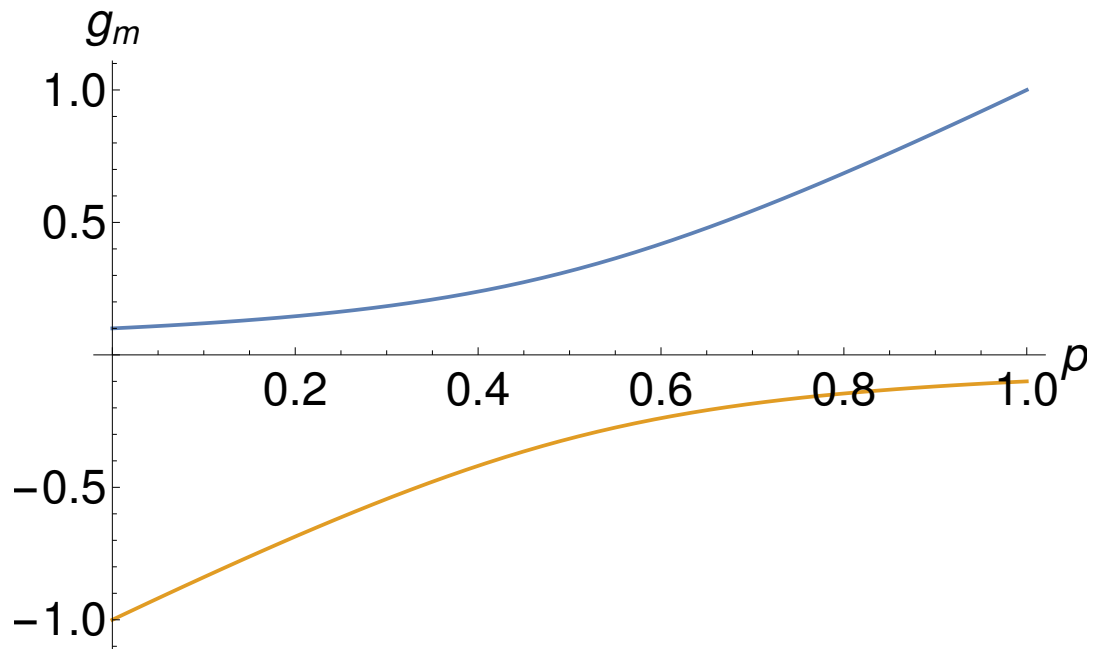


Figure 2.7: The two solutions $(g_m)_\pm$ to the effective medium theory in a binary resistor distribution where the relative proportions of the two conductors is given by P . In this figure the conductors have values 1 S and 0.1 S respectively.

properties of such devices as it is essentially the behaviour of connected nodes in mathematical graphs^{12,46,48,82}. Here we shall focus on using percolation theory to describe the conductive properties of a nanowire network.

Consider the two dimensional square lattice presented in Figure 2.8 consisting of 16 sites. Each site is occupied with some probability P , $0 \leq P \leq 1$ ($P = 10/16$ in the case of Figure 2.8). Percolation theory is concerned with the connectivity of such a system, and how it depends on the contact probability P for different types of networks. A *cluster* of *cluster size* s is defined as a group of s connected occupied sites. Returning to the network shown in Figure 2.8, there are four different clusters. The red sites belong to a cluster of size four, the green sites are a cluster of size three, the blue of size two and yellow a cluster of size one. For a finite sized lattice, there is some critical value of P where a cluster will span (or percolate) between two boundaries. A concrete definition of the critical value is one where a cluster of infinite size first appears in an infinite lattice. This critical value is known as

the percolation threshold P_c and is a phase transition between a conductive and a non-conductive network.

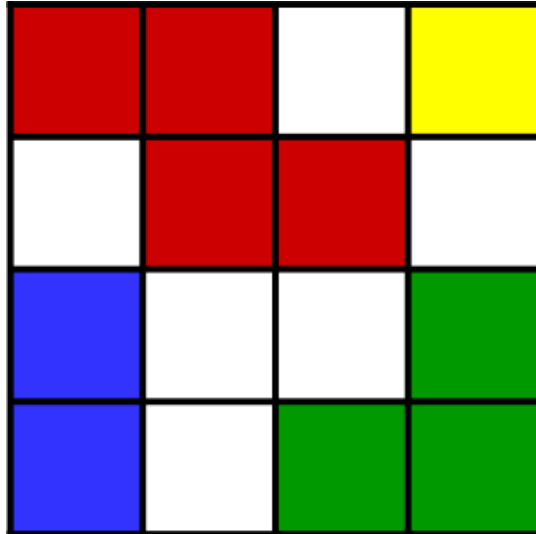


Figure 2.8: A 2-D square lattice of size 4×4 site. Sites are occupied with a certain probability P . Each occupied site is represented by different colours, each colour represents a different cluster. There is a clusters of size 4 (red), 3 (green), 2 (blue), and 1 (yellow). Unoccupied sites appear in white.

Percolation theory can be used to study continuum systems, as well as the lattice percolation problems discussed above. Continuum percolation problems include randomly positioned disks, sticks, squares, spheres e.t.c. In this work we will focus on the percolative properties of widthless conductive sticks as these best mirror the high aspect ratio nanowires we are concerned with. Similar to the critical occupancy probability there exists a critical wire density $(n_w)_c$, below which a percolative path will not form between two opposite boundaries. Stick percolative systems were studied in 1974 by Pike and Seager⁴⁶ and their work has been applied extensively in recent years to nanorod systems^{34,83}. Using Monte Carlo Simulations of randomly positioned and orientated sticks Pike and Seagar determined a relationship between the critical wire length (L_c) and wire densities (n_w)

$$L_c \left(\frac{\sqrt{\pi n_w}}{2} \right) = 2.118 \quad (2.4.1)$$

Li et al obtained a more accurate relationship between these quantities in 2009 through larger computational simulations and explicitly including finite-size effects⁴⁸.

$$(n_w)_c L^2 = 5.63726 \pm 0.00002 \quad (2.4.2)$$

Li et al's definition of the critical wire density is as follows, given an ensemble of random stick networks at the critical wire density percolation occurs in 50% of the networks. The critical wire density is an important parameter for NWNs, describing the minimum wire density that will result in a conductive network and is referenced multiple times throughout this thesis.

2.5 JUNCTION DENSITY AS A FUNCTION OF WIRE

DENSITY AND LENGTH

It is clear that the wire lengths and density play an important role in resistive properties of a nanowire network, collectively they largely determine the connectivity profile. The connectivity profile refers to the inter-nanowire junctions that occur in the network and so it is critical to understand the dependence of junction density on these fundamental properties of the nanowires, their length and wire density.

Heitz et al⁸⁴ calculated the contact probability (ψ) between two widthless sticks where their centres are no more than L apart, L being the length of each stick. Using a geometric and statistical approach, Heitz et al analytically calculated the contact probability as $\psi = 0.2027$ and supported this with Monte Carlo simulations. We used the contact probability to relate the wire density with junction density in a nanowire network⁸⁵. Consider a NWN with a wire density n_w . Focus on a single wire in the network, the expected number of wires whose centres are no more than L away from its own is $n_w \pi L^2$. Thus the expected number of contacts on this wire

is $\psi n_w \pi L^2$. There are a total of $N_w = n_w A$ wires in the network, A being the total area of the network. Thus the total number of junctions in the network is

$$N_j = \frac{1}{2} \psi \pi L^2 n_w^2 A \quad (2.5.1)$$

Where a factor of two is included to negate double counting. In terms of junction and wire densities the relationship is

$$n_j = \frac{1}{2} \psi \pi L^2 n_w^2 = \omega L^2 n_w^2 \quad (2.5.2)$$

where $\omega = \psi \pi / 2$ shall be used from here in order to simplify the notation.

Figure 2.9(a) presents the junction density as a function of wire density, the curves to equation 2.5.2 and data points corresponding to Monte Carlo simulations of the average n_j for an ensemble of nanowire networks at a specified n_w . The blue dashed curve uses the value $\omega = \frac{1}{2} \psi \pi \approx 0.316$ whereas the red solid curve is $\omega = 0.27$. The red curve provides a more accurate description of the simulation results, suggesting that the contact probability in our systems is not 0.2027 as found by Heitz et al, but $\psi = 2 \times 0.27 / \pi \approx 0.17$. Boundary effect account for this disagreement as wires that lie a distance of L from the nearest network edge will experience fewer intersections on average. To confirm this, Figure 2.9(b) presents the junction density vs wire density for two NWNs of size $30\mu\text{m} \times 30\mu\text{m}$ (orange) and $40\mu\text{m} \times 40\mu\text{m}$ (green). The larger network has a consistently higher junction density and is closer to the theoretical result with $\omega = 0.316$ shown as the blue dashed curve. Thus the larger a network the closer its junction density will be to the theoretical value. On the other hand for finite NWNs in this thesis, one expects those with larger wire lengths and wire densities to have junction densities lower than the theoretical value. This is the first reported relation of finite-size effects in nanowire network junction density and may offer insights into boundary effects on the conductivity of such systems. In later chapters the expression for the wire density in equation 2.5.2 is used extensively in the discussion of nanowire net-

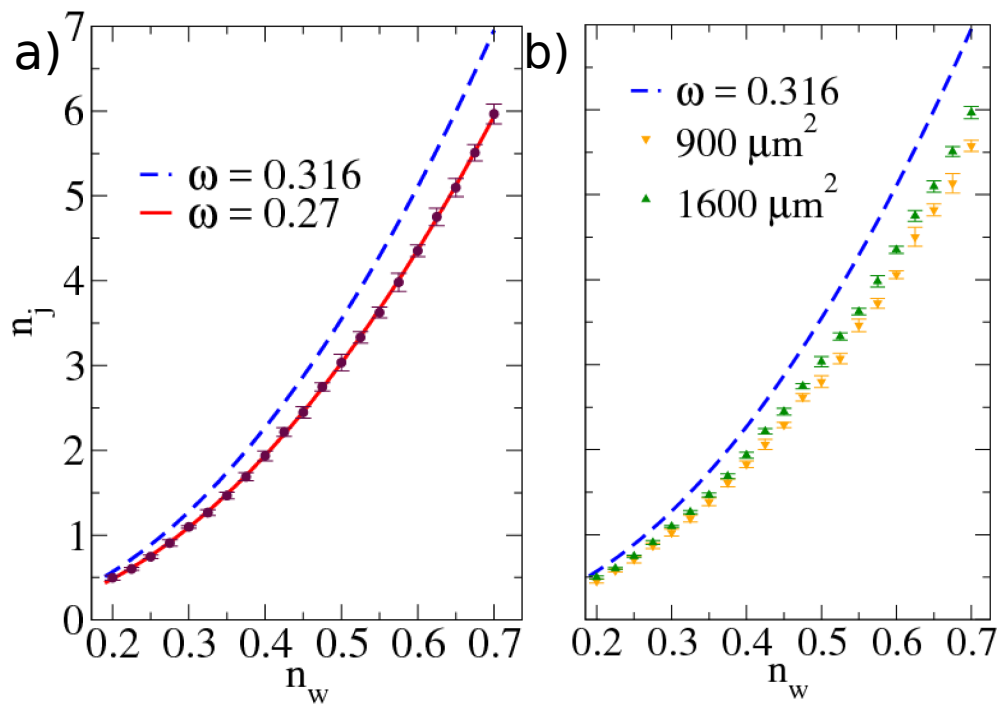


Figure 2.9: (a) Black data points are average junction density vs Wire density obtained from Monte Carlo simulations of NWNs with various wire densities, size $40 \times 40 \mu\text{m}$, and wire lengths of $7 \mu\text{m}^2$. Note that ten simulations were performed per wire density and the resulting 95% confidence interval is also shown. The blue dashed line corresponds to the analytical expression with $\omega \approx 0.316$ calculate using $P_c = 0.2027$ as derived by Heitz et al. The red curve corresponds to equation 2.5.2 with $\omega = 0.27$ and agrees much closer to the Monte Carlo simulations. (b) The boundary effects on the relationship between junction and wire density. The orange data points are average junction densities for networks of size $30 \mu\text{m} \times 30 \mu\text{m}$ and the green for networks of size $40 \mu\text{m} \times 40 \mu\text{m}$. Both networks have wires of length $7 \mu\text{m}$. The blue dashed line is the analytical expression equation 2.5.2 with $\omega = 0.316$.

work conductivity, particularly in chapter 4 where it is central to a novel effective medium theory for nanowire networks.

2.6 CHAPTER SUMMARY

In this chapter the necessary background theory and mathematical formalisms to understand current flow through a nanowire network was introduced, and will be referred to throughout this thesis. In section 2.1 some fundamental aspects of

network theory was introduced. Network theory was applied to an electrical network and shown to follow Kirchhoff's circuit laws. It was shown that the electrical properties of a network can be calculated by solving a system of linear equations containing the connectivity profile and resistances of the network. In section 2.2 an analytical method to calculate resistances in an ordered infinite lattice developed by Cserti⁴⁵ was presented. An approximation to the lattice Green's function solution to resistances on a square lattice was presented and shown to be very accurate, particularly at large distances. An effective medium theory for ordered resistive lattices was presented in section 2.3. An effective medium for a two dimensional square lattice with a bi-modal resistance distribution was derived as an example. A brief introduction to Percolation theory was given in section 2.4. In particular the critical wire density for a conductive stick system in two dimensions was presented, a density which is the lower bound to ensure an electrically conductive network between two opposite electrodes. Finally a functional form for the junction density was presented in section 2.5, relating the junction density with wire density and wire length.

The methods and general theory layed out in this chapter play a pivotal role in examining current flow in the nanowire networks. The Kirchhoff method to calculate network resistivity is used throughout this thesis, being crucial to results presented in every chapter. The Green's function technique offers an insight into how current flows through an ordered medium which can act as a template to current flow in a disordered one. This will be the foundation to a novel extended effective medium we developed for nanowire networks which will be discussed further in chapter 4. The critical wire density determined by percolation theory is of vital importance in understanding limitations of nanowire networks with regards sparsity and is used as a lower bound in simulations throughout the thesis. Similarly our expression for junction density and in turn the connectivity of a network is of fundamental importance for understanding the properties of networks and is used throughout the thesis.

3

COMPUTATIONAL MODELS FOR DISORDERED NANOWIRE NETWORKS AND THEIR APPLICATIONS

The conductance of a nanowire network depends on a multitude of underlying parameters; the length and diameter distributions of nanowires^{12,46,83,86,87}, inter-wire junction resistances⁸⁸, resistance of nanowire segments⁴⁹, wire density⁸², connectivity profile, and device dimensions⁸⁹ to name but a few. All of these parameters and physical features will impact the conductance of a NWN. A common method of numerically solving this complex transport problem⁸¹ is to map the NWN onto a node-voltage graphical representation where each nanowire is a node in the graph and is connected to its nearest neighbours by a resistor corresponding to the inter-wire junction. Kirchhoff's current laws and Ohm's law are applied to the node-voltage graph to calculate the conductance of the system as outlined in chapter 2⁹⁰. An implicit assumption is being made in this approach: the junction resistance is much higher than the nanowire inner resistance and so dominate the electrical properties of the network. This approach shall be referred to as the Junction Dominated Assumption (JDA) henceforth.

Monte Carlo simulations of conductive stick networks show that their electrical properties are highly sensitive to the ratio R_{in}/R_j where R_j is the resistance of a junction and R_{in} is the inner resistance of a wire segment^{48,49,87}. The JDA model has successfully calculated the resistive properties of carbon nanotube networks as the nanotube resistance is negligible compared with the resistance of a nanotube junction^{12,91}. Metallic nanowire junctions however have been shown to have relatively

low junction resistances⁹² and, as a result, the nanowires themselves have a sizable impact on the network conductivity. With the demand for increasing NWN conductivity for optoelectric device applications, R_j is continuously being minimised by effective annealing techniques^{34,80,93,94} and so the JDA is not appropriate for these systems. In this chapter we introduce a model that includes all nanowire resistances, the Multi-Nodal Representation (MNR), and show how both MNR and JDA models depend differently on the underlying parameters mentioned at the start of the chapter.

A fundamental issue with nanowire network simulations is the inherent spatial randomness of wire positions and their impact on network connectivity. Experimental measurements can only be related to the average results of simulations with matching underlying parameters in order to obtain meaningful results⁸⁸. To directly compare computational simulation with experimental measurements we developed a method to digitally capture the positions and orientations of nanowires from Scanning Electron Microscope (SEM) images of NWNs. The goal of this chapter is to compare MNR and JDA simulations using both configurational averaging and digitised networks with experimental samples to understand the effect of nanowire resistance on certain network properties.

The layout of this chapter is as follows. In section 3.1, the JDA and MNR models are presented and the computational simulations are outlined. In section 3.2, MNR and JDA approaches are applied to simulations of NWNs and the dependence of sheet resistance on a selection of nanowire properties are explored, highlighting the impact of inner-wire resistance on these relationships. In section 3.3, an original technique that digitises images of experimental NWNs to which the JDA and MNR are applied. The digitised networks can be used to approximate the junction resistance of the samples and these results were compared with a distribution of junction resistances that were measured experimentally⁹². The ultimate conductivity of a NWN, that which is obtained when junctions are annealed to their optimum capacities, is then calculated for each of the experimental samples. A novel way of

quantifying the potential for network conductance improvement is introduced in section 3.3 and its dependence on several network parameters are presented⁷⁹. In section 3.4 the effect of including dispersion in the junction resistances is examined for MNR and JDA mappings. A short chapter summary is presented in section 3.5.

3.1 GRAPHICAL REPRESENTATIONS OF NANOWIRE NETWORKS

To calculate the resistive properties of a NWN, the nanowire mesh must be mapped into a mathematical graph that captures the connectivity information of the network and node-voltage points so that Kirchhoff's system of linear equations introduced in chapter 2 can be used. In the JDA mapping, each wire is represented by a circuit node at a common voltage connected to other wires by junction resistors (edges of the graph). A NWN with N_w wires will result in a resistive graph with N_w nodes. An off-diagonal element in Kirchhoff matrix (K_{ij}^{jda}) is the conductance of the inter-wire junction between wires i and j . Figure 3.1(a) is a sketch of a simple NWN (top) with its JDA graphical representation (bottom). There are three nodes in this graphical representation, one for each nanowire, and two inter-wire junctions with resistance R_j . Note that there is no junction between wires W_1 and W_2 , thus there is no resistor in this connection in the graph representation. The locations of the nanowires are irrelevant in the JDA; only the connectivity profile of the network and R_j determine its the electrical properties. As this mapping only acts on the inter-wire connectivity, the inner-wire resistances of the nanowire segments are entirely omitted from this model.

While the JDA is suitable for materials with sufficiently large junction resistance the nanowire resistance cannot be omitted for materials where it is comparable with that of the junctions. In order to include the inner wire resistances a new voltage-node mapping is needed. Consider a wire that has b intersections with other wires

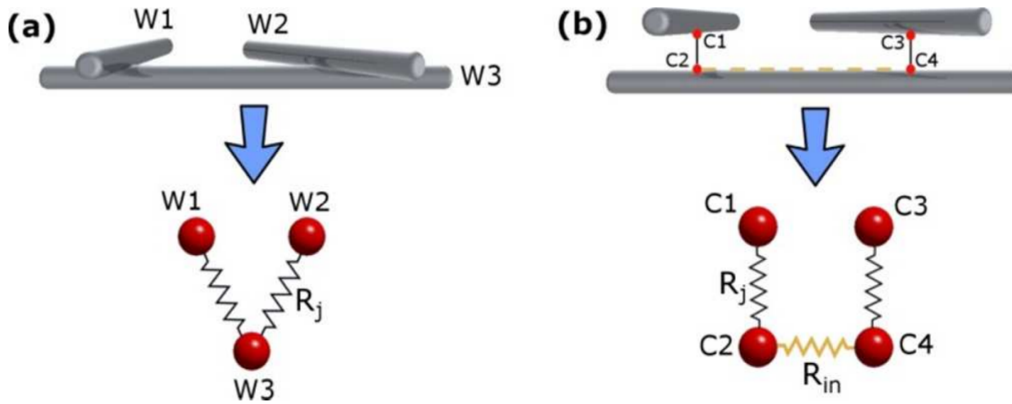


Figure 3.1: (a) A sketch of a simple NWN with three wires labeled W_i , $i = 1, 2, 3$ and two inter-wire junctions, one between wires W_1 and W_2 and another between wires W_1 and W_3 ⁷⁹. Underneath the sketch is a graphical representation of the NWN; there are three nodes corresponding to the three wires and two inter-wire junction resistors represented by black resistors with resistances of R_j . (b) An expanded view of the three wires sketched in panel (a). The four connection nodes, two for each inter-wire junction, are shown as the red dots labeled C_i , $i = 1, 2, 3, 4$. Underneath the sketch is an MNR graphical representation of the NWN. Connection nodes associated with the same junction are connected by a junction resistor R_j and shown in black. The connection nodes that are adjacent on W_3 , C_2 and C_4 , are connected by an nanowire segment resistor R_{in} illustrated by the yellow resistor.

thus partitioning it into $b + 1$ wire sections each with a classical resistance given by

$$R_{in} = \frac{\rho \ell_i}{A_c} \quad (3.1.1)$$

where ρ is the wire resistivity, ℓ_i is the length of wire section i , $A_c = \pi(D/2)^2$ is the cross sectional area of the wire, D being the diameter of the nanowire. Note that two of the sections, at either end of the nanowire, play no part in the electrical properties of the network as they are 'dead-ends' for current flow⁸⁵. There is the unlikely scenario where the end of the wire may touch another horizontally as opposed to forming an overlap junction, essentially forming a "T" junction. This

scenario is not considered in the mapping as it accounts for a negligible number of junctions overall.

The inter-wire connection points, which partition the wire segments, are the nodes in the new node-voltage mapping which we shall call Multi-Nodal Representation henceforth. For each inter-wire junction, there are two connection nodes, one on each wire, and are connected by a junction resistor. Adjacent connection nodes on the same nanowire are joined with an nanowire resistor. A sketch of a simple NWN and the corresponding MNR graph representation is presented in Figure 3.1(b). The total number of nodes in this scheme is $2N_j$, where N_j is the total number of junctions in the network. The nanowire resistor between the nodes C_2 and C_4 is depicted in yellow and the two junction resistors are shown in black. Note that contributions from the wires' dead-ends are not included in this representation either. Unlike the JDA model, the locations of the wires and their intersections in the network have to be considered in the MNR model as the distances between adjacent connection nodes are needed for the calculation of nanowire resistances.

In chapter 2, the junction density was related to the wire density in a network by $n_j = \omega L^2 n_w^2$ meaning that the total number of junctions is $N_j = \omega L^2 N_w^2 / B$ where L is the length of each wire, B is the total area of the NWN and ω is a constant $\approx 0.316^{84,85}$. The Kirchhoff matrix for the JDA model of a network is of size $N_w \times N_w$ representing a system of N_w linear equations. In the MNR model, the Kirchhoff matrix is of size $2N_j \times 2N_j$ representing $2N_j = 2\omega L^2 N_w^2 / B$ linear equations. The computational memory to store a set of $2N_j$ linear equations in the MNR model is an order of magnitude higher than needed for the JDA model, i.e. $O(N_w^2)$ for the MNR versus $O(N_w)$ for the JDA. Herein lies a disadvantage of the MNR model as the required computational memory quickly becomes too demanding for dense networks.

In both JDA and MNR the computational simulations conducted in random NWNs are performed as follows: a number of nanowires are randomly distributed over a predefined area. An inter-wire junction is assigned where two wires inter-

sect; the positions and associated wires of each intersection are recorded. The MNR and JDA mappings can then be applied to the NWN with the connectivity profile and the wire positions. The Kirchhoff matrix for both can be formulated and numerically solved to calculate the sheet resistance (R_s) of the network. The same network can be recreated a number of times by fixing the random number generator seed used to generate the positions and orientations of wires in simulations. This allows the impact of particular network parameters to be assessed on a fixed geometry. Likewise, a network ensemble can be created by shuffling the wires over the device area. The two models are an excellent tool to determine the effect of all of the underlying properties on the resulting sheet resistance of the NWN.

The parameters of the NWN can be grouped into two main categories: the geometric and the resistive parameters. The geometric parameters are those that affect the connectivity profile of the NWN, e.g. the wire density (n_w) and the wire length (L). Wire diameters are not used to determine the intersection of two nanowires and so is not included as a geometrical parameter but it does affect the inner-resistances of the wires. A change in one of these parameters will alter the connectivity profile of the NWN. For example, two networks with the same wire lengths and densities can have vastly different sheet resistances due to stochastic fluctuations in wire position and orientation. Monte Carlo simulations are then performed whereby a large number of NWNs are generated for a given wire density and wire lengths and so the effect of each parameter can be determined. The resistive parameters do not necessarily alter the connectivity profile of the NWN but change the magnitude of the resistors in the network. These are the junction resistance (R_j), and the inner-wire resistance ($R_{in}(\rho, \ell_i, D)$). The effect of these parameters are best illustrated by fixing a NWN connectivity profile and calculating the change in sheet resistance associated with changes to these parameters. The relationship between these two categories of parameters and network sheet resistance will be explored in the proceeding sections.

3.2 THE IMPACT OF INNER-WIRE RESISTANCE

This section will highlight the impact of inner wire resistance on the dependence of a NWN sheet resistance and is a benchmark for further simulations later in the thesis, namely in chapter 4 where the accuracy of a novel effective lattice for a NWN is examined. The resistive properties of nanowires are not considered to alter the connectivity of a given NWN geometry but they do impact on the resistance values of the network. Both JDA and MNR were applied to the same network geometry in order to keep the connectivity profile fixed and allow for a direct comparison between models. Figure 3.2 is a visualisation of the simulated network which is of size $20\mu\text{m} \times 20\mu\text{m}$, $L = 7\mu\text{m}$, and $n_w = 0.4 \text{ nanowires}/\mu\text{m}^2$. This network will be the benchmark geometry used to identify the dependence of the sheet resistance (R_s) on R_{in} by changing ρ , D and R_j in this section.

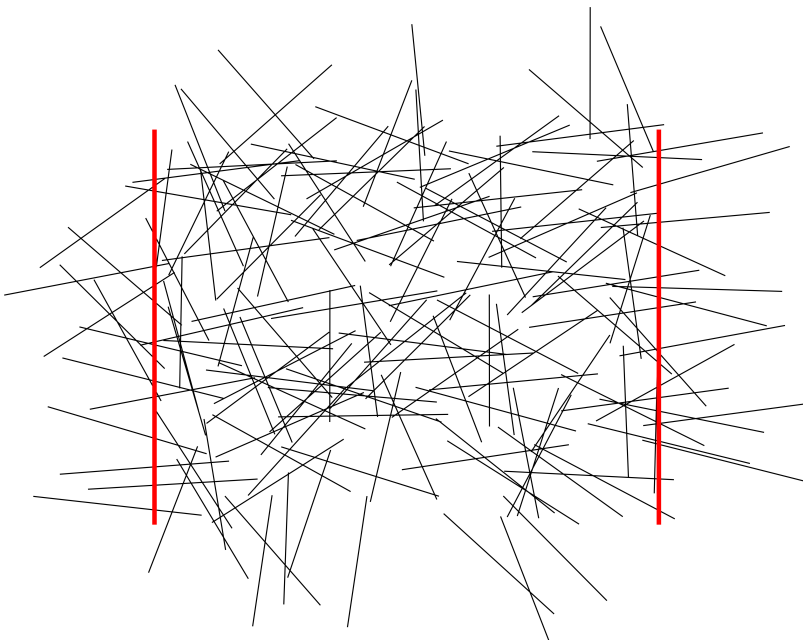


Figure 3.2: A visualisation of a simulated network to be used as a fixed geometry to determine the role of resistive parameters on network conductivity. Wires (black lines) are $7\mu\text{m}$ in length and the wire density is $0.4 \text{ nanowires}/\mu\text{m}^{-2}$. The network has dimensions $20\mu\text{m} \times 20\mu\text{m}$ and the electrodes are represented by the thick vertical red lines located at either sides of the network.

3.2.1 The Relationship Between Junction and Network Resistances

The common resistive parameter between MNR and JDA is the junction resistance. In this comparison between the models, every junction resistance was assigned the same value R_j . The resistivity and wire diameters were fixed in the MNR to values typical of Ag/PVP core-shell nanowires, $\rho = 22.6 \text{ n}\Omega\text{m}$ and $D = 50 \text{ nm}$ ⁷⁹. Figure 3.3 shows the effect of increasing R_j on the calculated sheet resistance for both the MNR and JDA models applied to the network geometry shown in Figure 3.2.

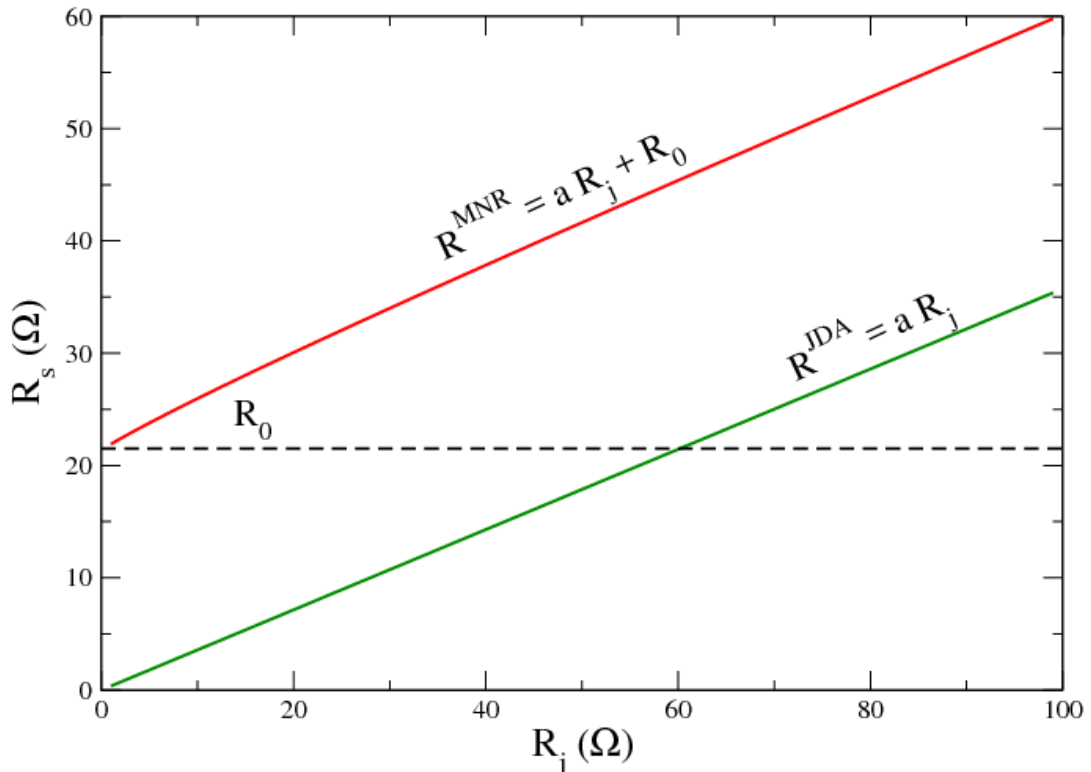


Figure 3.3: The effect of junction resistance on the sheet resistance of the network shown in Figure 3.2. The sheet resistance R_s depends linearly on the junction resistance for both the MNR and JDA models in the case of homogeneous junction resistances. In fact the slope of both lines (a) is the approximately the same for both models at $a = 0.37$. The effect of the nanowire resistance in the MNR manifests as the addition of a constant R_0 and corresponds to R_s^{MNR} with $R_j \rightarrow 0$.⁷⁹

A striking feature of Figure 3.3 is that the sheet resistance predicted by the MNR and JDA depends linearly on the junction resistance with the same slope as

$$R_s^{\text{JDA}} = \alpha R_j \quad (3.2.1)$$

$$R_s^{\text{MNR}} = \alpha R_j + R_0 \quad (3.2.2)$$

where $\alpha = 0.37$. The MNR result is offset from the JDA approach by $R_0 = 21 \Omega$ corresponding to the internal resistance of the nanowires. This linear dependence is for an idealised homogeneous junction resistor distribution and is shown to not hold when a level of disorder is introduced to junction resistances in section 3.4. The JDA functional form behaves as desired; one expects a sheet resistance of zero if every junction in the network has an idealised zero resistance. Similarly the MNR functional behaves as expected; as the junction resistance is brought to zero, the sheet resistance tends to the nanowire resistance contribution of the network R_0 . The inclusion of the nanowire resistance increases the sheet resistance of the NWN as expected. For example, in the MNR model the $R_s \rightarrow R_0 \rightarrow 21\Omega$ for $R_j \rightarrow 0$. In order to achieve this sheet resistance in the JDA, the junction resistance required is $R_j = 21/\alpha \approx 60\Omega$. This difference between the required R_j in both models can cause their overestimation when comparing simulations and experiments. This point is discussed further in section 3.3.

The value of the slope for both models gives an understanding of the nature of current flow through the NWN. A NWN is a mesh of parallel paths between the two electrodes, all of varying lengths. A simple interpretation of current flow through the NWN is that there are Y parallel paths of X junction resistors in series. X and Y are characteristic parameters unique to each network. Assuming that the paths do not superimpose on each other, the sheet resistance of such a network in the JDA model is,

$$R_s = \frac{X R_j}{Y} \quad (3.2.3)$$

Comparing this to equation 3.2.1 shows that $\alpha = \frac{X}{Y}$. Thus for $\alpha < 1$ we can argue that the current flow through the NWN is through many parallel paths Y , more paths than the number of junctions connected in series X . If $\alpha > 1$ then the current flows through few paths between electrodes. One expects that α depends on the connectivity profile, where highly connected NWNs will have a much lower slope than sparse networks.

A symmetry argument can be made to explain the linear relationship between R_s and R_j in the JDA. If the only difference between two networks is a constant shift of every resistors value then the resistance between any nodes in the network should shift by the same amount. A mathematical proof of this can also be made by making use of the Kirchhoff Matrix formalism defined in chapter 2. If every resistor in the NWN has the same value R then the Kirchhoff matrix is

$$K = \frac{1}{R} \mathcal{L} = \Gamma \mathcal{L} \quad (3.2.4)$$

recalling that \mathcal{L} is the Laplacian matrix defined in chapter 2 and $\Gamma = 1/R$. The Kirchhoff matrix, along with the current vector (\vec{I}) which defines the sourced and drained current to the network, is used to solve the potential at each node in the network. Consider the case where $R = 1$, Kirchhoff's system of linear equations are

$$\mathcal{L} \vec{V}^{\mathcal{L}} = \vec{I} \quad (3.2.5)$$

where $\vec{V}^{\mathcal{L}}$ is the solution to this equation. The resistance between the source current node (node m) and the drain current node (node n) is

$$R_{mn}^{\mathcal{L}} = \frac{|\vec{V}_m^{\mathcal{L}} - \vec{V}_n^{\mathcal{L}}|}{i_0} \quad (3.2.6)$$

where i_0 is the amount of current injected and drained from those nodes. Now consider the case where $R \neq 1$ and the current vector is the same as before. We now have

$$K\vec{V} = \frac{1}{R}\mathcal{L}\vec{V}^k = \vec{I} \quad (3.2.7)$$

Using equation 3.2.5 we can equate $\frac{1}{R}\mathcal{L}\vec{V}^k = \mathcal{L}\vec{V}^L$ and so the solved voltage vectors are related by

$$\vec{V}^k = R\vec{V}^L \quad (3.2.8)$$

The resistance between the two nodes m and n are now

$$R_{mn}^k = R \frac{|\vec{V}_m^L - \vec{V}_n^L|}{i_0} \quad (3.2.9)$$

proving that the resistance between two nodes in a network of identical resistors depends linearly on their resistance assuming that current flow does not alter course.

3.2.2 The Effect of Nanowire Resistivity and Diameter on Network Resistance

The inner-wire resistance only plays a role in MNR and so JDA simulations cannot be performed for these parameters. Their effect on R_s was determined by applying the MNR model to the NWN pictured in Figure 3.2 with $R_j = 11 \Omega$. Figure 3.4(a) shows the effect of changing the resistivity on the sheet resistance. R_s clearly increases in a linear fashion with respect to increasing resistivity which can be attributed to the linear dependence of the resistance of wire segments on the resistivity thus shifting R_0 in the linear formula for R_s given in equation 3.2.2.

Figure 3.4(b) shows the effect of increasing wire diameter (D) on the sheet resistance of the same network. The sheet resistance decreases as a power law relationship, $R_s = cD^{-2} + aR_j$, which is as expected as the nanowire resistance depends

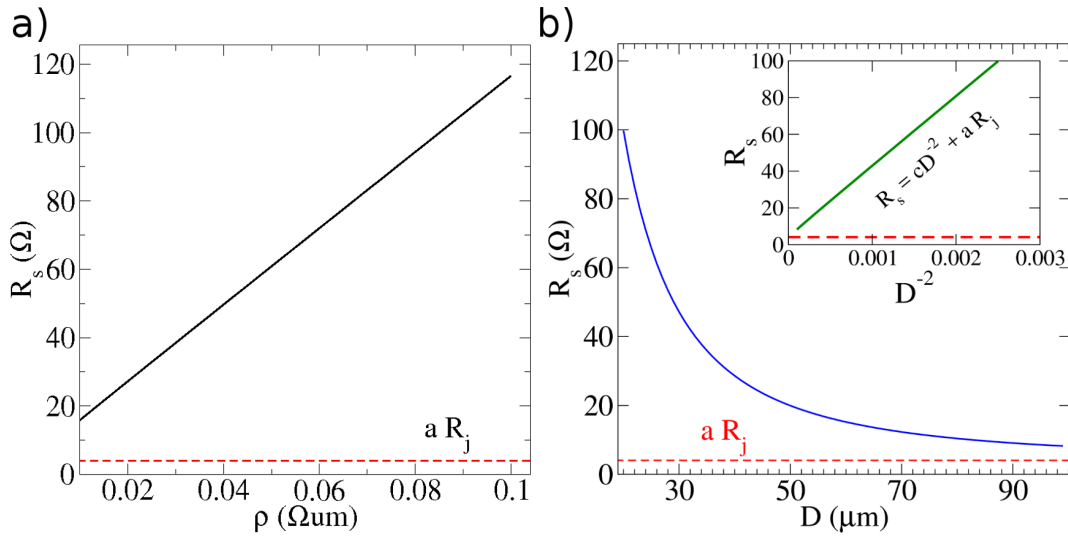


Figure 3.4: (a) The dependence of R_s on the resistivity of the nanowires, specific to the network geometry shown in Figure 3.2. R_s depends linearly on the resistivity of the nanowires. (b) The dependence of R_s on the diameter of the nanowires (D). This relationship follows that of the nanowire resistance on D with a D^{-2} dependence. In the inset, the same data is replotted in green, the x axis has been recast as D^{-2} highlighting the linear relationship between the sheet resistance and D . Recall $R_s = aR_j + R_0$ and so the sheet resistance tends to a non-zero value determined by the junction resistance for vanishing nanowire resistance. The horizontal dashed line in both plots represents the sheet resistance with no nanowire resistance $R_s = aR_j \approx 4.07\Omega$ for $R_j = 11\Omega$

on the wire diameter in this way. This inverse squared relationship is clearly evident in the inset plot which is the same data with the x axis recast as D^{-2} . Note that a non-zero junction resistance was used in simulations and so the sheet resistance tends to a non-zero value for vanishing resistivity and infinite wire diameter, $R_s \rightarrow aR_j$ as $R_0 \rightarrow 0$. This asymptotic sheet resistance is represented by the dashed horizontal line in both plots of Figure 3.4. If one were to consider a NWN with perfectly conductive junctions ($R_j \rightarrow 0$) then a symmetry argument similar to that used to describe the linear dependence of R_s on R_j can be used to describe the relationship $R_0 \propto \rho D^{-2}$.

An important note should be raised about these symmetry arguments however, they assume that current flow does not redistribute through the network as alter-

ations occur in the network. It is not inconceivable that in the MNR an increase in junction or nanowire resistances could cause the current flow to alter course thus causing a shift in the sheet resistance that does not follow the existing linear relationship.

3.2.3 *The Impact of Wire Density on Nanowire Network Resistance*

Altering either the wire density or the wire length of a network results in a fundamental change in its connectivity profile. This change is best illustrated by the expression for the junction density derived in chapter 2, $n_j = \omega L^2 n_w^2$, as it is the junctions that determine the connectivity profile. Recall from the definitions of the JDA and MNR that the junctions are a source of resistance and determine the graphical representations of the NWNs.

The impact that geometric parameters have on the connectivity profile of the networks is also described by Percolation theory⁴⁶. As discussed in chapter 2, Percolation theory can be used to determine quantities such as the critical wire density, $(n_w)_c$, below which a connective path does not form between two boundaries, or electrodes. This is described using the equation⁴⁸

$$(n_w)_c = 5.63726L^{-2} \quad (3.2.10)$$

Note that equation 3.2.10 only holds for networks where all sticks are of equal length L . This relationship links the wire density and length at the point of criticality and shows how the geometric parameters alter fundamental aspects of network systems. As the connectivity profile is altered in a random manner with a change in wire density, ensembles of simulations are required. The relationship between sheet resistance and the geometric parameters are then determined through averaging quantities and statistical analysis performed on the simulation ensemble.

The effect of wire density on the average $\langle R_s \rangle$ calculated in JDA (blue) and MNR (red) for an ensemble of NWNs is displayed in Figure 3.5(a). Other parameters were set to values measured for Ag/PVP core shell nanowires⁷⁹ that were used in the previous section: $L = 7 \mu\text{m}$, $R_j = 11 \Omega$, $D = 50 \text{ nm}$, and $\rho = 22.6 \text{ n}\Omega\text{m}$. Twenty simulations were performed for a given wire density in order to obtain an accurate calculation of the average R_s and the associated 95% confidence interval.

From Figure 3.5(a) the MNR model has a higher sheet resistance than for the JDA model at the same densities. This is due to the inclusion of nanowire resistance for the MNR and the junction resistances being the same in both models. There is large uncertainty for the average $\langle R_s \rangle$ for simulations at lower densities ($< 0.2 \text{ nanowires}/\mu\text{m}^2$) due to being close to the critical density of $(n_w)_c = 0.11 \text{ nanowires}/\mu\text{m}^2$ according to equation 3.2.10. A sparse network is susceptible to the stochastic spatial effects of the network and the large uncertainty in the sheet resistance is a manifestation of this randomness. The general decreasing trend of the sheet resistance with increasing nanowire density is a result of additional pathways developing across the network.

According to Percolation theory⁴⁶, the sheet conductance, Γ_s , of a random stick network scales as a power law with the stick density near the critical value as:

$$\Gamma_s \propto (n_w - (n_w)_c)^{-\beta} \quad (3.2.11)$$

where $(n_w)_c$ is the critical wire density. This scaling law has been well documented in simulations^{46,48,49} and has been used to understand the resistive properties of carbon nanotube^{12,95} and metallic nanowire networks^{83,91}. Figure 3.5(b) recasts the data from panel (a) in a log-scale plot but alters the horizontal axis to $(n_w - (n_w)_c)$ for comparison with the power law in equation 3.2.11. Both MNR and JDA have a power law response to the increase in wire density that is easily identifiable in this plot and were fit to both curves. The two models were found to have differing exponents in their power law fits, $\beta_{\text{MNR}} \approx 1.28$ (black dashed line) and $\beta_{\text{JDA}} \approx 1.44$ (green dashed line). These differing exponents are in line with those

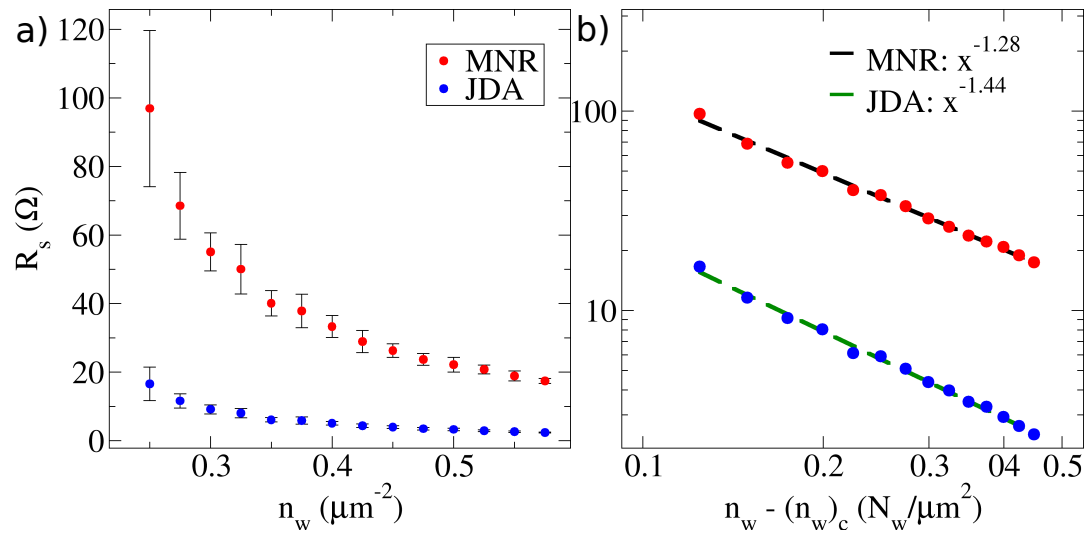


Figure 3.5: (a) The effect of changing wire density n_w on sheet resistance R_s for networks of size $20\mu\text{m} \times 20\mu\text{m}$ and wires of length $7\mu\text{m}$. The wire resistivity, cross sectional area and junction resistance are those measured typical for Ag/PVP core shell nanowires. 20 random networks were simulated for each wire density in both MNR and JDA and the average sheet resistance and 95% confidence interval for each wire density was calculated and plotted. (b) Sheet resistance versus the parameter $x = (n_w - (n_w)_c)$ for comparison with equation 3.2.11. Here the two scaling regimes between R_s and n_w is evident for both models. Power-laws were fit to both models and are shown as dotted lines. For the MNR model the scaling exponent according to regression analysis is $\beta_{MNR} \approx 1.28$ and the fitted curve is shown as the black dashed line. The JDA line has an exponent $\beta_{JDA} \approx 1.44$ and is shown as the green dashed line.

seen in Monte Carlo simulations that have been reported in the literature⁴⁸. Li and Zhang showed that the scaling exponent depends on the ratio of junction resistance (R_j) to nanowire resistance (R_{in}). By fitting the Error function to Monte Carlo simulations they found the relationship between the scaling exponent and $\zeta = \log_{10}(R_j/R_{in})$ was

$$\beta = \beta_0 + C \operatorname{erf}(\zeta) \quad (3.2.12)$$

where $\beta_0 = 1.314 \pm 0.002$ and $C = 0.108 \pm 0.003$. In the limit of vanishing nanowire resistance, i.e. the JDA model, the exponent is $\beta_{JDA} \approx 1.422$. For the MNR model, the resistance of a nanowire of length $7\mu\text{m}$, $D = 50\text{ nm}$, and $\rho = 22.6\text{ n}\Omega\text{m}$

is approximately 80Ω making $\beta_{MNR} = \beta_0 + C \operatorname{erf}(\log_{10}(11/80)) \approx 1.23$. These exponents are very close to those found in Figure 3.5 and further illustrate the importance of including nanowire resistance in calculations of the sheet resistance for networks where R_{in} is non-negligible.

3.3 DIGITAL REPRESENTATION OF PHYSICAL NANOWIRE NETWORKS

A key problem in comparing experimental measurements with computational simulations for nanowire networks is the need to generate an accurate numerical average. A large number of laborious simulations are required for a meaningful benchmark to compare to and even then a physical sample could have resistances in the extreme tails of expected outcomes, particularly for sufficiently low junction density networks. To combat the need for multiple simulations and to allow a more direct comparison with physical samples we developed a method to digitise the geometry of an SEM image of a NWN. This was achieved by opening the micrograph image of a NWN on a digital canvas where the start and end positions of each wire were recorded. The wire is represented as a straight line between these points in the digital version of the NWN. A computational routine to detect intersections of the digital wires is performed to determine the positions of junctions and to create an approximation of the connectivity profile of the physical NWN. With the positions of each wire and inter-wire junctions a ‘top-down’ two-dimensional representation of the NWN can be created digitally. Figure 3.6(a) shows a typical SEM image of a NWN comprising of Ag/PVP core-shell nanowires and Figure 3.6(b) is its digitised version. The digital version of the network is an approximation. From the top-down view of the SEM image it is impossible to tell if an overlap of wires results in physical contact between them, particularly in areas of high wire density where a wire may become suspended above another wire giving the appearance of

a junction but in reality there is none. This approximation works particularly well for relatively sparse networks in which there are a small number of wires piling up perpendicular to the NWN, in the Z direction.

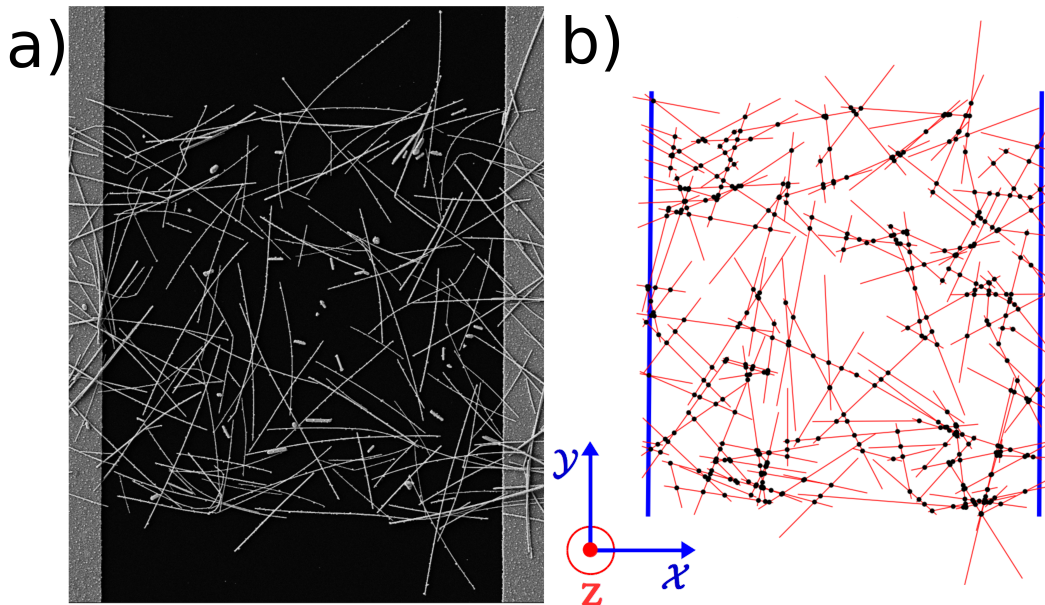


Figure 3.6: (a) An SEM of a physical nanowire network that is roughly $20 \mu\text{m} \times 20 \mu\text{m}$ in size. Nanowires can be seen against the black background with electrodes seen to the left and right side of the network. (b) A representation of the digitised NWN depicted in (a), the network has a wire density $0.37 \text{ NW}/\mu\text{m}$ and 440 junctions. Black dots represent inter-nanowire junctions and the blue vertical lines represent the electrodes⁷⁹.

The sheet resistance of the NWN in Figure 3.6(a) was measured experimentally as $R_s^{\text{EXP}} = 42.9 \Omega$. By analysing the dependence of R_s on R_j for both MNR and JDA simulations for the digitised network, one can identify a characteristic junction resistance that will lead to the observed experimental sheet resistance. Each junction in the digitised NWN was assigned a resistance R_j and wires in the MNR assigned the measured resistivity $\rho = 22.6 \text{ n}\Omega\text{m}$ and diameter $D = 50 \text{ nm}$ for Ag/PVP nanowires. R_s was calculated for both models and this process was repeated for many values of R_j , the results of which are plot in Figure 3.7. Also shown in Figure 3.7 is the experimental sheet resistance R_s^{EXP} and is represented by the horizontal dashed line. Where it intersects with the JDA sheet resistance curve (R_s^{JDA}) and the

MNR sheet resistance curve (R_s^{MNR}) provides two characteristic junction resistances, $R_j^{JDA} \approx 96.9 \Omega$ and $R_j^{MNR} \approx 52.9 \Omega$. The difference between the characteristic junction resistances is sizable, $\Delta R_j = 44\Omega$, illustrating the large impact the nanowire resistance has on the sheet resistance of the network.

As seen in section 3.2, the two resistive curves offer much insight into the behaviour of the network. Recall that the equations for R_s in terms of R_j for both models are

$$R_s^{JDA} = aR_j \quad (3.3.1)$$

$$R_s^{MNR} = aR_j + R_0 \quad (3.3.2)$$

where the fitting parameters are $a = 0.443$ and $R_0 = 16.2 \Omega$ for the sample in Figure 3.6. Recall that the slope of the line a can be used to understand how current flows through the NWN, either through a few or a large number of paths in the network. In this case $a \approx 0.443$ leading to the conclusion that current flows through many parallel paths, more paths than resistors in characteristic paths between electrodes.

The experimental sheet resistance for thirty electrically stressed samples were measured and their network geometry were digitised. R_s versus R_j curves were generated for each of the digitised network geometries in the same manner as in Figure 3.7. The linear equations for R_s outlined in equation 3.3.2 were applied to each digitised network and their characteristic junction resistances were obtained as well as the slope a and R_0 . These values are listed for each sample in Table A.1 in Appendix A. Note that the junction resistances appear in the range $2.28 \leq R_j^{MNR} \leq 152 \Omega$ and R_j^{JDA} in the range $42.35 \leq R_j^{MNR} \leq 185.91 \Omega$, once again showing the sizable impact that the inclusion of inner-wire resistance takes on a network system. The characteristic junction resistances obtained by the MNR simulations are taken to be a more accurate estimate for the junction resistances of Ag/PVP nanowire junctions.

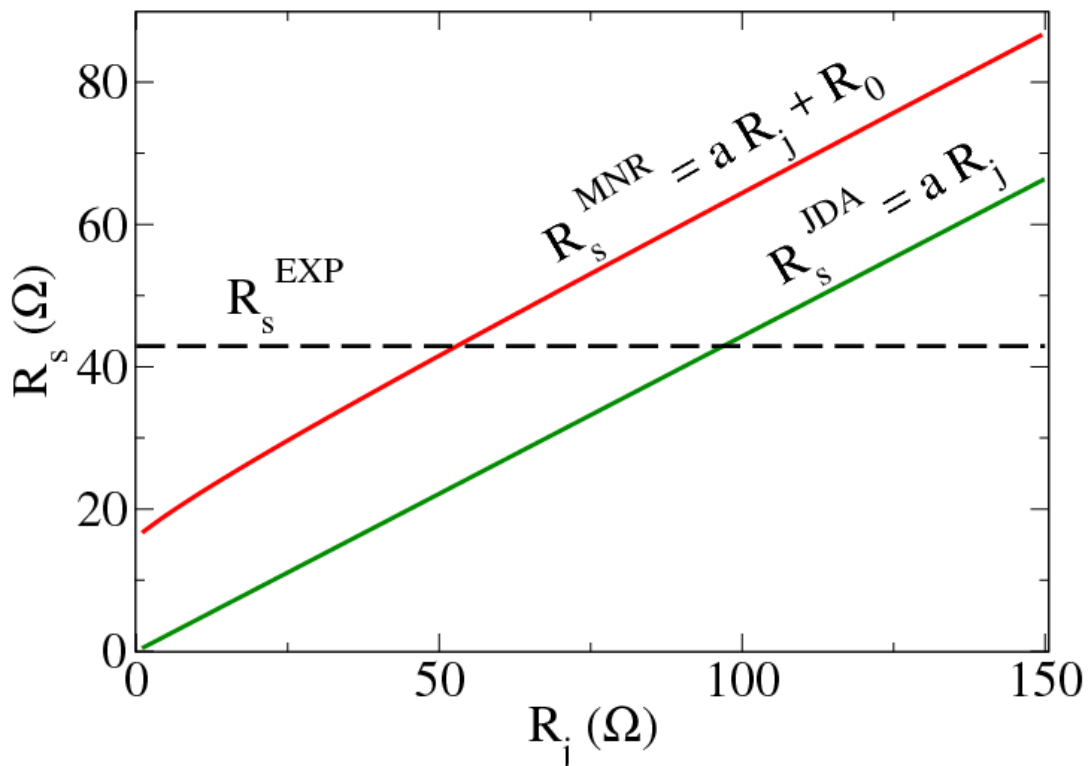


Figure 3.7: The relationship between the sheet resistance of the digitised network in Figure 3.6(a) using MNR and JDA models with increasing junction resistance (R_j). One finds $R_s^{MNR} = aR_j + R_0$ and $R_s^{JDA} = aR_j$ where $a = 0.443$ and $R_0 = 16.2 \Omega$ from regression analysis. The horizontal line represents the sheet resistance that was experimentally measured for this sample, 42.9Ω . The value for R_j required for the MNR and JDA to obtain a sheet resistance corresponding to that measured in experiment are identified as $R_j^{MNR} = 52.9 \Omega$ and $R_j^{JDA} = 96.9 \Omega$.

The calculation of the characteristic junction resistance assumes that the resistances in the network are identical which is not the case in reality. The resistances of several individual Ag/PVP nanowire junctions that had been electrically stressed or thermally annealed were measured (R_j^{EXP}). The distribution of recorded resistances is shown in Figure 3.8 as the green dotted bars⁹². The majority of junctions were found to have resistances less than 70Ω , however there were two junctions whose resistance were very high with values in the range $200 - 300 \Omega$. These two measurements represent 6.25% of the measured junction resistances. There is a clear spike in frequency of junction resistances in the range $10 - 20 \Omega$ and the median junction resistance of 11Ω occurs in this bin. Figure 3.8 also shows the

distribution of the characteristic junction resistances from the MNR model (R_j^{MNR}) for the experimental samples and are represented by orange solid bars. The distribution of R_j^{MNR} has a mean value 44.9Ω and median value of 38.4Ω , which is visibly higher than the distribution of R_j^{EXP} for individual junctions. While it is higher than the measured sheet resistance it does show that the characteristic junction resistance is of the correct order of magnitude of tens of Ohms. The inclusion of nanowire resistance in simulations results in a more accurate characteristic junction resistance; recall that the MNR resistances values are always smaller than those found with JDA. Again it should be stressed that the transport regimes of a single junction and a network of junctions are very different and the random connectivity profile of the network will have an impact on the calculation of R_j^{MNR} meaning that it should be viewed as an estimate only.

The contribution of the sheet resistance due to that of the nanowire sections is captured by the quantity R_0 and represents the ultimate conductivity of a network, where all of the junctions have been annealed to a perfectly conductive state. R_0 is listed for each of the thirty samples in Table A.1, where each network has a contribution in the range of $8.9 \Omega \leq R_0 \leq 92.05 \Omega$. To quantify the potential for junction annealing in a network, a dimensionless optimisation-capacity coefficient (γ) was introduced⁷⁹ that illustrates how close a network is to its ultimately conductive state,

$$\gamma = 1 - \frac{R_0}{R_s^{EXP}} \quad (3.3.3)$$

where γ varies between zero and one. Values of γ close to one indicate the conductance of the network can be considerably improved by altering the values of R_j . When γ is nearer to zero, the network is near its optimum conductivity, i.e. the skeletal nanowire resistance R_0 , as all of the junctions in the network have been annealed into a perfectly conductive state. This metric provides fabricators of NWNs with an idea of the potential improvement possible in a particular network.

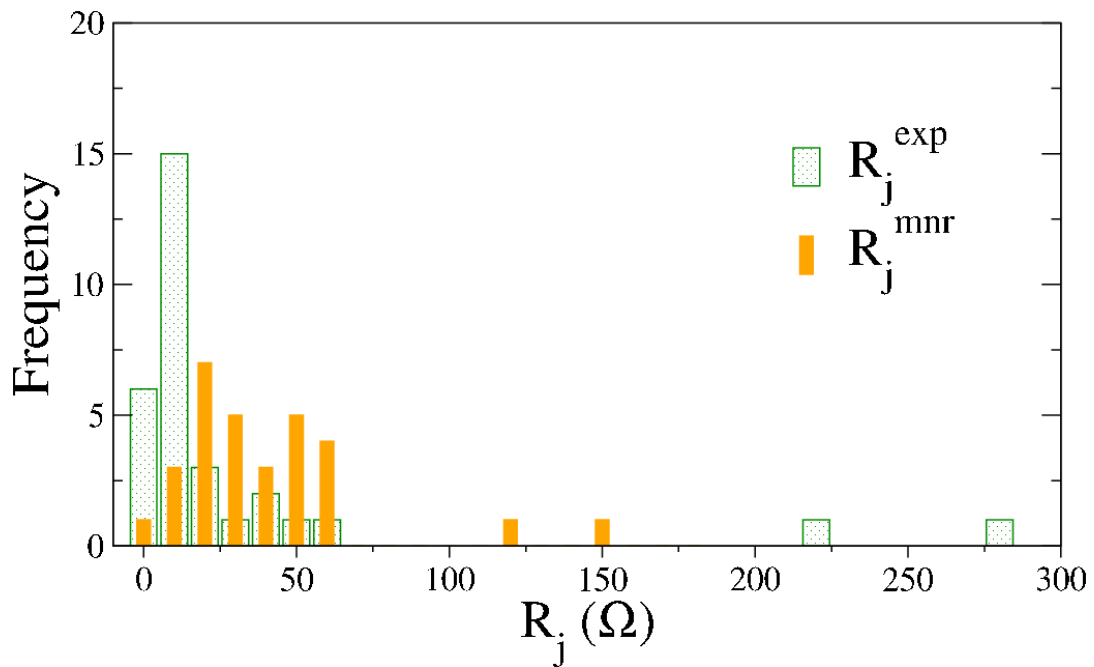


Figure 3.8: The distribution of resistances measured for thirty two individual nanowire junctions are shown by the green dotted bars⁹². There is a clear spike in frequency at the median resistance of $11\ \Omega$. The distribution of the characteristic junction resistances that were determined using MNR simulations and shown as thin solid orange bars. The average resistance is $44.9\ \Omega$ and median value is $38.4\ \Omega$, of the same order of magnitude as that measured experimentally. The bin sizes are of size $10\ \Omega$ for both distributions. NOTE: MAKE MNR/EXP CAPITALS

Table A.1 in Appendix A contains the wire density, sheet resistance and other parameters for all thirty of the processed experimental samples. In this table the outcomes of the digitisation techniques on the analysis of network properties are collected in one database. Looking at the optimisation-capacity coefficient in particular, no obvious correlation exists between γ and n_w , R_0 , or R_s^{exp} . This suggests that each of the networks had their junctions improved in a consistent manner, i.e. annealing was not more effective for sparse networks say. However a relationship between γ and R_j^{MNR} is expected as it is an estimate to the junction resistances in the network. Thus γ increases with increasing characteristic junction resistance which is shown in Figure 3.9.

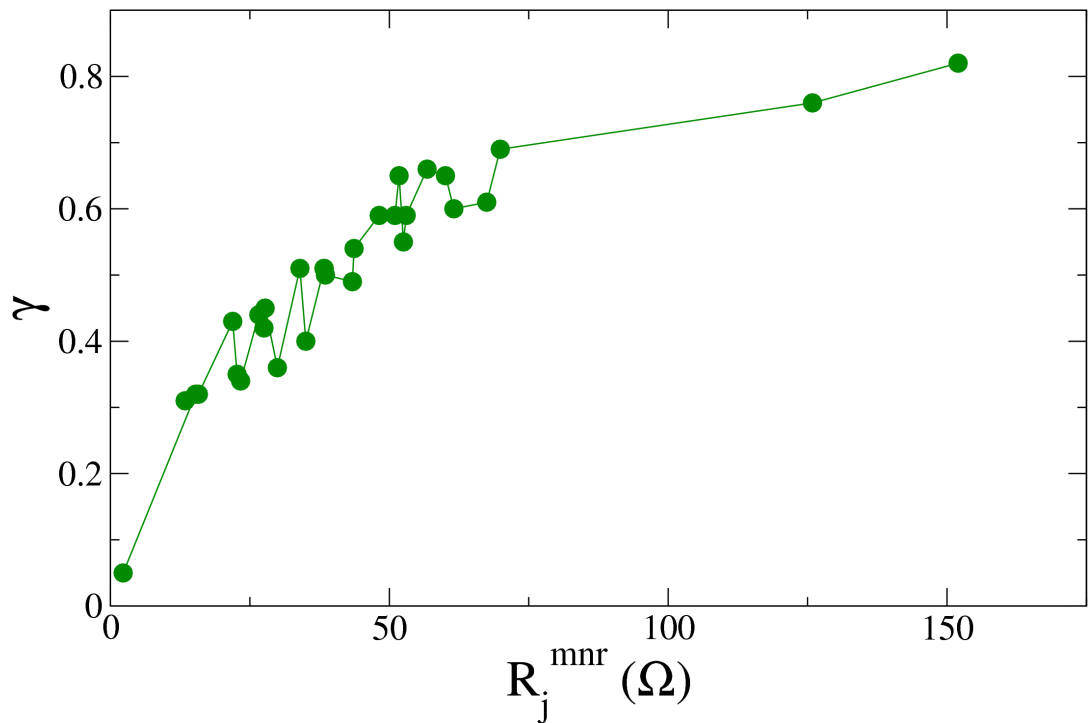


Figure 3.9: The Optimisation Capacity Coefficient (γ) versus the MNR characteristic junction resistances (R_j^{MNR}) for the thirty experimental NWN samples shown in Table A.1 in Appendix A⁷⁹.

The importance of including nanowire resistivity in comparisons between computational simulations and experimental measurements was demonstrated in this section through the MNR model. Not only does the MNR model more accurately estimate the resistance of electrically stressed junctions it also identifies the ultimate conductivity of a network, that which is limited by the skeletal nanowire resistance. The simulation results unique to each experimental sample presented in this chapter are numerical and take a great deal of sample processing to obtain. In the following chapter an analytical approximation using methods outlined in chapter 2 for the sheet resistance in terms of the fundamental properties are presented which provides a quick and mathematically transparent method to estimate various properties of a network.

3.4 IMPACT OF JUNCTION RESISTANCE DISORDER

Until now the main source of randomness in a NWN has been the spatial orientations of nanowires and the resulting connectivity profile of the network. However randomness can also arise in the parameters of the nanowires themselves such as the diameter and resistivity⁷⁹. In the previous section we showed that the resistance of individual annealed junctions took on many different values in the distribution presented in Figure 3.8, showing that junction resistances are another source of disorder. In this section we will examine the effect that fluctuations in junction resistances can have on the macroscale NWN resistance. Junction resistance distributions are determined by a normal distribution that is confined to the range $(0, \infty)$ with a standard deviation σ and a fixed mean value $\langle R_j \rangle$. The truncation is applied to the distribution to remove any negative resistances from simulations. The average of an ensemble of thirty sets of junction resistance distributions on an identical network geometry were used to calculate an average sheet resistance and confidence interval for each $\langle R_j \rangle$ and σ . The network geometry used in these simulations is that of sample #1 from Table A.1 and has an experimental sheet resistance $R_s^{\text{EXP}} = 84.42$.

Figure 3.10 presents the results of simulations, the top panels are the average sheet resistances R_s for a given $\langle R_j \rangle$ with three different standard deviations, $\sigma = 0 \Omega$ (black line), $\sigma = 20 \Omega$ (blue dashed curve), and $\sigma = 40 \Omega$ (green curve). Panel (a) corresponds to the JDA mapping and panel (b) to the MNR mapping for simulations. An interesting behaviour is seen for the normal distributions with $\sigma \neq 0$, the relationship between R_s and $\langle R_j \rangle$ are not linear as is the case for $\sigma = 0$. For small $\langle R_j \rangle$ the networks with junction resistance dispersion are much higher in resistance than the $\sigma = 0$ case, but the distributions eventually begin to converge with the linear trend of $\sigma = 0$ for high $\langle R_j \rangle$. This is due to the removal of negative resistances from the junction distributions, the asymmetry of the distribution being relatively greater for small values of $\langle R_j \rangle$.

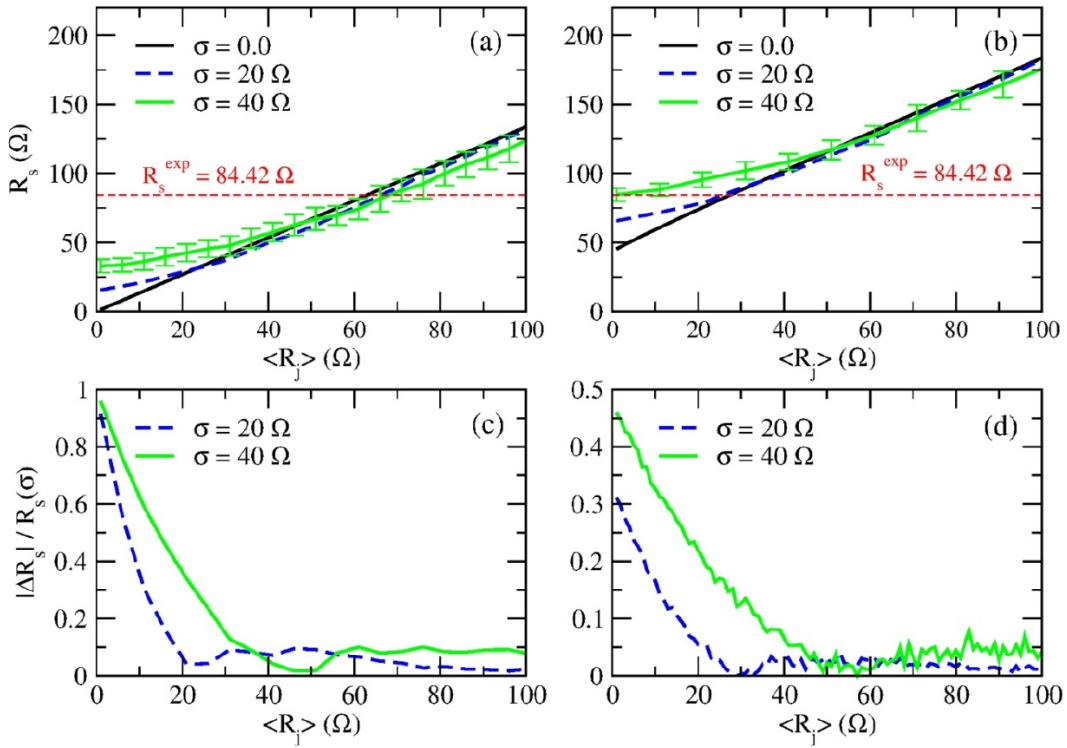


Figure 3.10: The result of including junction resistance dispersion on the calculated sheet resistance R_s for increasing mean junction resistance $\langle R_j \rangle$ for the JDA model in panel (a) and the MNR model in (b). The digitised geometry of network sample 1 from Table A.1 is used for each simulation reported here and $R_s^{\text{EXP}} = 84.42$ is displayed by the red dashed line in panels (a) and (b). The junction resistances follow Normal distribution confined to the range $(0, \infty)$ and two standard deviations are shown, $\sigma = 20 \Omega$ (green curve) and $\sigma = 40 \Omega$ (blue dashed curve). The linear relationships between R_s and $\langle R_j \rangle$ for homogeneous resistance distribution, $\sigma = 0$, are shown in black. Only error bars for $\sigma = 40 \Omega$ are shown for ease of viewing. The relative variance between the mean value of R_s for the distribution of R_j and the homogeneous simulations are shown in the bottom panels, (c) corresponding to the JDA and (d) to the MNR⁷⁹.

The bottom panels of Figure 3.10 quantifies the disagreement of R_s for the homogeneous and dispersed junction resistance distributions. The relative sheet resistance variance for the two curves representing dispersed distributions are shown for the JDA model in panel (a) and for the MNR model in panel (b). The relative variance was calculated by subtracting the curves with and without dispersion, $\Delta R_s = |R_s(\sigma) - R_s(\sigma = 0)|$ and dividing by $R_s(\sigma)$. The $\sigma = 40 \Omega$ simulations display a higher variance than $\sigma = 20 \Omega$ but both reach similar low values for large values

of $\langle R_j \rangle$. The spread in junction resistances alters the value of the characteristic junction resistance R_j^{MNR} , the value of $\langle R_j \rangle$ that gives a simulated R_s matching with $R_s^{\text{exp}} = 84.42 \Omega$ that was measured experimentally for this particular network geometry⁷⁹. The effect of junction resistance dispersion does not have a large impact in the value of R_j^{JDA} , the three simulation curves agree closely at this point in Figure 3.10(a). The dispersion does play a large role in MNR estimates of the characteristic junction resistance however. In Figure 3.10(b) the intersection of the $\sigma = 40 \Omega$ curve, or $R_j^{\text{MNR}}(\sigma = 40)$, occurs in the range $0 - 10 \Omega$ compared with $R_j^{\text{MNR}}(\sigma = 0) = 27.73 \Omega$. This demonstrates the impact resistance variance can have on the sheet resistance of a NWN, the resistance dispersion can lead to a much lower R_j^{MNR} according to the degree of this dispersion.

It should be noted that here only the junction resistance had a degree of dispersion but it has been demonstrated that Ag/PVP nanowires display a certain variation in wire diameter and resistivity also⁷⁹. As NWNs are comprised of many individual components care must be taken to account for the variability of different properties of the ensemble of nanowires that collectively form the network. In chapter 4 an approximation for the effective medium lattice of a NWN is introduced and can be used to quickly estimate the effect of introducing more complex resistance distributions on the sheet resistance of a NWN.

3.5 CHAPTER CONCLUSION

The importance of including the contribution of nanowire resistance when calculating that of a nanowire network was highlighted in this chapter. Not only did the inclusion of inner-wire resistance changes the dependence of the network on certain fundamental network properties, it determined the ultimate conductivity of a network with perfectly annealed junctions.

The electrical properties of NWNs can be calculated by mapping the NWN onto a node-voltage lattice, the electrical properties of which can be numerically solved using Ohm's and Kirchhoff's laws as discussed in chapter 2. Two node-voltage mappings were introduced in section 3.1, the Junction Dominated Approach (JDA) and the Multi-Nodal Representation (MNR). The JDA model assumes that the electrical properties of the network are dominated by the junction resistances and so the nanowire resistances are ignored while the MNR model includes them.

The dependence of the sheet resistance (R_s) on various network parameters were studied in section 3.2 and here the effect of including the inner-wire resistance on those dependencies were examined. In the MNR model wire resistivity (ρ) and wire diameter (D) was shown to relate to the sheet resistance as $R_s = C\rho D^{-2} + \alpha R_j$ where C is a constant and αR_j is the contribution of the junction resistances. A linear relationship between sheet resistance and junction resistance (R_j) was shown to hold mathematically and in simulations for JDA models of NWNs such that $R_s^{\text{JDA}} = \alpha R_j$. The same linear relationship was shown in simulations of MNR models of NWNs plus a contribution from the nanowire resistance, $R_s^{\text{MNR}} = \alpha R_j + R_0$. Since networks with the same wire density can have different connectivity profiles the need for spatial configurational averaging arose. A large number of simulations altering the wire density were performed and the corresponding average sheet resistances were plotted for MNR and JDA. A Power law relationship between sheet resistance and wire density was observed as one would expect from percolation theory. The inclusion of nanowire resistance was shown to alter the value of the exponent in the percolative power laws.

A method to capture the geometrical layout of a physical NWN sample from an SEM image was presented in section 3.3 which allows for simulations on geometries similar to the experimental samples. Thirty samples whose sheet resistance had been measured were digitised and they were used to understand the nature of current flow and junction resistances in real NWN samples. Linear expressions relating the sheet resistance and junction resistance were found for each sample

using MNR and JDA simulations and were used to determine a characteristic junction resistance, the value at which simulated R_s matches the experimental R_s^{EXP} . The characteristic junction resistance was found to be lower for MNR model than the JDA model which can be explained with the sizable impact of nanowire resistance on the network. The distribution of MNR characteristic junction resistances was compared with a distribution of single Ag/PVP junction resistances measured experimentally by Bellew et al⁹². The simulated characteristic resistances overestimated the measured junction resistances but were found to be of the same order of magnitude of tens of Ohms. Characteristic junction resistances calculated with the MNR model were more accurate than those from the JDA model further highlighting the need for nanowire resistances to describe metallic NWNs.

The ultimate conductivity of a network was shown to be limited by the contribution of the nanowire resistances in section 3.3. A measure of how much potential for conductivity improvement was introduced, the optimisation capacity coefficient (γ), and was calculated for the experimental samples. There was no direct relationship between γ and wire density suggesting that the electrical annealing process was equally effective for all of the networks. However γ did depend on the characteristic junction resistance, where NWNs with higher resistances had higher values of γ meaning there was much room for improvement.

The impact junction resistance dispersion can have on the sheet resistance of a NWN was demonstrated in section 3.4. Here it was shown that dispersion can break the linear linear relationship between R_s and R_j demonstrated in section 3.2. A digitised network geometry was used to show that the non-linear relationship between R_s and $\langle R_j \rangle$ for dispersed junction distributions can shift the characteristic junction resistance to lower values compared to estimates obtained with homogeneous simulations.

4

EFFECTIVE MEDIUM THEORY FOR NANOWIRE NETWORKS

A difficulty with NWN adaptability for use in devices at an industrial scale is their random nature. The random connectivity profile, varying junction resistances and wire resistivity all conspire to make the fabrication of a NWN with a desired sheet resistance difficult. Worse still, two NWNs comprised of identical wires and of similar wire densities can have wildly different electrical properties. This large variance is caused by two main types of disorder: the randomness with which wires are spatially distributed and the inherent fluctuations on the characteristics of the individual wires. This calls for averaging strategies that reduce the impact of these fluctuations in any calculations, requiring a large amount of computational resources to determine the average sheet resistance for fixed nanowire properties as was seen in chapter 3. With that in mind, a novel method that processes Scanning Electron Microscope (SEM) images of NWNs and captures the precise locations of all wires of a given sample was presented in chapter 3. An example of an SEM image is presented in Figure 4.1(a) and its digitised form is shown in Figure 4.1(b). This establishes the exact connectivity the NWN possesses and removes the need for averaging over the wire locations, consequently reducing the fluctuations induced by spatial disorder, but still requiring significant computational resources and processing time.

There exists no theoretical description based on real-world NWNs in which their far-from-perfect physical characteristics are accounted for in a closed-form

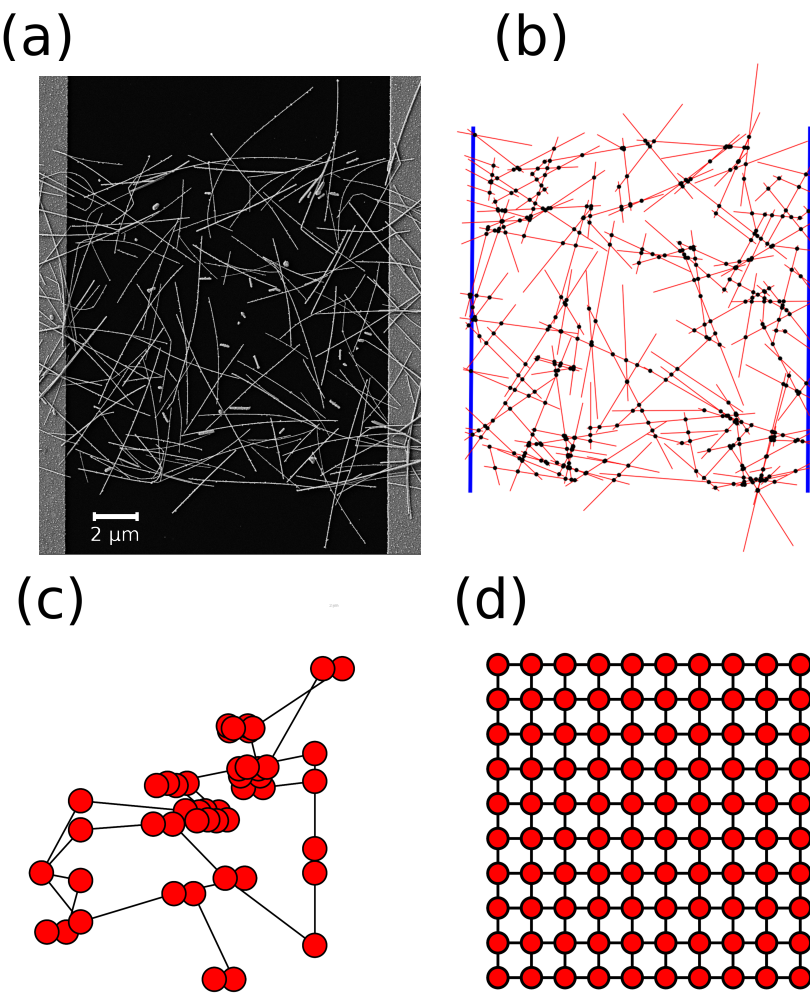


Figure 4.1: (a) SEM micrograph image of a Ag-NWN with hundreds of wires randomly distributed on top of an insulating substrate. Two electrodes on both sides of the sample, shown as vertical gray bars, are connected by numerous paths formed by the wires. (b) After the image is processed, the digitized version of the image records each wire location and provides full information about the intersection points of each wire; (c) Mathematical graph showing voltage nodes as points and connecting resistors as edges. (d) The simplified graph of a square lattice representing a regular ordered network.

mathematical representation.¹ This is typically done by means of laborious Monte-Carlo procedures used to determine universal behaviours of simplified computer-

¹ remove this line

generated NWNs^{46,48,49,96}. Indeed, such techniques are so computationally demanding that the dependence of the sheet resistance on all the possible physical characteristics of real NWN such as the wire density, material properties, connectivity, etc, can only be estimated numerically. However, closed-form analytical expressions for the conductance of ordered homogeneous networks are known⁴⁵ and was discussed in chapter 2. These are spatially ordered networks (*e.g.* square, triangular, hexagonal, etc) connected by identical resistors throughout. Whether these expressions can be of use to describe heavily disordered structures, even though they are far from ordered and homogeneous, is the question posed in this chapter. By mapping the disordered structures onto a corresponding effective square lattice as introduced in chapter 2, we can obtain the sheet resistance of NWN with an arbitrarily large density of wires. This mapping is visualised in Figure 4.1 where the resistive network graph in panel (c) is approximated by the effective square lattice in panel (d). Further manipulation of these expressions enables us to describe the conductivity of these films under real experimental conditions. In fact, we show that dense networks composed of nanowires of non-uniform lengths and diameters contacted by finite-sized electrodes can be fully described by this approach.

The sequence of this chapter is as follows. In section 4.1 a lattice Green's function is employed to derive an analytical expression between any two nodes in an infinite square lattice. This expression is shown to match numerical calculations of inter-nodal resistances on large but finite square lattices. Further to this the resistance between two nanowire junctions in a random NWN is shown to behave in a similar manner to the inter-nodal resistance in the infinite square lattice suggesting a mapping between the two systems. An Effective Medium theory (EMT) is introduced for regular lattices and is then used to determine this mapping between a square lattice and a random NWN in terms of the underlying properties of a NWN in section 4.2. Following this the lattice Green's function is generalised to a multi input/output electrode system, in particular to a system where the electrodes span opposite sides of a finite square lattice in section 4.3. In section 4.3, by combin-

ing the NWN specific EMT with the multi-electrode Green's function an analytical, closed form mathematical expression is successfully derived for the resistive properties of a NWN based on all of the relevant Nanowire properties. This expression is then used to determine various parameters and properties of NWNs that were discussed in chapter 3 in section 4.4. Finally a chapter summary is presented in section 4.5.

4.1 INTER-NODAL RESISTANCE IN A NANOWIRE NETWORK

In chapter 2 an expression for the resistance between two nodes in an infinite resistor lattice was derived using the Green's function method. Furthermore an approximation to the Green's function was derived and shown to be highly accurate for increasing separation between nodes in the lattice. Where two nodes are separated by the lattice vector \vec{r} the approximation for the inter-nodal resistance is

$$R_{nn}(\vec{r}) \approx \frac{R}{\pi} \left(\ln(|\vec{r}|) + \gamma + \frac{\ln(8)}{2} \right) \quad (4.1.1)$$

Where R is the resistance of each edge in the lattice and γ is the Euler-Mascheroni constant. Equation 4.1.1 was shown to match the inter-nodal resistance calculated in a finite square resistive lattice using Kirchhoff's and Ohm's laws in chapter 2. With an understanding of the electrical properties of inter-nodal currents in ordered resistive networks the question arises if current flow in NWNs behaves in a similar manner. In Figure 4.2 a sketch of several nanowires is shown with two electrode nodes represented by red dots. For an accurate comparison with a resistive lattice the distance metric used will be the nodal distance, or the number of resistors in the shortest path between two electrodes. Figure 4.2 is a sketch of a NWN where the shortest nodal path between two electrodes is depicted with blue arrows. The

path contains three wire segments and one inter-wire junctions making the nodal separation four.

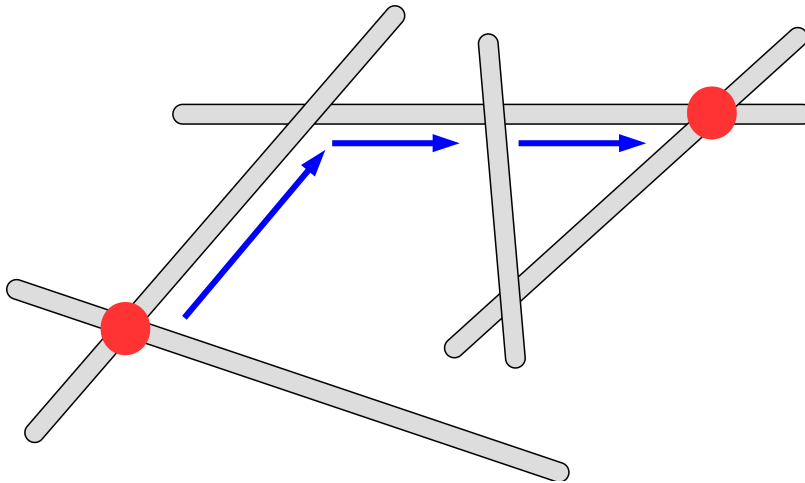


Figure 4.2: A sketch of a NWN with Nanowires represented as black lines, the two electrodes as red circles. The shortest path between electrodes is traced with the blue arrows through a single Nanowire junction and three wire segments, making the nodal separation between the electrodes four.

A large NWN with no vertical electrodes was simulated to calculate the relationship between R_{nn} and the Nodal separation using the MNR node-voltage mapping so to include inner-wire resistances. The simulated nanowires were of length $L = 7 \mu\text{m}$, junction resistance $R_j = 11 \Omega$, wire resistivity $\rho = 22.6 \text{ n}\Omega\text{m}$, and wire diameter $D = 60 \text{ nm}$. The average inter-nodal resistance for a given nodal separation is shown in Figure 4.3. Immediately one identifies that the resistance between nearest neighbours is relatively large and uncertain. This large variance is due to the nearest neighbour being either a junction or inner-wire segment which itself has a large variance as it depends on the length of that wire segment. The uncertainty decreases for increasing nodal-separation due to the fluctuations of inner-wire resistance values and junction resistances being averaged over. At larger separations the uncertainty grows once again, this is likely due to finite sized effects as the second output node begins to reach the edge of the network. There is unmistakable trend between R_{nn} and node separation which appears log-like but the initial data-

point and large error bars obscures this. The green line in Figure 4.3 corresponds to a fit of equation 4.1.1 where the effective resistance was the fitting parameter and found to be $R = 6.09\Omega$. This suggests that the inter-nodal resistance in a random NWN can be approximated using an expression derived for a regular square lattice, requiring only an appropriate effective resistance that represents both the wire segment and junction resistances. A method to calculate an effective resistance is outlined in the following section.

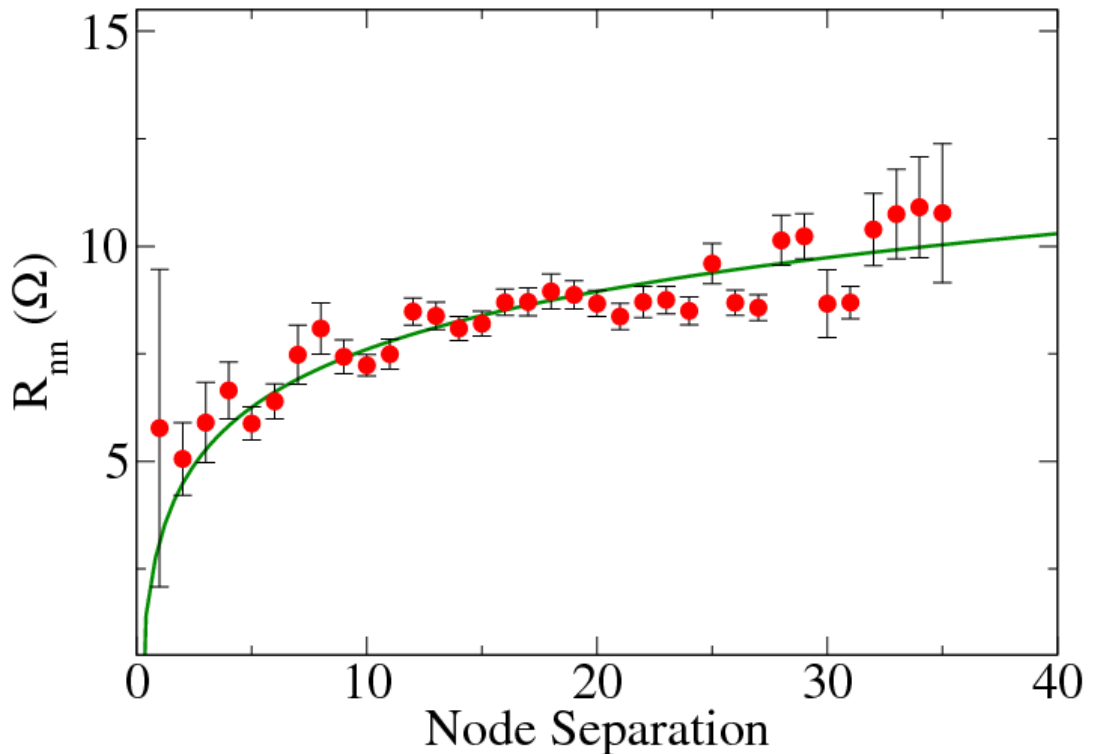


Figure 4.3: The inter-nodal resistance (R_{nn}) for a given nodal separation in a random NWN. The resistance between nodes is calculated using the MNR model, thus including the effect of inner-wire resistance. The red points correspond to the average R_{nn} for a given node separation and the error bars are 95% confidence intervals. The green line is equation 4.1.1 where $R = 6.09 \Omega$ is the fitting parameter.

4.2 EFFECTIVE MEDIUM THEORY OF A NANOWIRE NETWORK

In chapter 2 the Effective Medium Theory (EMT) for conduction in resistive lattices was introduced where a network whose resistors follow some distribution $f(g)$ can be mapped onto a homogeneous one that has the same average properties. The effective resistance is calculated such that the average resistive properties of the homogeneous and inhomogeneous networks are the same. An EMT requires an understanding of the resistor distribution $f(g)$, both the resistance values and relative proportions of each. Thankfully, there is some order to a randomly orientated nanowire network. In this section the different types of resistors in a NWN are identified and analytical expressions to calculate their percentages are derived.

In the MNR voltage mapping each node has three edges connected to it, one junction resistor and, either two inner-wire segments or a single wire segment and a ‘dead-end’. Dead ends occur at either end of a nanowire (two per nanowire), and are represented by an infinite resistance connection $R_d = \infty$. Mathematically the number of dead-ends is $N_d = 2N_w$. The number of junction resistors is simply N_j and each will follow some junction resistance distribution $\sigma_j(R_j)$. Finally there are current carrying inner-wire segments whose relative percentages can be derived with the following logic. Consider a network with no inter-wire junctions, the number of wire segments is clearly the number of wires in the network. For every inter-wire junction that is added to the network, two wire segments are formed (one on each wire). Thus the total number of wire segments N_s are

$$N_s = N_w + 2N_j$$

However this includes dead-ends and so the number of current-carrying wire segments is

$$N_{cc} = N_s - N_d = 2N_j - N_w$$

Figure 4.4(a) presents a sketch of a simple NWN and Figure 4.4(b) identifies the different types of resistors. In this network $N_w = 5$ and $N_j = 5$, it then follows that there are $N_d = 10$ dead-ends which are coloured in blue and there are $N_{cc} = 5$ current carrying segments coloured in red.

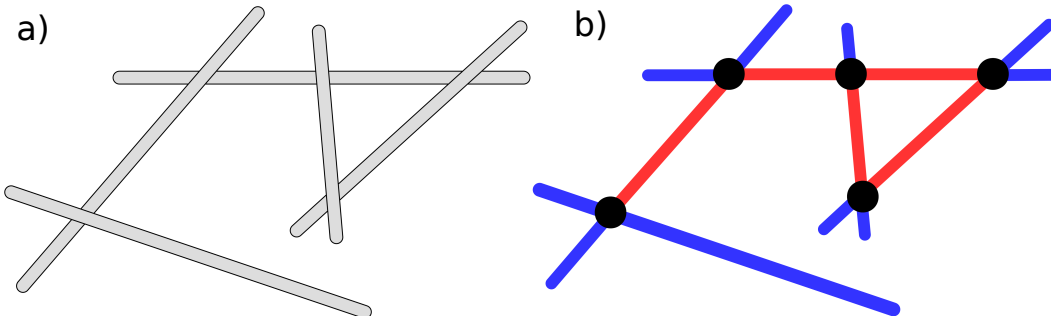


Figure 4.4: A sketch of a NWN depicting the different types of resistors present. In this network there are five wires, $N_w = 5$, and the five junctions, $N_j = 5$, depicted by black circles. There are ten dead-ends, $N_d = 2N_w = 10$, and are depicted by blue segments. There are five current-carrying segments, $N_{cc} = 2N_j - N_w$, shown in red. In total there are $N_t = N_j + N_d + N_{cc} = 20$ resistors in this network.

The total number of conductors N_t is the sum of inter-wire junctions N_j and wire segments

$$N_t = N_j + N_{cc} + N_d = 3N_j + N_w$$

The relative percentages of each type of resistor is thus

$$\begin{aligned} P_j &= \frac{N_j}{3N_j + N_w} \\ P_{cc} &= \frac{2N_j - N_w}{3N_j + N_w} \\ P_d &= \frac{2N_w}{3N_j + N_w} \end{aligned} \quad (4.2.1)$$

where P_j is the percentage of junction resistors, P_{cc} the percentage of current carrying wire segments, and P_d the percentage of dead-ends. These relative populations can easily be translated into expressions in terms of junction and wire densities by dividing both numerator and denominator by the area of the network. In chapter 2 an expression relating the junction density with the wire density in a network was derived as $n_j = \omega L^2 n_w^2$ where $\omega \approx 0.316$. Following this expression the relative percentages in terms of wire densities and their lengths only is

$$\begin{aligned} P_j &= \frac{\omega L^2 n_w}{3\omega L^2 n_w + 1} \\ P_{cc} &= \frac{2\omega L^2 n_w - 1}{3\omega L^2 n_w + 1} \\ P_d &= \frac{2}{3\omega L^2 n_w + 1} \end{aligned} \quad (4.2.2)$$

Equations 4.2.2 allows one to calculate the population of each type of resistor in a NWN knowing only the total number of wires and junctions. This is a more desirable form for the relative percentages of populations as it does not require one to explicitly count the number of junctions in a NNW. The nanowire density and typical length are predefined parameters in typical Monte Carlo simulations and are straightforward to measure in physical NWN samples.

Figure 4.5 presents a visualisation of these relative percentages as a function of wire density for a NWN with nanowires of length 7 μm . Note that as the wire density tends to infinity the percentage of dead-ends tends to zero, while the number of junctions tends to $1/3$ and the number of current carrying segments tends to $2/3$. As mentioned previously each node in MNR has three nearest neighbours and is

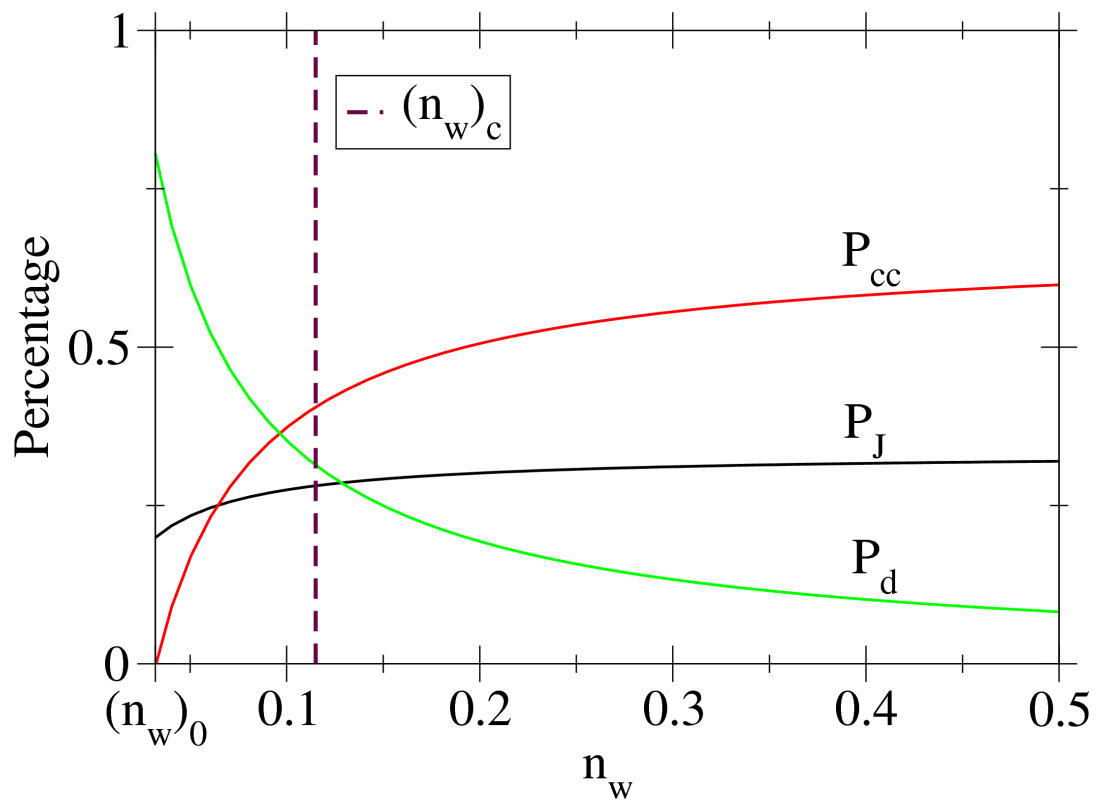


Figure 4.5: A plot of the relative percentages of the different types of resistors in a NWN as a function of wire density for a NWN with wire lengths of $7\mu\text{m}$. The red curve is the percentage of current carrying wire segments P_{cc} , the black curve is the percentage of junctions P_j and the green curve is the percentage of dead ends P_d . The purple dashed line is the percolative critical wire density $(n_w)_c$ at which a percolative path occurs in 50% of randomly generated networks with this density⁴⁸.

connected to a junction resistance and either two current carrying wire segments or one current carrying wire segment and a dead end. As the number of wires tends to infinite the percentage of dead-ends drops to zero and so the percentages tend to the $1/3$ junctions $2/3$ current-carrying segment percentages. On the other extreme a critical wire density of sorts can be identified at which the percentage of current-carrying segments is zero according to the definition of P_{cc} in equation 4.2.2.

$$(n_w)_0 = \frac{1}{2\omega L^2} \quad (4.2.3)$$

For wire lengths of $L = 7\mu\text{m}$ this gives $(n_w)_0 \approx 0.035 \text{ nanowires}/\mu\text{m}^2$. At this value there are only dead-ends and wire junctions which does not result in a conductive network as there are no conducting wire segments through which current can flow. $(n_w)_0$ is the minimum wire density that is considered in Figure 4.5 as below this density $P_{cc} < 0$.

The population of each type of resistor is only one of the components to the full conductance distribution $f(g)$, one also requires the distribution in conductance values of each type of resistor. Recall from chapter 2 that the effective conductance g_m is calculated using the following equation

$$\int \frac{g_m - g}{g + (z/2)g_m} f(g) dg = 0 \quad (4.2.4)$$

Where z is the degree of each node in the lattice. In general the distribution for NWNs to be used in equation (4.2.4) is:

$$f(g) = P_{cc}\sigma_{cc}(g) + P_j\sigma_j(g) + P_d\delta(g) \quad (4.2.5)$$

where $\sigma_{cc}(g)$ is the distribution of inner-wire conductances, $\sigma_j(g)$ is the distribution of junction conductances, and all dead-ends have a conductance $g = 0$ hence its distribution $\delta(g)$ characterised by the Dirac delta. While the populations of each type of resistor has been given in equation 4.2.2 the distributions to be used for the junction and inner-wire resistances have not. The junction resistances in Monte Carlo simulations are usually fixed to some homogeneous value g_j and so $\sigma_j(g) = \delta(g - g_j)$. The conductance of a current carrying inner-wire segment is given by $g_{cc} = \frac{A_c}{\rho\ell}$ where ρ is the resistivity, A_c the cross sectional area, and ℓ the length of the wire segment. The inner-wire conductance distribution will be approximated by the conductance of length that is the average of the length distribution. The

average wire segment length \tilde{l}_s is calculated by dividing the total length of all the wires by the number of wire segments in the network.

$$\tilde{l}_s = \frac{LN_w}{N_s} = \frac{LN_w}{N_w + 2N_j} \quad (4.2.6)$$

where L average length of each wire. It follows then that the characteristic inner-wire conductance is $g_{cc} = A_c/\rho\tilde{l}_s$ making the conductance distribution $\sigma_{cc}(g) = \delta(g - g_{cc})$. Equation 4.2.5 simplifies to

$$f(g) = P_{cc}\delta(g - g_{cc}) + P_j\delta(g - g_j) + P_d\delta(g) \quad (4.2.7)$$

This approximation of the conductance distribution in NWNs can now be easily used to solve for the effective conductance. Solving equation 4.2.4 for a square lattice (degree ($z = 4$)) and with the distribution given in equation 4.2.7 the effective conductance is given by

$$g_m = \frac{g_{cc}(N_j - 3N_w) - g_j(N_j + N_w)}{6N_j + N_w} + \frac{1}{6N_j + N_w} \left(12g_{cc}g_j(N_j - N_w)(3N_j + N_w) + (g_{cc}(N_j - 3N_w) - g_j(N_j + N_w))^2 \right)^{1/2} \quad (4.2.8)$$

Rewriting the number of junctions in terms of the wire density using the relationship $n_j = \omega L^2 n_w^2$ the effective conductance can be written as

$$g_m = \frac{g_{cc}(\omega l^2 n_w - 3) - g_j(1 + \omega l^2 n_w)}{2 + 6\omega l^2 n_w^2} + \frac{1}{2 + 6\omega l^2 n_w} \left(12g_{cc}g_j(\omega l^2 n_w - 1)(1 + 3\omega l^2 n_w) + (3g_{cc} + g_j + \omega(g_j - g_{cc})l^2 n_w)^2 \right)^{1/2} \quad (4.2.9)$$

Recalling the definition of the characteristic inner-wire resistance, equation 4.2.9 is an expression in terms of the wire length, density, diameter, resistivity, and junction resistance only which are all predefined parameters of a NWN. This means simulations are not required to calculate the parameters for the effective conductance.

Revisiting the inter-nodal resistance for a NWN shown in Figure 4.3 the effective resistance calculated using equation 4.2.9 using parameters matching those of the simulated network is $R_{EMT} \approx 6.01\Omega$. Recall that in Figure 4.3 equation 4.1.1 was fit to the simulation data with the resistance R as the only fitting parameter resulting in $R_{fit} \approx 6.09\Omega$. Figure 4.6 presents the data shown in Figure 4.3 alongside the approximation to the lattice Green's function given by equation 4.1.1 with the effective resistance found through regression as the green line, and the effective resistance calculated using equation 4.2.9 in the orange dashed line. The agreement between the R_{fit} and R_{EMT} is remarkably close considering that mapping the NWN onto an Effective Medium square lattice involved several approximations in creating the resistance distributions and indeed the mapping in itself.

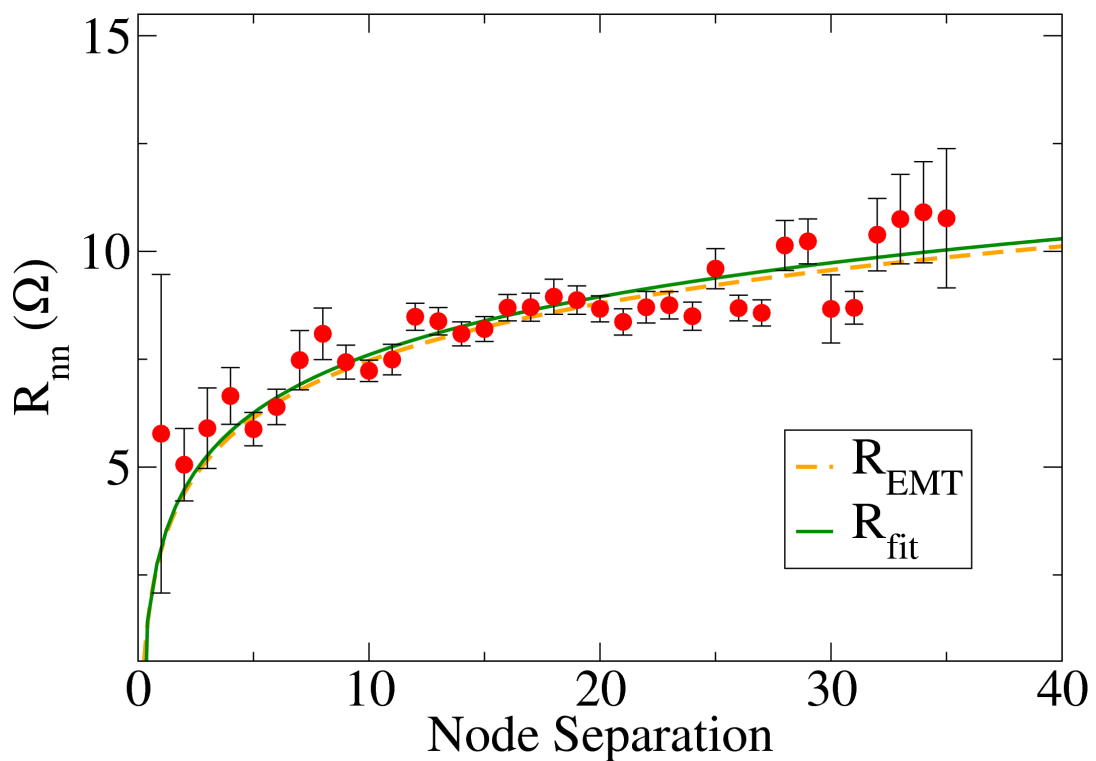


Figure 4.6: Data points correspond to the inter-nodal resistance that was shown in Figure 4.3. The green solid line was obtained by fitting equation 4.1.1 to the data with the resistance R the only fitting parameter which was calculated as $R_{fit} \approx 6.09\Omega$. The Orange dashed line represents equation 4.1.1 with $R = R_{EMT} = 6.01\Omega$ calculated using equation 4.2.9.

4.3 INTER-ELECTRODE RESISTANCE IN A NANOWIRE NETWORK

In the previous section the inter-nodal resistance in a NWN was successfully calculated by mapping its resistive properties onto an effective medium square lattice. As seen in Figure 4.1(a) NWNs are usually fabricated with bounding electrodes on two opposite sides in order to measure the sheet resistance. In this section the mapping between NWNs and the effective medium square lattice is extended to take into account the bounding electrodes. The first step in this is calculating the resistance of a finite homogeneous square lattice that is bounded on either end by an electrode, such as the system sketched in Figure 4.7(b) where the electrodes are represented by two vertical strips of $N_y = 7$ black square nodes separated by $N_x = 13$ resistor edges. Electrodes are at equipotential and so by symmetry each column of nodes are also at equipotential which varies as one moves from left to right. In this scenario no current flows between nodes in the same column due to there being no difference in potential and so the square lattice can be viewed as N_y parallel paths each containing N_x resistors in series. The inter-electrode resistance R_e is

$$R_e = R \frac{N_x}{N_y}$$

Where R is the resistance of each network edge.

Figure 4.7(a) presents a sketch of a NWN where there are 7 nanowire intersections with the electrodes and 13 total resistors (both junction and inner-wire resistors) in the shortest path between the electrodes. The shortest paths between electrodes are determined by applying a path finding algorithm to the graphical representation of the NWN, the same method used in the previous section to calculate the nodal separation. Figure 4.7(b) is a mapping of the NWN in panel (a)

onto a square lattice, the lattice has the same graphical dimensions as the NWN. In order to compare the mapping between a NWN and a square lattice with extended electrode the dependence of R_e on N_x was identified by simulating a large NWN and calculating R_e with electrodes placed at various N_x separations and keeping the number of electrode intersections $N_y = 7$. The relationship between R_e and the calculated nodal separation N_x is plot in Figure 4.7 (c) for the NWN and its effective medium square network with a matching N_y and N_x . A clear linear relationship exists for the effective medium square lattice which is represented by the green triangles whereas R_e fluctuates around the linear trend. The effective medium square lattice approximates the simulated NWN very well. In this example the quantities N_x and N_y were explicitly counted for a NWN in simulations which is a tedious process and quickly becomes too difficult for large dense NWNs, and so analytical approximations for both are needed.

The number of parallel paths in the effective medium square lattice can be calculated using a variant of the geometric probability method used in the famous “Buffon’s Needle” problem⁹⁷. Consider an input electrode with N_y wire intersections, each intersection opens the possibility of a parallel path between the electrodes. In this approximation we will take the number of electrode intersections as the number of parallel paths between electrodes. Consider a wire of length L . If the center point of the wire is a distance $x < \frac{L}{2}$ from an electrode, the two will intersect if the angle θ is in the range

$$\theta \leq \cos^{-1} \left(\frac{2x}{L} \right) \quad (4.3.1)$$

where θ is the angle the wire makes with the horizontal. A wire at a distance x intersects the electrode with a probability $\frac{2}{\pi}\theta$. In order to obtain a probability that a wire intersects the y axis once its center is $x \leq \frac{L}{2}$ we perform an integration over x .

$$\frac{2}{\pi} \int_0^1 dx \cos^{-1}(\theta) = \frac{2}{\pi}. \quad (4.3.2)$$

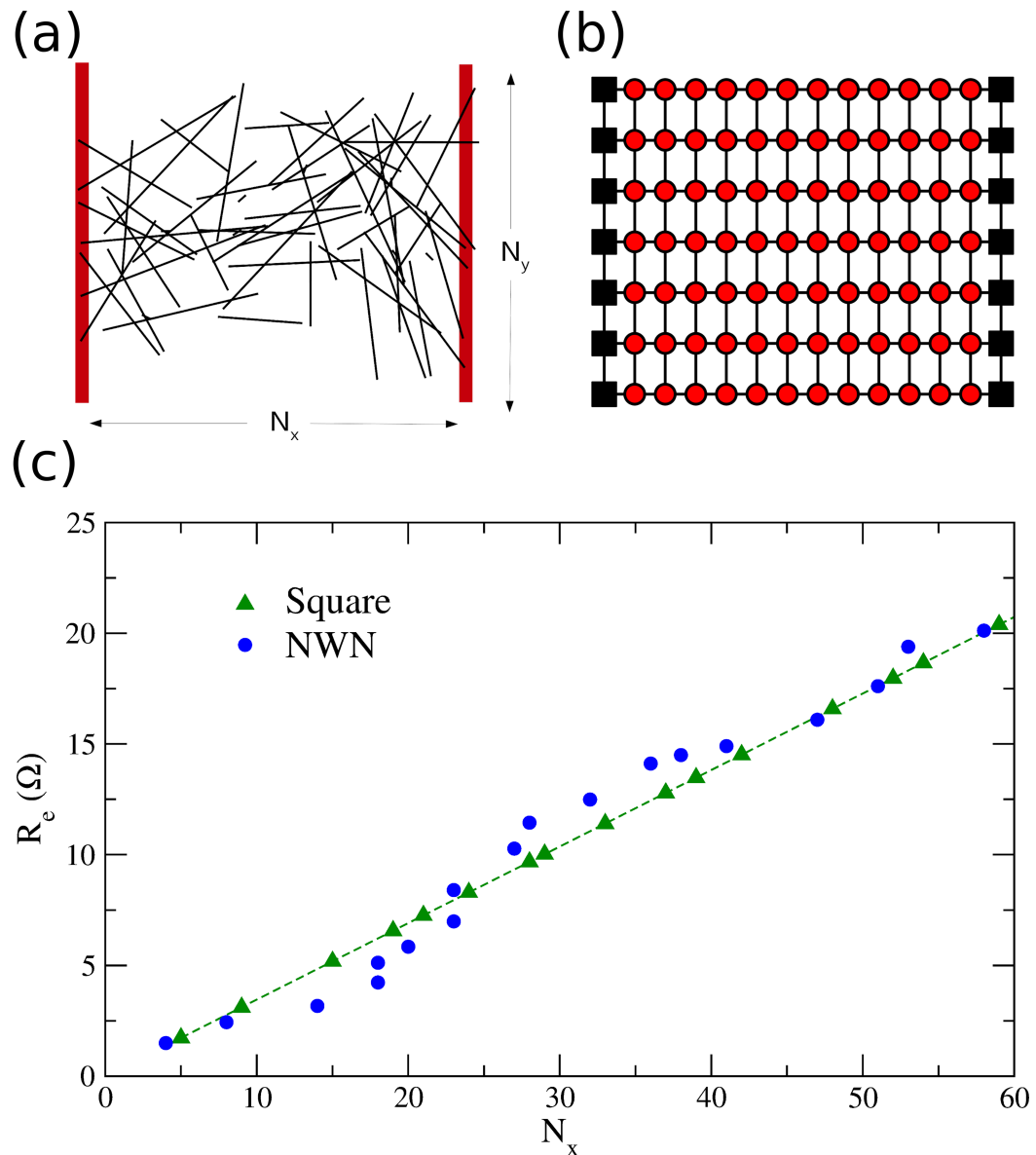


Figure 4.7: (a) A simulated NWN with two separate finite-sized electrodes represented by vertical red lines. $N_y = 7$ wires cross the electrodes. (b) Square lattice with finite-sized electrodes (represented by red dots). The number of black squares on either side corresponds to the value of $N_y = 7$ electrode nodes obtained from panel (a). N_x represents the characteristic number of junctions and wire segments needed to form a path between the electrodes; (c) Equivalent resistance as a function of N_x . Circular dots are the calculated results for the realistic network whereas triangular dots correspond to the results of the corresponding effective medium square lattice.

We now consider how many wires lie in the range that they could potentially intersect the electrode. If wires are distributed homogeneously with a density of n_w

and over a vertical width range of W , the relevant area is $WL/2$ which contains $WLn_w/2$ wires. Combining this with the value of p_e , the expected total number (N_y) of intersections can be written as

$$N_y = \frac{LWn_w}{\pi}. \quad (4.3.3)$$

Figure 4.8 compares equation 4.3.3 with computer simulations in which N_y was counted for systems with various wire densities (Figure 4.8(a)), lengths (Figure 4.8(b)), and NWN widths (Figure 4.8(c)). In each case the analytical expression shows excellent agreement with simulations but note that equation 4.3.3 overestimates N_y in each case, particularly for high wire lengths. These discrepancies are due to boundary effects, at the top and bottom parts of the NWN the constraint on wire positions increases making electrode intersections in these areas less likely. Thus the relative discrepancy between theory and simulation could be more pronounced for larger parameter values and smaller NWNs.

The nodal separation between electrodes is more difficult to approximate. A useful interpretation is to view a NWN as a small-world network on short length scales and a regular network for larger length scales. A Watts-Strogatz (WS) network is an example of a small-world network⁹⁸. A WS network is created by taking a regular lattice network where each node has z nearest neighbours. A percentage p of links are removed and are then used to connect random pairs of nodes anywhere in the network. We assume that NWNs of size $L \times L$ behave as small-world networks, where L is the typical length of a Nanowire. The rationale here is that a current carrying segment can act as a pathway for current flow and allow it to move a large distance at a time whereas a junction resistor does not facilitate large distance movement, thus the wire segments act as the random connections in a WS model but only over distances less than the length of a wire.

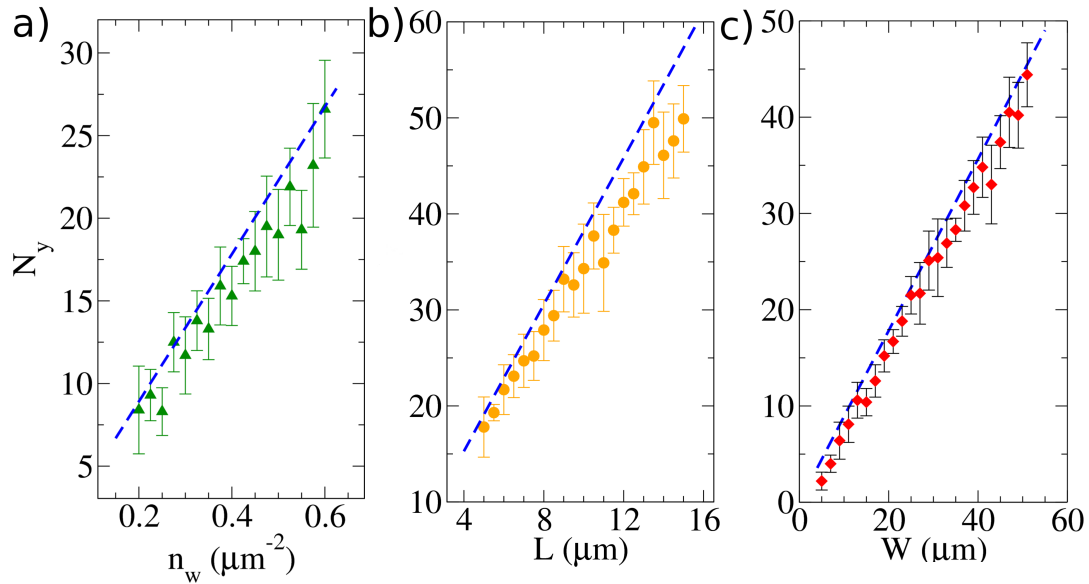


Figure 4.8: The dependence of N_y on wire densities in a NWN of size $20\mu\text{m} \times 20\mu\text{m}$, and wire lengths $7\mu\text{m}$. N_y is counted for each wire density and the average N_y of 20 samples for each wire density is plot with corresponding 95% confidence intervals. Equation 4.3.3 is plot in black alongside the simulation results displaying excellent agreements between the two. (b) The dependence of N_y on the width (W) of the NWN where the NWN is of size $W\mu\text{m} \times 20\mu\text{m}$, and with the same wire density and length as (a). The data points (circles) are the average of 20 measurements for a given width and the 95% CI are plot alongside. (c) The dependence of N_y on wire length in a NWN of size $20\mu\text{m} \times 20\mu\text{m}$, and wire density $0.4\mu\text{m}^{-2}$. Theoretical values are plot alongside and represented by the black line.

Braunstein et al⁹⁹ showed that when weak disorder is introduced to the weight values of links the optimal path q_{opt} that minimises the total weight of the path connecting two nodes scales as:

$$q_{\text{opt}} \propto \frac{1}{pz^2} \log(Npz) \quad (4.3.4)$$

here N is the number of nodes in the network. In the MNR model the number of nodes in an area $L \times L$ in terms of wire density is $2n_jL^2$ or $2\omega L^4 n_w^2$. Each node is connected to one junction resistor, a wire segment and either another wire segment or a dead end making the degree of each node $z = 3$. p is the percentage of current carrying intra-wire segments in the network as they can connect two nodes that

have a large separation. Therefore $p = P_{cc} = \frac{2N_j - N_w}{3N_j + N_w}$ from equation 4.2.2. Subbing this into equation 4.3.4, q_{opt} scales as

$$q_{opt} \propto \frac{1}{P_{cc}} \log(6\omega L^4 n_w^2 P_{cc}) \quad (4.3.5)$$

Consider a network of size $W \times W$, $W \gg L$ and node A that lies on the electrode of the NWN. The optimal path between node A and node B that are separated by a distance L is q_{opt} defined above. Similarly the distance between node B and another node C that are again separated by a distance L is q_{opt} and so two electrodes separated by a distance W is $\frac{W}{L} q_{opt}$. Using equation 4.3.5 the number of resistors in the shortest path connecting the two electrodes can be written as

$$N_x = \frac{W}{L} \frac{\kappa}{P_i} \log(6\omega L^4 n_w^2 P_i) \quad (4.3.6)$$

where κ is a constant of proportionality. In Figure 4.9(a) the dependence of N_x on the electrode separation is shown for NWNs of wire lengths $7\mu\text{m}$ and density 0.5 nanowires/ μm^2 . The data points represent the average result of different randomly generated NWNs with a given electrode separation and the 95% confidence interval is also shown. Equation 4.3.6 is plotted alongside the experimental data and the constant of proportionality was found to be $\kappa \approx 1.1$ from regression analysis and agrees excellently with the results of simulations. In Figure 4.9(b) the dependence of N_x on the wire density is shown for NWNs of wire lengths $7\mu\text{m}$ and a NWN size of $20 \mu\text{m} \times 20 \mu\text{m}$. The results of simulations are represented by the data points and equation 4.3.6 by the blue curve with $\kappa \approx 1.1$. The theoretical curve gives a reasonable approximation to the nodal separation between electrodes however it does underestimate the path length at low densities. Equation 4.3.6 is a useful approximation for Nodal separations between electrodes however it is not ideal as it contains a constant of proportionality κ and does not match simulations at low densities.

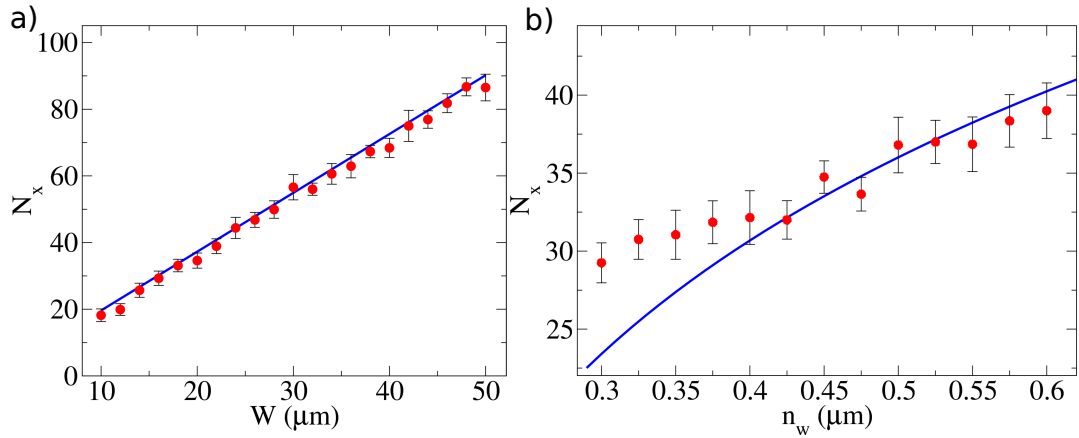


Figure 4.9: (a) The Nodal distance between electrodes is plot versus the separation between them. The results are for networks with wire lengths of $7\mu\text{m}$ and wire densities of $0.5\mu\text{m}^{-2}$. 10 simulations of random NWNs are performed for each data point. (b) The Nodal distance between electrodes is plot versus wire density for a sample of size $20\mu\text{m} \times 20\mu\text{m}$ and wire lengths of $7\mu\text{m}$. 20 simulations of random NWNs for a given density are performed for each data point.

Combining the many separate parts derived in this chapter the formula to describe the inter-electrode of a NWN by means of an effective square lattice of electrode height H , electrode separation W , and effective conductance g_m is

$$\begin{aligned}
 R_e &= R_m \frac{N_x}{N_y} = \frac{1}{g_m} \frac{N_x}{N_y} \\
 N_y &= \frac{L n_w}{\pi} \\
 N_x &= \frac{W}{L} \frac{\kappa}{P_i} \log(6\omega L^4 n_w^2 P_i) \\
 P_{cc} &= \frac{2\omega L^2 n_w^2 - n_w}{3\omega L^2 n_w^2 + n_w} \\
 \tilde{l}_s &= \frac{L n_w}{2\omega L^2 n_w^2 + n_w} \\
 g_{cc} &= \frac{\rho \tilde{l}_s}{A_c} \\
 g_m &= \frac{g_{cc}(\omega L^2 n_w - 3) - g_j(1 + \omega L^2 n_w)}{2 + 6\omega L^2 n_w^2} + \frac{1}{2 + 6\omega L^2 n_w} \left(12g_{cc}g_j(\omega L^2 n_w - 1)(1 + 3\omega L^2 n_w) + \right. \\
 &\quad \left. + (3g_{cc} + g_j + \omega(g_j - g_{cc})L^2 n_w)^2 \right)^{\frac{1}{2}} \tag{4.3.7}
 \end{aligned}$$

Here the only parameters needed to calculate a sheet resistance is the wire density n_w , wire length L , NWN height H , electrode separation W , the junction conductance g_j , and the wire resistivity and cross sectional area ρ , A. While at face value this expression seems to have many complex constituents, they all are calculated from the fundamental parameters of the NWN. These expressions allow for the approximation of several measurable quantities in a NWN all without the need of additional Monte Carlo simulations or image processing techniques.

4.4 APPLICATION OF THE EFFECTIVE SQUARE LATTICE

In this section the effective square lattice will be used to estimate the sheet resistance of a network using known nanowire properties and compared with Monte Carlo simulations. Equations 4.3.7 are used to calculate the sheet resistance of the effective lattice, and while they are relatively complicated they can easily be written in a programming language and calculations performed extremely quickly compared to the Monte Carlo simulations. This method allows for a quick examination on the necessary nanowire properties required for a desired sheet resistance. Furthermore network parameters such as the ultimate conductivity of a network can be estimated very quickly as opposed to the lengthy digitisation and MNR simulation routine presented in the previous chapter.

In Figure 4.10 the effective square lattice summarised in equation 4.3.7 is plotted against average values of sheet resistance for various wire densities. Green data points are the average conductance of 20 simulations with 95% confidence intervals of Monte Carlo simulations of NWNs of size $20 \mu\text{m} \times 20 \mu\text{m}$, wires of length $7 \mu\text{m}$ with other parameters corresponding to those characteristic of Ag/PVP nanowires used throughout this thesis⁷⁹. The blue curve is a visualisation of equation 4.3.7 and agrees closely with simulated data, lying within the confidence interval for

each data point. The inset graph presents equation 4.3.7 in blue with horizontal axis rescaled to $x = n_w - (n_w)_c$ alongside a red curve proportional to $x^{-1.44}$. Recall from the discussion of percolation theory in chapter 3 that simulated resistances of Ag/PVP nanowire networks scales with the quantity x as $x^{-1.44}$. Here the sheet resistance as calculated by equation 4.3.7 converges onto this scaling at an approximate density 0.25 nanowires/ μm^2 , thus agreeing with the appropriate scaling according to percolation theory. Figure 4.10 shows that the effective square lattice mapping is particularly accurate at capturing the networks scaling with nanowire density.

The resistive parameters of the NWN; junction resistance, wire resistivity, and cross sectional areas, only affect the calculation of the effective conductance g_m as they do not alter the connectivity profile, and their impact is shown in Figure 4.11. Panel (a) presents the effect of changing wire resistivity on the sheet resistance for Monte Carlo simulations as red data points and for the expression outlined in equation 4.3.7 as the blue curve. The approximation agrees well with the Monte Carlo in this case. Figure 4.11(b) shows the dependence on the junction resistance for Monte Carlo simulations as red data points and the effective square lattice as the solid blue curve. Here the approximation gives a good estimate to the sheet resistance of the networks. Recall from chapter 3 that the dependence of the sheet resistance on the resistivity and junction resistance is linear for both parameters when applied to a particular network geometry. Here it is the average of ten simulations of a given R_j or ρ that is being compared with the effective square lattice. In Figure 4.11, equation 4.3.7 provides a slightly curved relationship between the sheet resistance and R_j and ρ but it does provide an excellent estimate to sheet resistances in both cases. As mentioned in the derivation of the effective medium theory, it is most accurate when the current flow distribution is homogeneous across the NWN. It may be that the increasing junction resistance results in a more localised current flow making the effective medium theory less applicable. If current flow does become inhomogeneous then the approximation of N_y parallel paths also becomes less applicable,

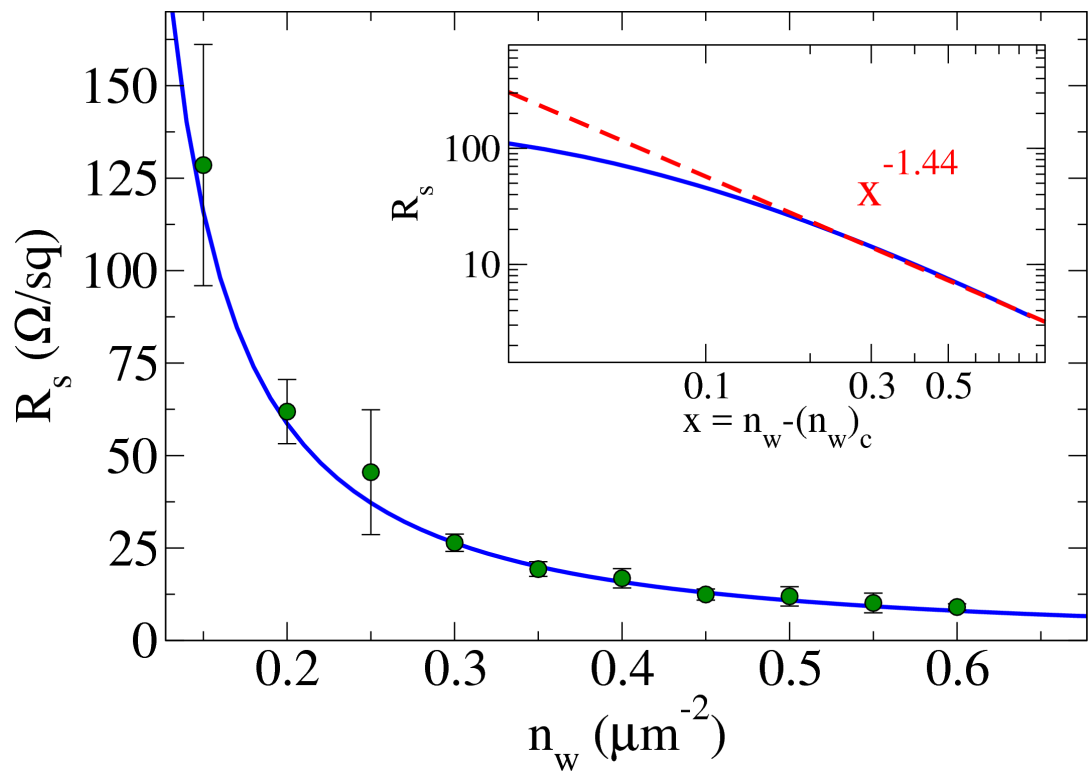


Figure 4.10: The dependence of sheet resistance on wire densities. Data points represent the average sheet resistance for 20 simulations for each given wire density performed in a NWN of size $20\mu\text{m} \times 20\mu\text{m}$ with wires of length $7\mu\text{m}$. The junction resistance values and resistivities are those characteristic for Ag/PVP wires⁷⁹. The 95% confidence intervals for each n_w are also plotted. The theoretical sheet resistance calculated using equation 4.3.7 is represented by the blue curve. The inset log-log figure presents the theoretical curve with alongside a power law proportional to $(n_w - (n_w)_c)^{-1.44}$ which converge at higher wire densities. The value of the scaling exponent of -1.44 was determined in chapter 3 when examining the percolative scaling of a NWN's sheet resistance with respect to wire density.

which would effect the approximation of the sheet resistance. Thus the effective square lattice is most accurate for networks whose junction resistances and wire segment resistance are comparable to one another, and will become less accurate if junction dominant or intra-wire dominant resistive networks.²

Further to Monte Carlo simulations, the effective square lattice mapping can be used to approximate the sheet resistance of experimental samples. Table A.1 in Appendix A lists the sheet resistance and other properties of thirty experimental

² may add this paragraph and Figure 4.11 to an Appendix or remove it entirely

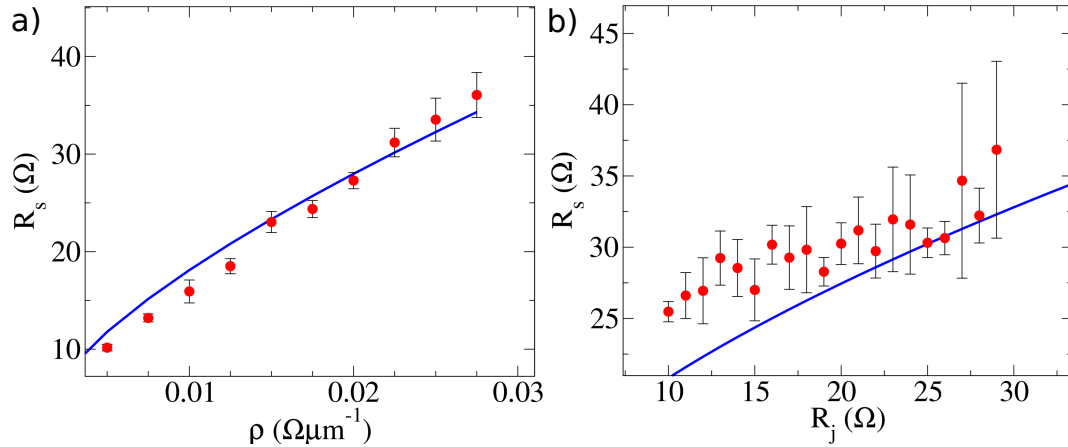


Figure 4.11: (a) The effect of changing wire resistivity on the sheet resistance. The data points correspond to the average and 95% sheet resistance calculated for a set of 10 simulations for a given resistivity and the curve corresponding to the theoretical expression in equation 4.3.7. (b) The sheet resistance Vs the junction resistance, again data points are from Monte Carlo simulations for 10 samples and the curve corresponds to Equation 4.3.7. Both (a) and (b) use networks of size $30\mu\text{m} \times 30\mu\text{m}$, wire density $0.4 \text{ Nw}/\mu\text{m}^2$ and, wire length $7\mu\text{m}$. Note: may add this plot and associated discussion to an appendix

Ag/PVP NWN samples that were discussed at length in chapter 3. Figure 4.12 presents the experimental sheet resistance for each sample versus their wire density as red data points. The solid blue curve is the sheet resistance calculated with the effective square lattice method having the nanowire parameters set to those typical of Ag/PVP nanowires, in particular the junction resistance was set $R_j = 11 \Omega$. The effective square lattice mapping provides an excellent estimate to the sheet resistance of the experimental samples, however it does underestimate the majority of sheet resistances. Recall from chapter 3 that the characteristic junction resistances determined through MNR simulations was much higher than 11Ω .

In chapter 3 a distribution of junction resistances was shown in Figure 3.8, in which there exists a small population of high resistance junctions. The electroforming process that was used to minimise junction resistances for the experimental samples involves increasing current flow through the network slowly to a point where the sheet resistance is in a stable and low resistance state. As shall be demon-

strated in the next two chapters this leads to the emergence of many parallel low resistance pathways between the electrodes which can lead to some isolated junctions not being electroformed as others⁹². As stated previously the effective lattice requires a relatively homogeneous resistor distribution for accuracy but it can be used here to estimate the population of outliers in samples. By choosing a representative high resistance state of $R_j^h = 200 \Omega$ that is a percentage χ of junction resistors, and fixing the remaining $1 - \chi$ junction resistors at $R_j = 11 \Omega$ the effective resistance is calculated as the weighted average of the two. Then by tuning χ an estimate for junction outliers present is achieved. In Figure 4.12 the green dashed line corresponds to a $\chi = 10\%$ percentage of high resistance junctions and provides a much better agreement between the effective square lattice and experimental samples.

Further to approximating the sheet resistance the effective square lattice can be used to quickly determine the optimization capacity coefficient γ which was defined in chapter 3 as

$$\gamma = 1 - \frac{R_0}{R_s^{\text{EXP}}} \quad (4.4.1)$$

where R_s^{EXP} is the experimental sheet resistance and R_0 is the contribution to the sheet resistance from the inner-wire resistances. Recall that values of γ close to 1 represent networks whose conductivities can be considerably improved since their sheet resistances are far from the optimal value R_0 , the sheet resistance of a NWN if it were to have perfect junction resistors ($R_j = 0$). For relatively small values of γ , on the other hand, the network is close to its optimum conductivity and is unlikely that it can be further optimized. In chapter 3, R_0 was calculated numerically for each sample using the MNR model with perfect junction conductance using the digitisation method to capture the connectivity profile of a NWN. The effective square lattice can be used to easily determine the sheet resistance when $R_j = 0$ and is shown by the black dotted line in Figure 4.12. Using these theoretical values for R_0 , γ is calculated for each experimental sample and is plotted against wire density

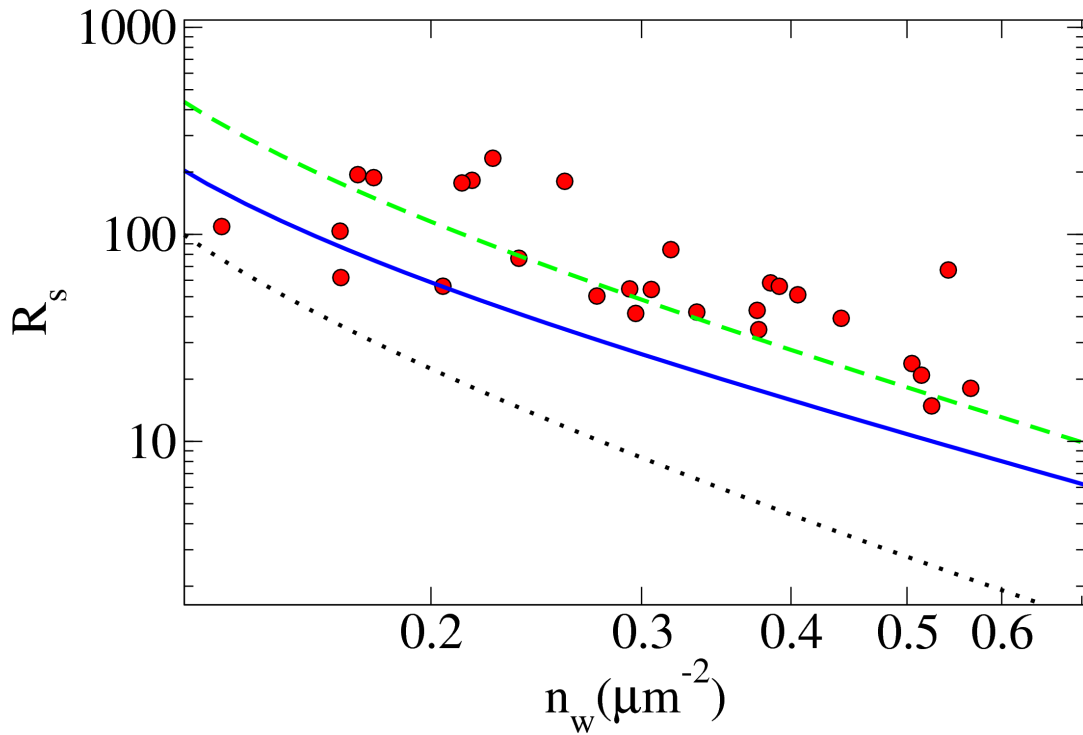


Figure 4.12: The Sheet resistance R_s versus the wire density measured for thirty experimental Ag/PVP NWNs listed in Table A.1 are plotted as red data points. The blue curve is the sheet resistance versus wire density calculated using the effective square lattice summarised in equation 4.3.7 with a junction resistance of 11Ω and other parameters typical to Ag/PVP nanowires⁷⁹. The green dashed curve includes the effect of outlier junction resistances and corresponds to an effective square lattice with 10% of the junctions at 200Ω and the remaining junctions at 11Ω . The black dotted line is the ultimate conductivity of a NWN for a given wire density as calculated by the effective square lattice where all junctions have a perfect resistance $R_j = 0 \Omega$.

for each sample in Figure 4.13 and is in close agreement to the results of numerical simulations presented in Figure 3.9.

It is in the application of the effective square lattice mapping for experimental results that its usefulness is properly illustrated. In Chapter 3 the different node-voltage mappings, JDA and MNR, were combined with digitised SEM images of NWNS in order to estimate quantities such as the characteristic junction resistance and the optimization capacity coefficient. These calculations took a large deal of effort and for the denser networks a great deal of computational resources. The effective square lattice on the other hand is an extremely fast method to estimate

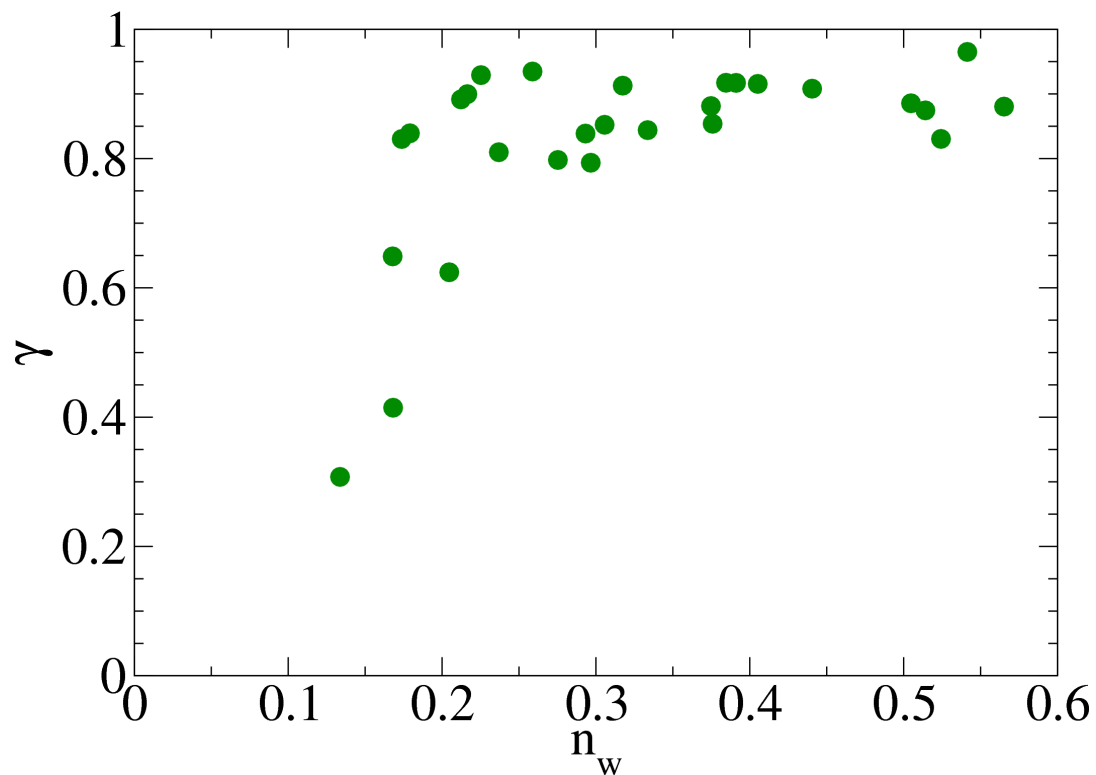


Figure 4.13: The optimizatitition capacity coefficient for the thirty experimental samples plot as green data points in Figure 4.12 calculating the ultimate conductiv- ity R_0 using the effective medium square lattice.

different properties of a NWN and a welcome tool for understanding the resistive properties of NWNs.

4.5 CONCLUSION

In summary, here a simple method that establishes the correspondence between the sheet resistance of a heavily disordered NWN with that of an ordered network was outlined. To do so the current flow between junctions in a NWN was shown to scale with their separation logarithmically in the same manner as a regular square lattice in section 4.1. Expressions for the relative percentages of types of resistors in a NWN were derived, the types of resistors being inter-wire junctions, current-carrying wire segments and dead-ends in section 4.2. These expressions can be

used to determine a quantitative critical wire density at which a percolating path between electrodes is impossible, which is much less than the one suggested by percolation theory. In the same section the expressions for relative resistor percentages were used to create an effective medium, one which maps the resistive properties of a random NWN onto a regular square lattice. This mapping was shown to approximate logarithmic scaling of the resistance Vs nodal separation between pairs of junction intersections in a random NWN mentioned above.

In section 4.3 The sheet resistance of a finite square lattice where two opposite sides are bounded by electrodes of length N_y nodes and separated by N_x resistors with resistance R were shown to operate as N_y parallel paths of resistance RN_x . To apply this expression and the effective square lattice mapping to a NWN expressions to approximate N_x and N_y in a NWN were derived. The expression for N_y was found to agree closely with Monte Carlo simulations for various wire densities and wire lengths. The expression for N_x estimated those recorded in Monte Carlo simulations well. After combining the effective square lattice with the expressions for N_x and N_y a closed form approximation for the sheet resistance of a NWN in terms of its underlying geometrical and electrical properties was obtained and is summarised at the end of section 4.3. The approximation was shown to scale closely with Monte Carlo simulations for the fundamental parameters of a NWN in section 4.4. Finally the approximation was applied to thirty experimental samples and used to estimate the optimization coefficient of each network.

5

MEMRISTIVE PROPERTIES OF NANOWIRE NETWORKS

Until now the conductive properties of a NWN has focused on static nanowire junctions that have been annealed in some manner into a low resistance state. The surface layer in individual nanowires - a polymer, native oxide or some other surfactant - are a necessity to stabilise the NWNs during synthesis. Their presence act as an insulating barrier between the highly conductive metallic cores of the nanowires which has traditionally been seen as an undesirable feature in NWNs. Many of the applications of NWNs as transparent conductors require minimal junction resistance in order to increase their sheet conductance while maintaining their high optical transparency. In fact the preceding two chapters had a large focus on understanding the effect of junction resistance on annealed NWNs and their upper-limit sheet conductance where the inter-wire junctions are perfectly annealed. The potential exploitation of these barriers have thus gone largely unexplored.

A popular annealing method for NWNs is electrical stressing. An applied current is gradually increased from small current ranges until such a level where the resistance of the NWN as a whole reaches a low-resistance state, but not so high as to cause wire failures due to melting from Joule heating^{100,101}. This gradual increase in NWN conductivity is akin to a class of materials known as Memristors (Memory resistors) that up until recently were completely theoretical. Memristors were first hypothesised in 1971 by Chua and their defining behaviour is a non-constant, reversible resistance that is mediated by some tunable internal state variable⁵¹. Since the first experimental realisation of a memristor in 2008⁷ many

examples of memristors have been demonstrated, one such device is a planar Metal-Insulator-Metal (MIM) tri-layer. The internal state variable corresponds to some physical phenomenon that can be controlled via some external means, for example many memristors are mediated by an ion-doped layer or a conductive filament, the size of which is controlled by current flow to cause various resistance states^{62? ?}. The MIM architecture that is common in memristors are found in un-annealed nanowire junctions, the metals being the cores of the NWNs and the two surface layers acting as the insulating barrier. This means that a NWN contains many highly connected MIM junctions and offer a rich new area of potential applications as memristive and neuromorphic (brain-like computing) devices.

To date there has been numerous attempts to mimic biological computation through simulation on traditional Von Neumann computer architectures⁷¹. However this approach is computationally expensive and thus energy intensive. Another approach to achieve biological computation is through the use of neuromorphic computing architectures^{55,72}. These are decentralised networks of memristor or analogue synapses. While these architectures are much more energy efficient, the fabrication of such devices can be quite difficult, often requiring exact engineering of individual memristor components and connections. A high level of component homogeneity and regularity in neuromorphic networks may not be required as the variability, stochasticity and component reliability which are becoming increasingly difficult to overcome in traditional computing technologies do not pose as big a problem to biological computing systems⁷³. Indeed the variability of individual synapses and the complexity of the global synapse network are exploited to perform robust and reliable computations, all while using a fraction of the power that a Von Neumann computer would need for similar performance. The spacial stochasticity of the NWN coupled with the memristive properties of inter-wire junctions results in a random memristor network. The random connectivity may actually be beneficial for memory storage and neuromorphic computing as a highly

connected NWN has no hierarchical structure and thus should have a high fault tolerance.

The aim of this chapter is to introduce a memristive model for nanowire junctions and report results of a computational routine that simulates the properties of a NWN. The layout of this chapter is as follows: Experimental evidence for a memristive response of individual NW junctions and global memristive response of a NWN is presented in section 5.1. An empirical model for individual junctions is introduced in this section. In section 5.2 a computational routine to simulate a large network of memristive junctions is introduced and the memristive responses of a network to increasing current flow are presented. The conductance of both the junction and nanowire network are shown to scale as a power law with increasing current levels through the NWN and junctions in section 5.2. The exponent of the networks power law is shown to be the same as the individual junctions of which it comprises showing a self-similarity between the individual and the collective. The activation patterns of nanowire networks is shown to vary according to certain measurable parameters of the memristive junction model. In section 5.3 a mapping technique is presented that allows for the visualisation of current flow through a network at any stage in its junction evolution and shows that for certain nanowire parameters the current flows through a single pathway between electrodes in a winner-takes-all manner. The existence of localised current flows has potential application in neuromorphic computing and a method to achieve independent and associative conductive states in a NWN is presented in section 5.4. Finally a chapter summary is presented in section 5.5

5.1 MODELLING THE MEMRISTIVE RESPONSE OF A NANOWIRE JUNCTION

Figure 5.1(a) presents experimental measurements of the conductance of individual Ag/PVP nanowire junctions for increasing current compliance as triangular data points to the left of the plot, along with the conductance of an Ag/PVP NWN to the right as circular data points⁷. Here both the individual junctions and the NWN clearly respond in a memristive manner to increasing current compliance, their conductivity increases in a power law manner. The NWN scales with a power law over three decades of current compliance signified by the red line through the data points. Remarkably, the fitted power law to the NWN has the same exponent as the power laws fitted to the individual nanowire junctions, meaning their respective conductivities (Γ_{nt}/Γ_j) scale in a self-similar manner. The scaling of an individual junction is described with the power law

$$\Gamma_j = A_j I^{\alpha_j} \quad (5.1.1)$$

where the values of A_j and α_j are material dependent and determine the memristive response of the material. While the memristive scaling presented in Figure 5.1(a) is particular to Ag/PVP nanowires the self-similar scaling between junctions and networks was seen for a range of nanowire materials: Ni/NiO, core-shell Ag/TiO₂ and Cu/CuO⁷.

Another intriguing phenomenon is observed in the NWN's conductance curve where it no longer scales as a power law and reaches a plateau. Figure 5.1(b) is a magnified view of this region where the fine detail of this region can be seen. Three distinct plateaus in the networks conductivity can be seen, each represented by the horizontal Orange-brown lines. The conductivity of the network has been normalised by the quantum of conductance ($\Gamma_0 = 2e^2/h$), the conductance of a sin-

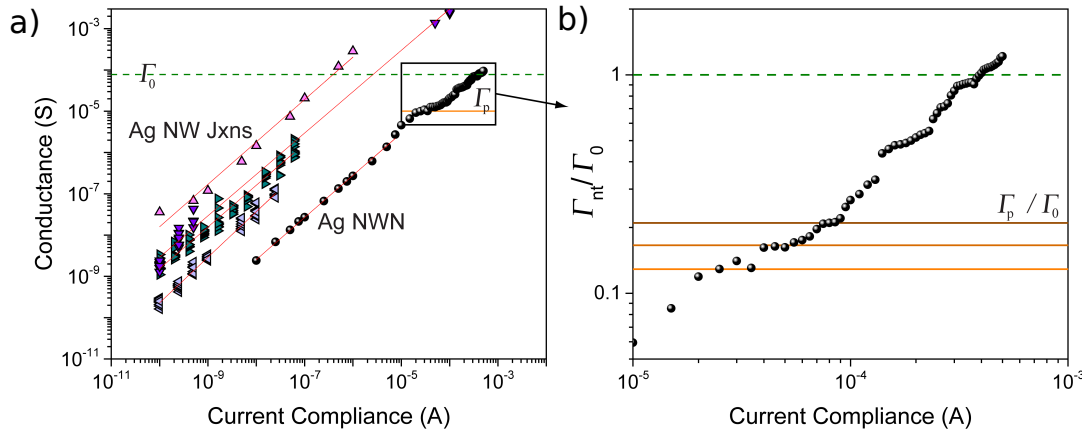


Figure 5.1: (a) Experimental measurements of the conductance of individual Ag/PVP nanowire junctions (triangles) and an Ag/PVP NWN with increasing current compliance levels. Both system display a power law scaling of the conductance, in the case of the NWN this holds until a point at which the conductance reaches a plateau. (b) A magnified view of the memristive response of the NWN in (a) in the vicinity of the plateau in conductivity where the conductance of the network Γ_{nt} has been normalised by the quantum of conductance Γ_0 . Here several smaller plateaus are observed with a conductance Γ_p that are fractions of the (Γ_0).

gle channel that can transport a single spin degenerate pair of electrons, where e is the charge of an electron and \hbar is Planck's constant. The plateaus have an approximate normalised conductance of: $\Gamma_{nt}/\Gamma_0 \approx 1/8$ (bottom), $\Gamma_{nt}/\Gamma_0 \approx 1/6$ (middle), and $\Gamma_{nt}/\Gamma_0 \approx 1/5$ (top). Conductance plateaus were not seen for all of the examined NWN materials mentioned above meaning that specific material properties are required to observe them. In this section a memristive model for individual nanowire junctions is introduced and used in the next section in a computational model of a memristive NWN to explain the self-similar scaling between junctions and NWNs, and to understand the cause of plateaus in NWN conductivity.

Nanowire junctions are described using the scaling law presented in equation 5.1.1. The memristive response of a NWN is then determined through the collective response of the connected nanowire junctions. The set of parameters $[A_j, \alpha_j]$ determine the response of each nanowire junction and as mentioned above are obtained from experimental measurement. We assume that the resistance of the

junctions are bounded by an initial high resistance state (HRS), or the off state, where $R_{\text{off}} = 10^4 \text{k}\Omega$ was chosen as a suitably high value. The low resistance state (LRS) was assumed to correspond to the quantum of conductance $R_{\text{on}} = 12.9 \text{ k}\Omega$ (equivalent to $1/\Gamma_0$). In planar metal-insulator-metal devices the physical process responsible for decreasing resistance, often referred to as the state variable, is the formation of a conductive filament from electromobile atoms or ions that originate in the electrodes⁶⁷. The growth of the conductive filament is regulated by distinct mechanisms including thermochemical, electrochemical metallization, and valence change^{57,63–66}. Where a conductive filament mediates the resistance of the junction, one can assume that once it spans the entire insulating barrier between metallic cores that the conduction is through a single channel. A single conducting channel is a quantum of conductance and so approximates the conductance of a fully formed filament in our model. Thus, the empirical Power law plus cut-off (PL+C) will refer to the junctions whose conductance can vary with equation 5.1.1 but only in the range $[\Gamma_{\text{off}}, \Gamma_0]$.

Figure 5.2 presents the scaling of the conductance of a single junction with varying values of A_j and α_j . The effect of altering the prefactor A_j on a junctions conductance modelled with the PL+C is plot in Figure 5.2(a) where the scaling exponent is set $\alpha_j = 1$. Several effects of changing A_j are seen in this plot, most notably increasing values shift the conductance curve to the left meaning that the junction begins to evolve at lower current levels but also reaches its ultimate conductivity quicker. The current (I_{th}) at which a junction reaches its ultimate conductivity Γ_0 is calculated as

$$\Gamma_0 = A_j(I_{\text{th}})^{\alpha_j} \rightarrow I_{\text{th}} = \left(\frac{\Gamma_0}{A_j}\right)^{\frac{1}{\alpha_j}} \quad (5.1.2)$$

The inverse relationship between I_{th} and A_j is visualised as the purple curve corresponding to the largest value of A_j reaching Γ_0 first. Similarly the current level where the memristive increase in junction conductance begins (I_b) is calculated as

$$I_b = \left(\frac{\Gamma_{off}}{A_j} \right)^{\frac{1}{\alpha_j}} \quad (5.1.3)$$

Here the inverse relationship between A_j is seen as curve with $A_j = 0.5$ begins to increase in conductivity first.

The effect of different scaling exponents on the evolution of the junctions conductance is best understood by considering the derivative of equation 5.1.1, or the strengthening rate v_j

$$v_j = \frac{d\Gamma_j}{dI} = A_j \alpha_j I^{\alpha_j - 1} \quad (5.1.4)$$

According to equation 5.1.4 there are three distinct regimes of NWN scaling exponents. For a sub-linear exponent $\alpha_j < 1$, v_j decreases with increasing current levels meaning that further increasing the conductance becomes more difficult. For supra-linear exponents $\alpha_j > 1$, v_j increases with current levels meaning the strengthening of the junctions becomes easier with increasing conductance. Finally the linear exponent case $\alpha_j = 1$ has a constant strengthening rate. Each of these exponents give rise to unique conductance curves and are presented in Figure 5.2(b) where the prefactor is set $A_j = 0.1$. As both axis are in log-scale, the difference in junction conductance scalings from difference power law exponents are clear. The change in critical current flow I_b is also evident as the smaller exponent requires less current to begin conductance improvement.

Drawing an analogy with the ion-drift model first proposed by Strukov et al⁷ A_j and α_j can be related to the mobility of the diffusing charge-carriers in the junction and to the nonlinear effects caused by the strong electric fields present in the dielectric layer⁷ respectively. In their model, Strukov et al hypothesised that the memristance was modulated by an intefacial boundary between an undoped

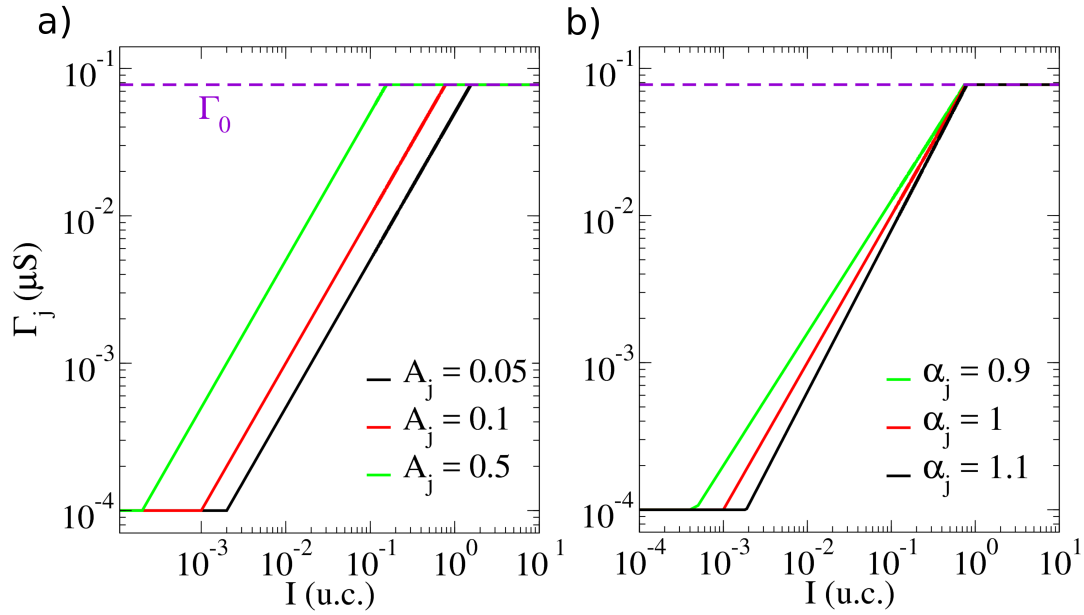


Figure 5.2: (a) The effect of changing the prefactor A_j on the evolution of the conductance of a single NW junction with scaling exponent $\alpha_j = 1$. (b) The effect of changing the scaling exponent on the conductance evolution for a NW junction with $A_j = 0.1$. The differing I_{th} and I_b are seen in both plots. Note that all junctions begin at a conductance of $\Gamma = 10^{-4} \mu\text{S}$ and finish at a conductance $\Gamma_0 \approx 0.0775 \mu\text{S}$, the upper and lower bound for junction conductivity.

TiO_2 and a TiO_{2-x} layer doped with oxygen vacancies. The electrical response of a junction can be represented as

$$V(t) = \left[R_{\text{on}} \frac{w(t)}{D} + R_{\text{off}} \left(1 - \frac{w(t)}{D} \right) \right] I(t)$$

$$\frac{dw}{dt} = \mu_v \frac{R_{\text{on}}}{D} I(t) \quad (5.1.5)$$

where t is time, D is the full length of the $\text{TiO}_2/\text{TiO}_{2-x}$ junction, μ_v is the mobility of the ions, I is the current, and V is the output potential of the device. The state variable w is the length of the doped layer which modulates the resistance of the junction and can vary between 0 to D . The resistance of the junction clearly varies between R_{on} and R_{off} depending on the value of w .

According to the PL+C model for the conductance scaling of a nanowire junction, the conductance is a dynamical quantity controlled by the current flow. For each

current value the corresponding cumulative charge through the junction is $Q_c = \int_{-\infty}^t I(\tau)d\tau$. Therefore a small increment in I_c yields a similar increment in the cumulative charge such that $Q_c \propto I_c$ or $Q_c = BI_c$. Therefore without loss of generality we can write the power law equation in terms of cumulative charge

$$\Gamma_j = A_j I_c^{\alpha_j} = A_j B^{\alpha_j} Q_c^{\alpha_j} = \tilde{A} Q_c^{\alpha_j} \quad (5.1.6)$$

Where a junction has not reached its ultimate high conductance state the stable current flow is a result of non-resonant electron tunnelling where the conductance follows an exponential dependence on the tunnelling gap

$$\Gamma_j = \Gamma_0 e^{-\beta(D-w(t))} \quad (5.1.7)$$

where β is a decay parameter that characterises the tunnelling barrier. The state variable $w(t)$ in the case of an ECM memristive junction represents the length of the conductive filament bridging the inter-wire junction such that $\Gamma_0 e^{-\beta D} = \Gamma_{off}$. Using the fact that $\frac{dw}{dt} \propto I(t)$ and an approximation for small separations D

$$\frac{d\Gamma_j}{dt} = \Gamma_0 \beta \frac{dw}{dt} = A_j \frac{dQ}{dt} = A_j I(t) \quad (5.1.8)$$

The state equation that determines the growth of the filament is thus

$$\frac{dw}{dt} = \frac{A_j}{\beta \Gamma_0} I(t) \quad (5.1.9)$$

Since $\Gamma_0 = 1/R_{on}$ we obtain the following relationship for A_j

$$A_j = \frac{\mu_v \beta}{D} \quad (5.1.10)$$

This relates the prefactor A_j with the ion mobility, the electron decay parameter and the width of the junction, or in essence the ease at which the filament can form with respect to current levels.

The derivation up to now has assumed $\alpha_j = 1$, the effect of non-linearity in the charge carrier drift is manifested through $\alpha_j \neq 1$. Returning to equation 5.1.8 and not performing an expansion on the exponential in equation 5.1.7 the general form of the state equation is

$$\begin{aligned}\Gamma_j &= \Gamma_0 e^{-\beta(D-w(t))} = A_j Q^{\alpha_j} \\ \frac{d\Gamma_j}{dt} &= \Gamma_0 \beta e^{-\beta(D-w(t))} \frac{dw}{dt} = A_j \frac{d}{dt}(Q)^{\alpha_j} = A_j \alpha_j Q^{\alpha_j-1} I(t) \\ \frac{dw}{dt} &= \frac{\mu_v}{D\Gamma_0} I(t) e^{-\beta(D-w(t))} \alpha_j (Q(t))^{\alpha_j-1} = \frac{\mu_v}{D\Gamma_0} I(t) f(W/D, \alpha_j, Q_c(t))\end{aligned}\quad (5.1.11)$$

The non-linearity of the scaling exponent is captured by the additional functional $f(\alpha_j, W/D, Q_c(t))$. Thus α_j can be interpreted as the non-linearity of the derivative of the state variable w , the length of the doped layer, on the driving current. While this analysis was particular to a TiO₂ material the length of the doped layer, w can be associated with the length of the conductive filament and so links the interpretation of A_j and α_j to the conductive filament model.

In this section experimental evidence for the memristive nature of nanowire junctions and NWNs was presented and the PL+C model for nanowire junction memristance was introduced. In the next section a computational routine to simulate networks of such junctions is described and used to understand the self-similar scaling and conductance plateaus in the NWN's memrsitance.

5.2 MEMRISTANCE IN A NANOWIRE NETWORK

The PL+C model can be applied to a NWN by allowing the conductance of each junction in the network to vary with respect to current flowing through them, requiring the calculation of current flow through each junction in the network. By solving Kirchhoff's set of linear equations the potential of each wire V_i in the JDA or each connection node in the MNR mappings is obtained and using Ohm's law

the current flow through the junction is calculated. Consider the junction connecting nodes m and n connected by the junction of conductance Γ_j^{mn} , the current flow is calculated as

$$\mathcal{I}_{mn} = |V_m - V_n| \Gamma_j^{mn} \quad (5.2.1)$$

Knowing the current flow an updated junction conductance $\bar{\Gamma}_j^{mn}$ can be calculated using the PL+C

$$\bar{\Gamma}_j^{mn} = A_j \mathcal{I}_{mn}^{\alpha_j} \quad (5.2.2)$$

This updating scheme must be applied recursively to every junction in the network once a change in sourced current through the network has occurred.

Before the computational routine is discussed in more detail, the different node voltage mappings MNR and JDA must be discussed in the context of memristive junctions. Recall that the MNR model scheme includes junction resistance ($R_j = 1/\Gamma_j$) and inner wire resistance (R_{in}) contributions interacting in a voltage-node network frame. While R_j characterises a dynamical quantity in accordance to equation 5.1.1, R_{in} is fixed and it is given by $R_{in} = \rho\ell/A_c$ where ρ is the wire resistivity, ℓ is the wire segment length and A_c is the cross sectional area of the wire. The inclusion of inner-wire resistance is not entirely necessary for these simulations of an Ag/PVP NWN, as the junction resistances will be between $10^7 - 10^4 \Omega$ compared with the resistance of inner-wire resistance which is of the order of tens of Ω . Inner wire resistance was included as it is needed for the current colour mappings that will be discussed in the section following this.

Simulations begin with the sourced current at some minuscule value and iterating it up to some predefined maximum I_{max} . At each current-step, the potential of each node \vec{V} in the network is calculated with Kirchhoff's matrix equation. The current flow through each junction is calculated according to equation 5.2.1 and the junction resistances are then updated with equation 5.2.2. After each junction

has been updated and the values stored in the Kirchhoff matrix, the conductance of the entire network (Γ_{nt}) is then calculated. Following this the current is iterated to a new value and the junction update routine occurs again. For the first iteration, $\Gamma_j^{nm} = \Gamma_{off} \forall (n, m)$ internode pairs and junctions are updated until they reach their maximum conductance Γ_0 . The work-flow diagram of the computational model can be seen in Figure 5.3.

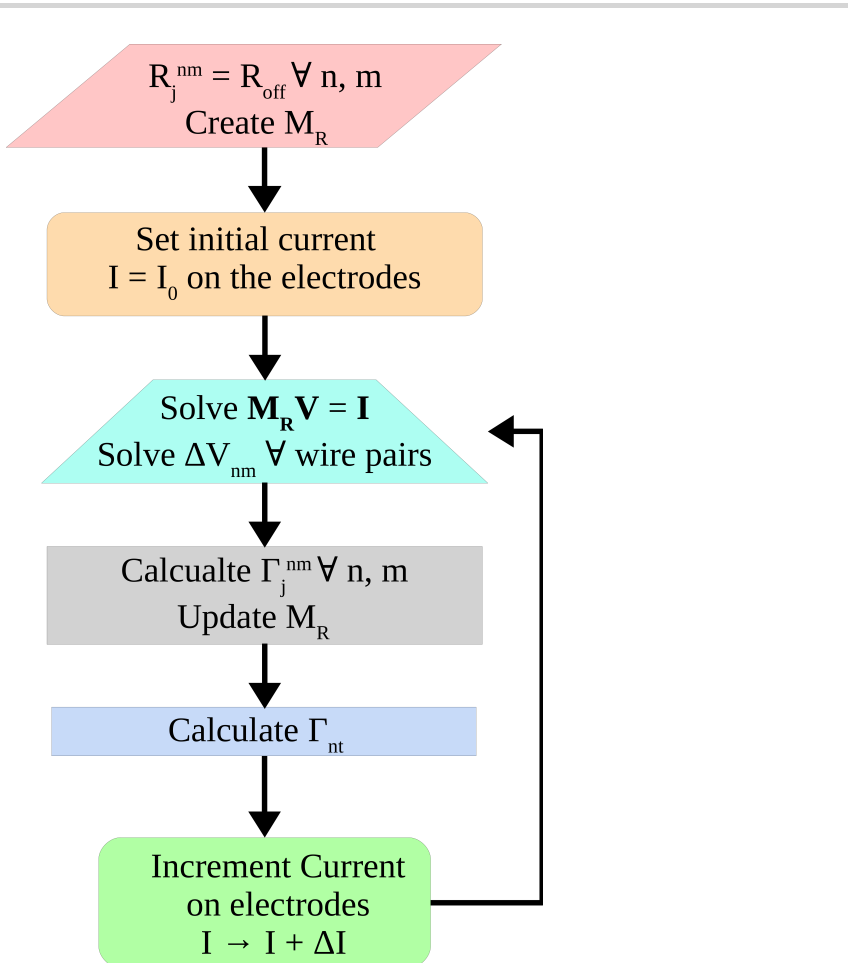


Figure 5.3: A workflow diagram of the computational implementation of PL+C junction model onto macroscopic networks. The algorithm obtains the conductance evolution of NWNs subjected to an electrical current source. See main text for detailed explanation of the algorithm.

In order to remove random connectivity profile effects from determining the role of different A_j and α_j combinations on the evolution of a network conductance, an identical digital NWN geometry was used for each simulation. An experimental

sample of size $\approx 20 \times 20\mu\text{m}^2$ with wires of average length $6.7\mu\text{m}$ and of density 0.49 nanowires/ μm^2 was digitised using the method outlined in chapter 2. Figure 5.4(a) is an SEM image of said sample. Figure 5.4(b) is a digitised version of the NWN where wires are represented by grey sticks and the electrodes as thick vertical yellow lines. Figure 5.4(c) is a visualisation of the connectivity profile that is obtained from the digitised geometry of the NWN. Black dots represent memristive nanowire junctions and the two yellow dots are the two electrodes. Note all dots are connected by straight lines which correspond to current carrying inner-wire segments.

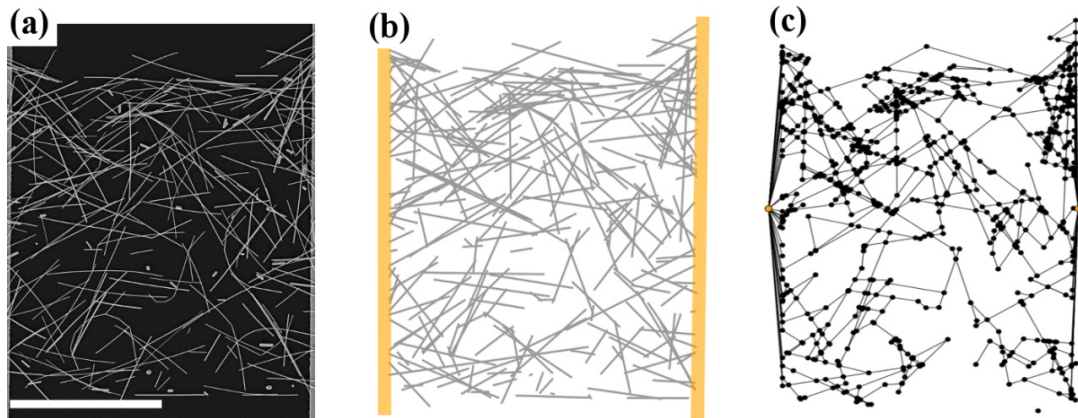


Figure 5.4: (a) An SEM image of a NWN fabricated from Ag PVP core shell Nanowires that have a mean length of $\approx 6.7\mu\text{m}$ and a network size of $\approx 20 \times 20\mu\text{m}^2$ with a wire density of 0.49 nanowires/ μm^2 . The bottom scale bar represents $10\mu\text{m}$. (b) is a digitised version of the NWN obtained using the technique outlined in chapter 3. The grey lines represent nanowire and the thick vertical yellow lines represent the electrodes. (c) A graphical representation of the digitised NWN geometry from (b). The electrodes are represented by the two yellow dots on either sides of the figure, black dots are NWN junctions and the straight black line segments that connect junctions are current carrying wire segments.

Figure 5.5 presents the effect on the conductance curve evolution for different combinations of the parameters A_j and α_j . Even though the junction characteristics are well defined, how current will flow through a collective of these junctions and the resulting macro scale network conductance is not clear. As discussed in the previous section there are three distinct parameter spaces that are determined by

the exponent value;; sub-linear, linear, and supra-linear exponents are expected to have varying evolution characteristics. Figure 5.5(a) the conductance curves for exponent $\alpha_j = 0.9$ are shown for three different values of A_j . The left-most curve has the highest value of $A_j = 0.5$ and it decreases for each curve as one moves to the right, the exact labelling for each curve is displayed at the top of panel (b). This behaviour is of course expected as recalling from equation 5.1.3 $I_b \propto A_j^{\frac{-1}{\alpha_j}}$ and so the greater A_j is, the lower the current a junction will begin to improve conductance at. Recall A_j can be interpreted as the ease of conductive filament formation for the MIM material. Notice that the conductance curve gradually decreases in slope with higher current levels, the $A_j = 0.5$ curve in particular almost reaching the horizontal at $I = 10\mu\text{A}$ meaning that the majority of junctions are reaching the LRS.

Figures 5.5 (b) and (c) present the conductance curves for exponents $\alpha_j = 1$ and 1.1 respectively, again with varying A_j values in each case. The same behaviour is seen as before where systems with higher A_j values begin to strengthen first. However for linear and supra-linear junction dynamics the smooth conductance growth seen for the sub-linear case is lost. In particular for exponent $\alpha_j = 1.1$ in figure (c) after an initial power law scaling phase the conductance growth is characterised by long plateaus of an Ohmic response to increasing current punctuated by sudden increases in NWN conductance which shall be discussed in more detail later in this section. Similar to the sub-linear case the network conductance begins to become more horizontal for $A_j = 0.5$ at high currents meaning that this behaviour applies to the three exponent regimes.

In panels (a)-(c) in Figure 5.5 a dotted line representing a fitted power law is visible, slightly offset to the $A_j = 0.01$ curve for each exponent. This fitted curve has a slope of $\alpha_{NT} = 0.892$ in panel (a), extremely close to that of the exponent of individual junctions. In fact this self-similar scaling between networks and junctions is seen for each A_j, α_j shown in Figure 5.5, where the slope of the PL regime in each case agrees closely with the junctions slope of which the network comprises. This

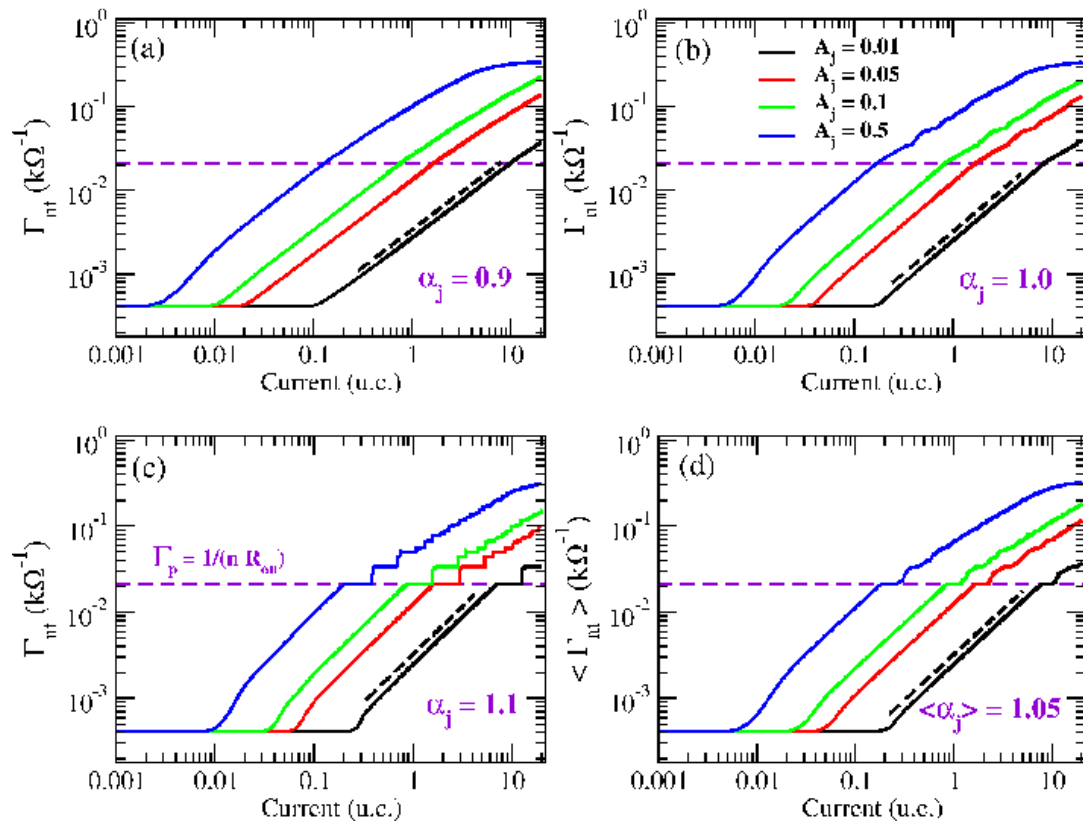


Figure 5.5: The conductance versus current plots for the memristive response model applied to the Network geometry outlined in Figure 5.4. Simulations with different values of A_j and $\alpha_j = 0.9$ (Figure (a)), $\alpha_j = 1$ (Figure (b)), $\alpha_j = 1.1$ (Figure (c)), $\langle \alpha_j \rangle = 1.05$ (Figure (d)). In the latter case the junction exponents in the NWN follow a truncated Gaussian distribution with a mean value of $\langle \alpha_j \rangle$, a standard deviation of 0.1, and is truncated at [1,1.1]. The black dotted lines represent fitted power laws to the PL regime of the $A_j = 0.01$ case for each exponent value and is slightly offset to the curve for ease of viewing. The prefactor and exponent for these power laws, along with these parameters for fits to each of the other conductance curves are presented in Table 5.1. The horizontal purple lines shown in each figure represents the conductance of the optimal path between electrodes, where there are 4 junctions in their low resistance states connected in series $\Gamma = 1/4\Gamma_0$. The number of junctions in the optimal path between electrodes were determined by Network analysis of Figure 5.4(c).

supports the experimental evidence for self-similar scaling presented in section 5.1. The prefactor A_{nt} and exponent α_j for each sample shown in figures (a-c) is shown in Table 5.1. Interestingly the values of α_{NT} and A_{NT} are independent from one another, depending only on their respective junction values A_j , α_j .

A_j	0.01	0.05	0.1	0.5
$\alpha_j = 0.9$	{0.0027, 0.892}	{0.0027, 0.892}	{0.0266, 0.9}	{0.1407, 0.925}
$\alpha_j = 1$	{0.0025, 1.0}	{0.0125, 1.0}	{0.0251, 1.0}	{0.13071, 1.024}
$\alpha_j = 1.1$	{0.0024, 1.115}	{0.0125, 1.115}	{0.0251, 1.113}	{0.13941, 1.159}
$\langle \alpha_j \rangle \geq 1.05$	{0.0025, 1.054}	{0.0125, 1.049}	{0.0251, 1.051}	{0.1323, 1.071}

Table 5.1: The Network prefactor (A_{NT}) and scaling exponent α_{NT} for each combination of A_j and α_j obtained from fitting power laws $\Gamma_{NT} = A_{NT}I^{\alpha_{NT}}$ to the conductance curves shown in Figure 5.5. The prefactors and exponents are presented as $\{A_{NT}, \alpha_{NT}\}$ in this table.

The horizontal purple dotted line represents conductance of four junctions in series that are in the low resistance state $\Gamma_p = \Gamma_0/4$. According to the graphical representation of the NWN sample the memristive model was applied to, which is shown in Figure 5.4 (c), there are precisely four junctions in the shortest path between the two electrodes. This fact gives a clue as to the networks behaviour during and after the PL regime. For the sub-linear and linear exponent simulations the conductance curves begin to diverge away from the initial power law scaling in a gradual manner. In the supra-linear case a plateau is seen at precisely Γ_p suggesting that the network conductance is dominated by four low resistance state junctions in series. In this scenario all of the current in the NWN may be funnelled through a single low-resistance path, or a winner-takes-all (WTA) pathway. Further evidence of localised current flow is that $A_{NT} \approx A_j/4$ for exponents $\alpha_j \geq 1$ in table 5.1, except for the $A_j = 0.5$ case. This can be explained as four conductors in series scaling in unison with increased current flow

$$\Gamma_p(I) = \frac{1}{n} \sum_{j=k}^n A_j I^{\alpha_j} = \frac{A_j}{4} I^{\alpha_j} = A_{NT} I^{\alpha_{NT}} \quad (5.2.3)$$

This relationship for localised current flow is manifest by the self similar scaling and the fact that $A_{nt} \approx \frac{A_j}{4}$ for each of the simulations where $\alpha_j \geq 1$ bar the case with $A_j = 0.5$. The exact nature of current flow through the network is further illuminated in the following section.¹

¹ why is this true for linear and sub-linear? Might remove the discussion of A_j . Also why not $A_j = 0.5$, is it the relatively large step size?

Finally in Figure 5.5(d) the sheet conductance where each junction in the NWN is assigned a scaling exponent from a Gaussian distribution centred at $\langle \alpha_j \rangle = 1.05$, with a standard deviation of 0.1 and confined to the range [1,1.1] is shown. Similar to the $\alpha_j = 1.1$ simulations there are clear PL and PPL regimes with plateaus forming for each prefactor simulations. The first plateau takes place at $\Gamma_p = \Gamma_0/4$, again suggesting the emergence of a WTA between electrodes. The black dotted line is the fitted power law $A_{nt}I^{\alpha_{nt}}$ to the $A_j = 0.01$ simulation and it was found to have an exponent $\alpha_{nt} = 1.054$, very close to the average junction exponent. The fitted parameters obtained for PL regions in the other prefactor simulations are shown in Table 5.1 and all have exponents close to 1.05. A noticeable difference between these simulations and those shown in Figure 5.1 (c) is that the jumps between subsequent plateaus in the PPL take on a smoother profile.

In the supra-linear scaling simulations in Figures 5.5(c)&(d) distinct conduction regimes are evident for networks. The different regimes are identified in Figure 5.6 for a simulation with $A_j = 0.05$ and $\alpha_j = 1.1$. The OFF regime is the initial Ohmic response of a NWN to low current levels, where current flowing through junctions in the NWN are too low to begin the process of junction evolution and so all junctions in the NWN are in the R_{off} state. Following this is the initial evolution of the junctions in the Transient Regime (TR) which is characterised by a varying network strengthening rate which converges onto a power law. The power-law (PL) regime is the portion of the networks behaviour where it scales with an exponent similar to that of the junction. The PL regime continues until until the first plateau in the supra-linear case (Figure (c&d)) or until a point of divergence in the linear and sub-linear cases (Figures 5.5 (a&b)). The behaviour following the PL regime is known as the Post-power law (PPL) regime and appears as a divergence of the networks conductance away from the power law and towards the horizontal. These conducting regimes are further explored in the following section.

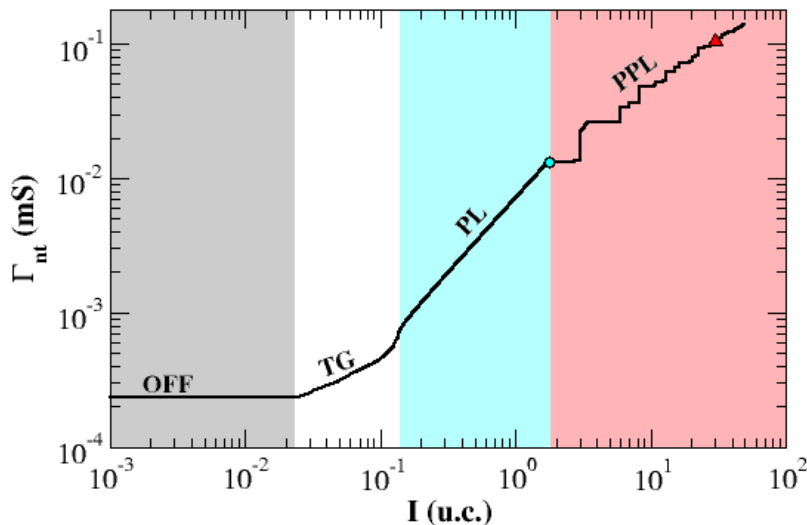


Figure 5.6: Network conductance (Γ_{nt}) versus current for a network with $\alpha_j = 1.1$ and $A_j = 0.05$. There are four regimes of network conductance evident in this plot; the OFF regime corresponds to current levels that are not sufficiently large to begin junction evolution. The transient growth (TG) occurs where the networks conductance begins to increase away from Γ_{off} where it reaches the power-law (PL) regime that is characterised by a power-law with an exponent approximately that of the junctions. The first plateau occurs immediately after the PL regime and heralds the beginning of the post-power-law regime.

5.3 CURRENT COLOUR MAPS

A useful tool in understanding the nature of emergent memristance in a NWN is to calculate the current flow through every individual wire segment and plot a 'heat-map', where colour intensity corresponds to current flow. Using the MNR model the current flowing through a wire segment bounded by two connection nodes m and n is simply the voltage difference over it divided by the resistance of that segment.

$$J_{mn} = \frac{|V_m - V_n|}{(R_{in})_{mn}} \quad (5.3.1)$$

At every iteration of the computational model the current through each wire segment was recorded and used to generate the current colour maps. Figure 5.7 presents conductance for a network in three scaling regimes plus their corresponding current colour maps. The current colour maps are linked to the conductance curve to the left via the symbols located at the top right of each map (star, triangle, and circle symbols). Figure 5.7(a) is the conductance curve for a network with $\alpha_j = 0.9$ with the current colour mappings to the right. The first mapping ($I = 1.0$ u.c.) is linked with the star symbol is set in the PL scaling regime of this network. Here one can identify several paths through the network that are carrying the current as the lighter paths set against the blue background. As the current is increased to $I = 3$ u.c. (triangle symbol), the current flow intensifies through these main paths and additional paths begin to form through the network also. At $I = 9.3$ u.c. (circle symbol) the network is well into the PPL regime and several paths are carrying the current across the network in a relatively homogeneous manner. Figure 5.7(b) contains the conductance curve and current colour maps for a network with $\alpha_j = 1$. Here a similar behaviour is seen between it and the sub-linear scaling simulation, the current flow is dispersed through several paths between the electrodes. However in the PPL ($I = 9.3$ u.c.) the current flow is more confined than the sub-linear case but not significantly.

In the supra-linear simulation, Figure 5.7(c), a striking difference is clear between it and simulations with smaller scaling exponents. In the PL regime the current is predominantly flowing through a single pathway as opposed to the more distributed current flow seen for $\alpha_j \leq 1$. The single path that emerges in the PL regime taken in conjunction with the fact that the first plateau occurs at a conductance Γ_0/n where n is the number of junctions in the path is clear evidence of the winner-takes-all behaviour of supra-linear scaling NWNs. As the current is increased and the network enters the PPL regime the origin of additional plateaus are the emergence of additional paths between the electrodes. In this case the network creates a second path that is entirely independent from the first. At $I = 7$

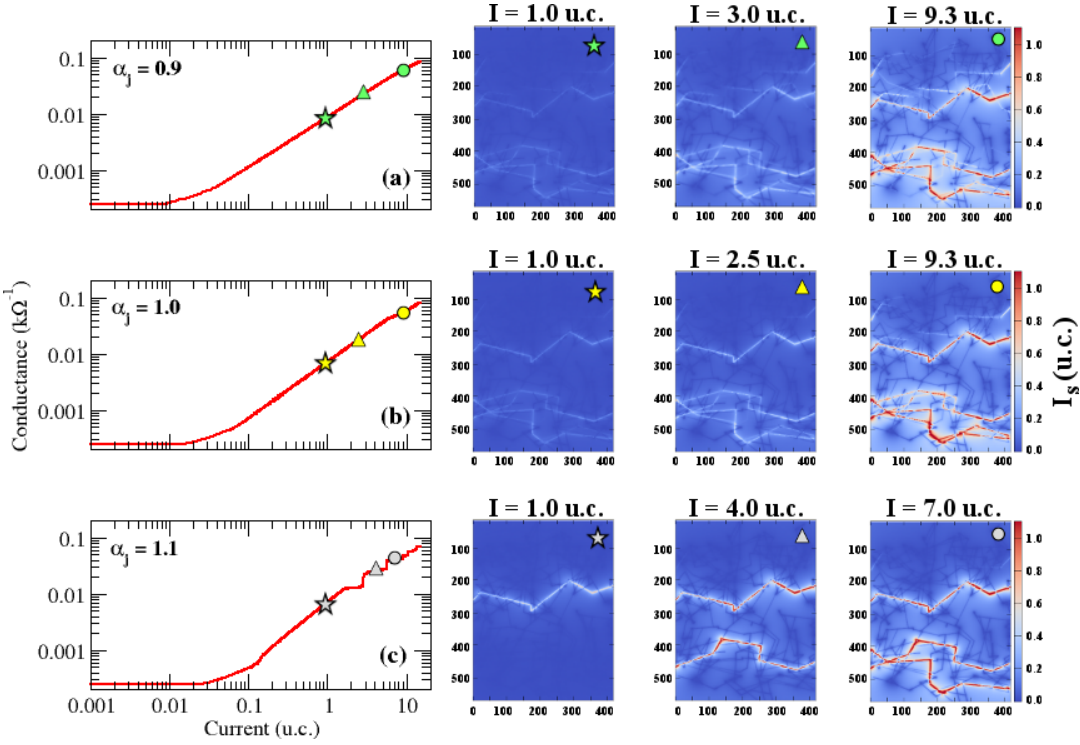


Figure 5.7: (Far left panels) Network conductance (Γ_{nt}) versus sourced current (I) curves taken for a Ag NWN made with PL junctions of $A_j = 0.05$ and distinct exponents: $\alpha_j = 0.9$ (top), $\alpha_j = 1.0$ (middle), and $\alpha_j = 1.1$ (bottom). The currents are expressed in units of current (u.c.). The symbols mark points in the curves in which current colour maps were taken. (Three right panels) CCMs calculated over each wire segment of the network. Snapshots were taken for three current values specified on the top of each current map and distinguished by the symbols: star (set in the PL regime), and triangle and circle (both set in a post-PL regime).

u.c. which is well into the PPL, another path emerges but it is not wholly independent from the second path that emerged as they share a junction. The emergence of winner-takes-all paths leads to a unique behaviour in the networks memristive response with the sequential emergence of highly conductive pathways across the network. Figure 5.8 is a closer examination of the current colour maps of a different network geometry at different points in the networks conductance strengthening, particularly the TG regime.

Figure 5.8 presents a NWN with memristive parameters, $A_j = 0.05$ and $\alpha_j = 1.1$. The network conductance is shown in Figure 5.8(a) and conductance maps at various current levels are panels (b)-(e). Each current scan is labelled with a different

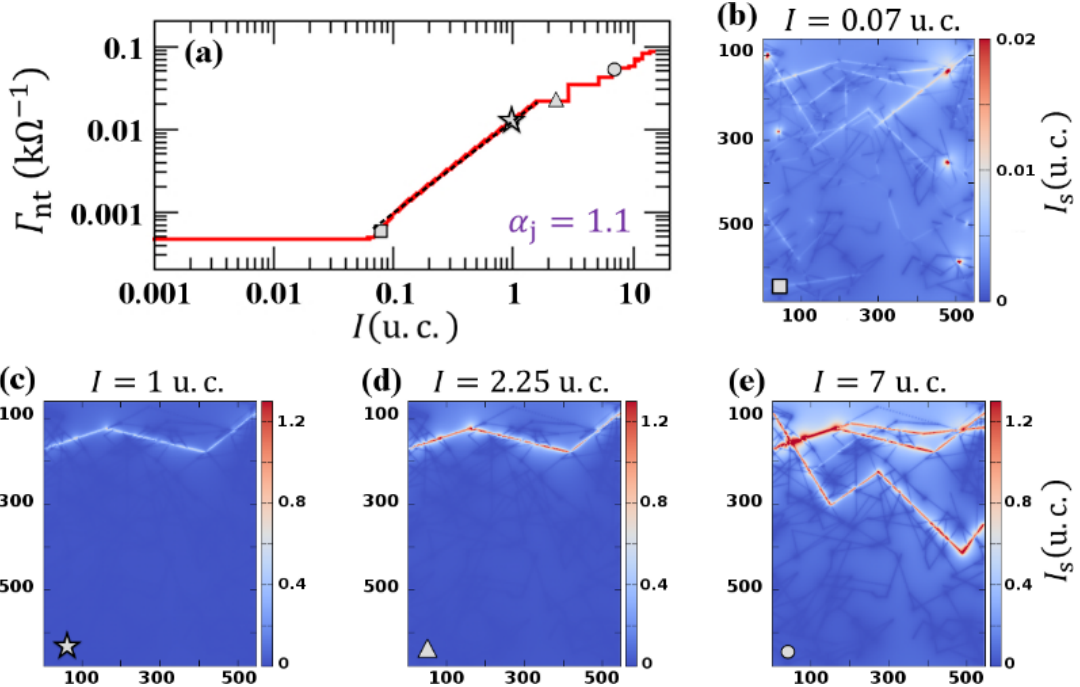


Figure 5.8: (a) Conductance versus sourced current (I) calculated for an Ag-PVP NWN made with power law junctions of $A_j = 0.05$ and $\alpha_j = 1.1$. The black dotted line is a power law with $\alpha_{nt} \approx 1.1$ displaying self-similarity between the NWN and junction. The symbols mark points in the curves in which current maps were taken, a mapping was made in four different scaling regimes of the NWN; the transient growth (square), the power law (star), the first plateau (triangle), and the post power law (circle) regimes.

symbol (square, triangle and so on) which is then connected with a position on the conductance curve. The square symbol on the conductance curve is at $I = 0.07$ and the corresponding current scan is visible in Figure 5.8(b) which is a visualisation of the TG regime. The current flow is spread throughout the network in order to transport current in the most energy efficient manner. In contrast, the power-law regime sees the emergence of a highly localised current flow through the network, which shows that the self-similar scaling between the junction and network conductances is indeed a consequence of the the current flow confined to a single path between electrodes. The transient growth region can be understood as current seeking out a particular path which emerges in the PL regime through which the majority of current flow occurs in a winner-takes-all manner. The current mapping for the first plateau is labelled with the triangle symbol and shows

that the winner-takes-all path still dominates the conductance of the junction at this point, the constant conductance at this stage of the networks conductivity means no junctions are increasing in conductance. The conductance of the NWN at this current level is approximately $\Gamma_0/4$ due to their being four junctions in their final high conductance state in the winner-takes-all path. The post power law current mapping shows that several other pathways have emerged in the network at higher current levels (circle label), here the paths in the PPL are not all independent as two of the paths share a junction.

The winner-takes-all response shown for supra-linear junctions has been demonstrated in many simulations of different geometries alongside the two examples shown here⁷. In fact an experimental technique to image electrically connected of a NWN was performed on an Ag/PVP NWN that had been electrically driven into a plateau state. Known as a Passive Voltage Contrast image, the wires that have a stronger electrical contact with either electrode in Figure 5.9 appear as dark areas in the image while the lighter coloured areas are more lightly coloured⁷. Here the localised dark wires indicate that this pathway is significantly more conductive than the surrounding nanowires which further evidences the winner-takes-all response of Ag/PVP NWNs.

Thus far the memristance response of a NWN has been shown for one type of electrode geometry, where two electrodes span the network at opposite ends of a network. In the following section a multi-electrode architecture is presented that allows for a greater exploration of a networks response to winner-takes-all pathways.

5.4 MULTI-TERMINAL

The emergence of WTA paths as highlighted in Figure 5.11 demonstrates the possibility of activating distinct conductance states in a complex network system and

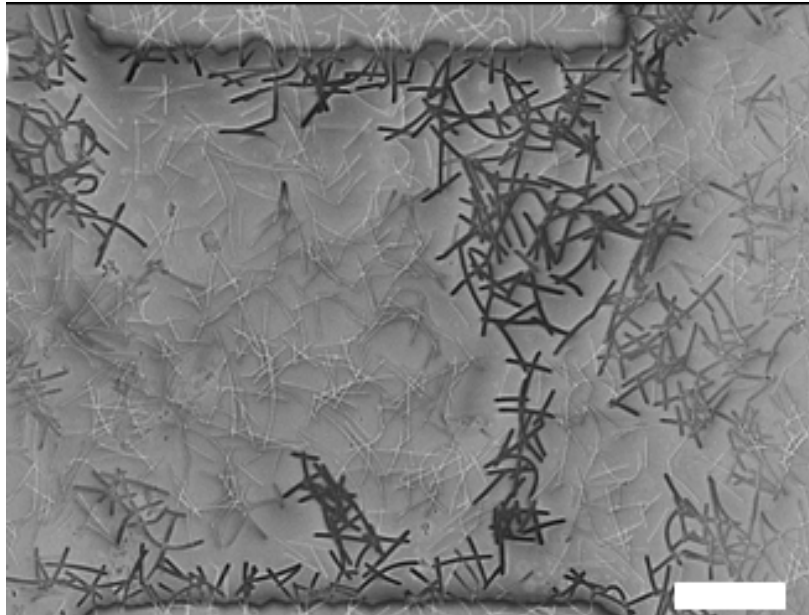


Figure 5.9: A Passive Voltage Contrast image of an Ag/PVP NWN of size $100 \times 100 \mu\text{m}$ that has been electrically driven to a stable conductive state at $50 \mu\text{A}$. The dark wires indicate a strong electrical connection with the electrodes seen to the top and bottom of the image⁷.

this phenomenon has potential neuromorphic applications. To fully realise the potential of memristive NWNs as a neuromorphic device, an architecture that facilitates multiple input signals, i.e. rather than a 2-probe interrogation method, is required. A neuromorphic network requires numerous electrical signals of distinct modulations and amplitudes inputted via a multi-terminal configuration, such as that shown in Figure 5.10. Here the four terminals are represented by thick red vertical lines and the nanowires are randomly dispersed and shown in grey. The four terminal architecture is used as a means to study the effect that the formation of a WTA has on other areas of the network in this section. This will be achieved by developing a WTA path between one of the six possible pairs of electrodes and then calculating the impact it has on the conductance of the remaining pairs.

A plot of the multi-terminal NWN with four electrodes is shown in 5.11(a) along with sketches of the six possible paths between the four electrodes, represented by lines of various colours and in two cases as dashed lines. Current is sourced

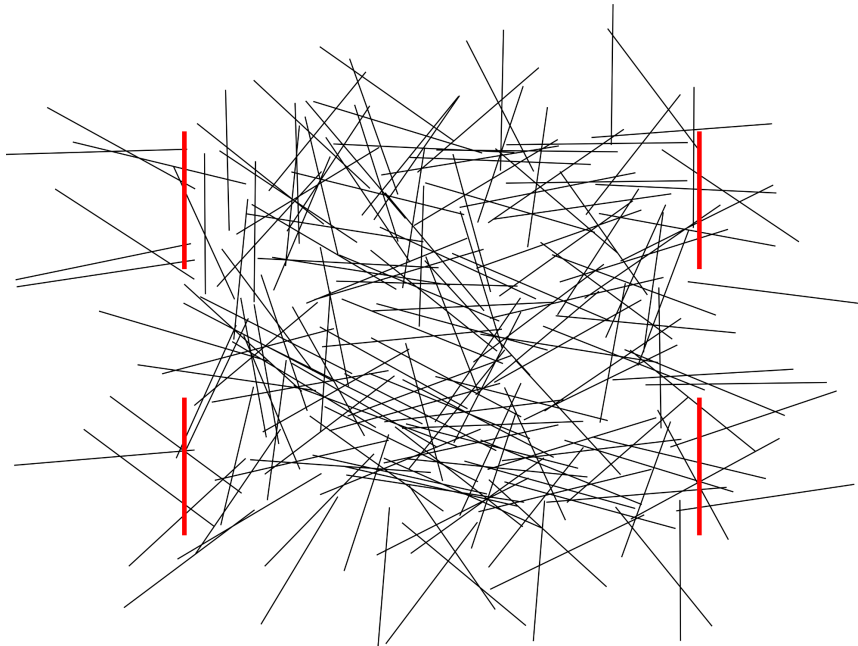


Figure 5.10: A visualisation of a multi-terminal network to enable the formation of multiple WTA paths on the one network. The four terminals are represented by thick vertical red lines and the nanowires as black lines dispersed throughout the device. Four electrodes creates 6 unique electrode pairs between which WTAs can be formed.

and drained between two electrodes only, in this case these were electrodes A and C, the path being evolved will be referred to as \overline{AC} . Junctions were set to evolve with a supra-linear exponent $\alpha_j = 1.1$ in order to facilitate the emergence of a WTA between A and C. After each increment in the sourced current along the path \overline{AC} the conductance of every junction in the NWN is recalculated according to PL+C junction mode and the resistance of every electrode pair in the network is then calculated.

Figure 5.11(b) plots the conductance of each electrode pair in the NWN that was shown in Figure 5.11(a) while the current sourced at electrode A and drained at electrode C is incremented. The main path \overline{AC} sees its conductance increase by over 10,000% during the simulation and reaches its' second plateau. While the other paths in the network were not explicitly evolved by running current through them, their conductances changed as a result of the WTA path \overline{AC} nonetheless. The

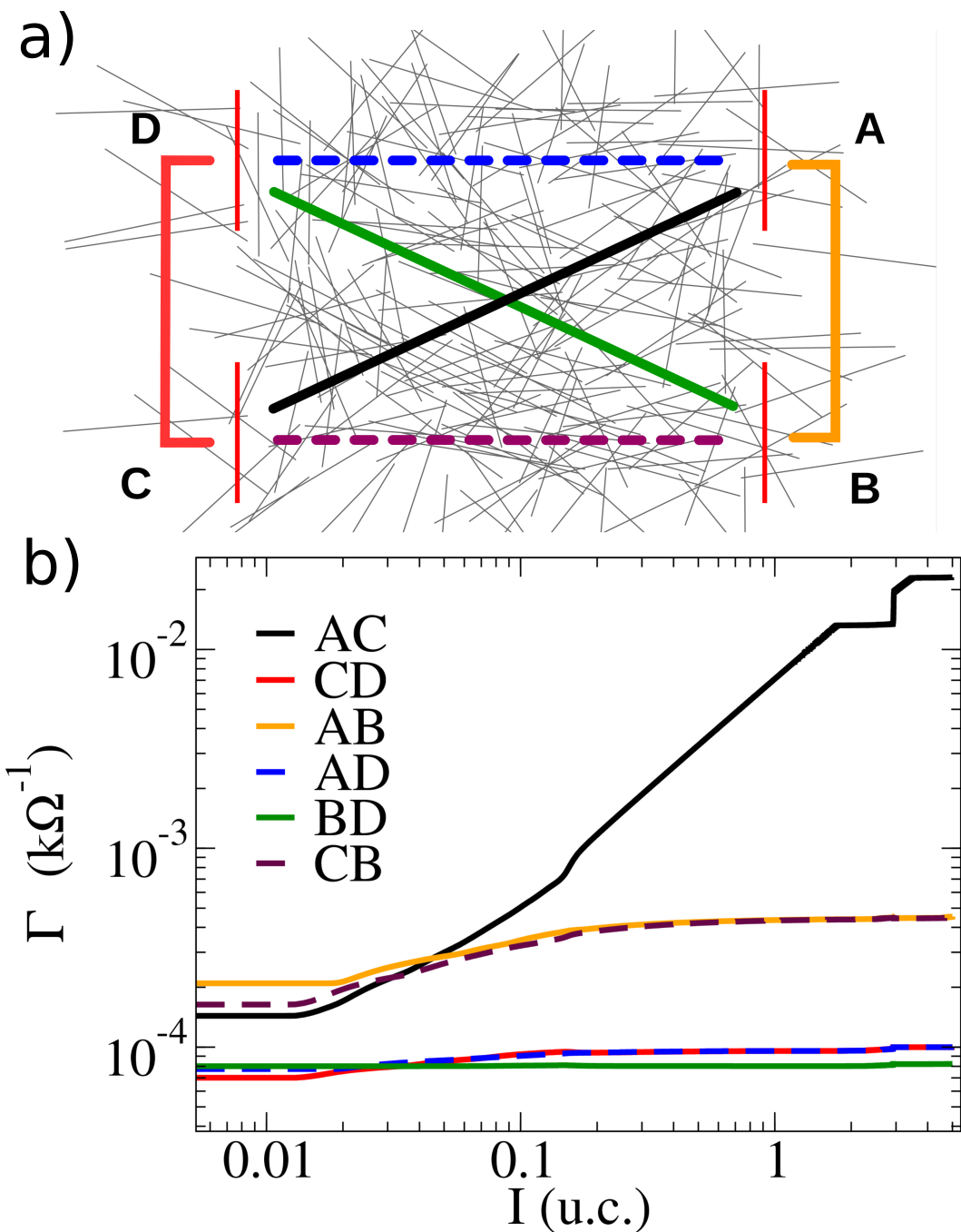


Figure 5.11: (a) A sketch of a multi-terminal NWN with 4 electrodes depicted by vertical red lines (labelled A-D), and light gray lines representing the nanowires. The paths between the terminals are depicted by thick lines of different colours. (b) The inter-electrode terminal for each of the 6 paths depicted in (a). The path between A and C is matured to a high conductance state corresponding to a new memory state while the memory states of the other paths change very little

paths \overline{AB} and \overline{BC} saw an increase in their conductance by over 100% while the paths \overline{CD} and \overline{AD} saw an approximately 30% increase in conductance. The path \overline{BD} which is represented by the green line saw hardly any change in its conductance which is interesting as it is the only path in the NWN that is independent of the electrodes A and C. The negligible change in the path \overline{BD} also explains the change of conductance observed in the other non-driven paths. The evolution of the main path between the electrodes A and C causes a change in conductance for any other path containing these electrodes.

While the multi-terminal device simulated in Figure 5.11 is a proof of concept, it does offer valuable insights into the potential of NWNs as a neuromorphic device. The contamination of non-driven paths by the evolution of a memory state in other paths is undesirable in memory storage devices and device architecture would need to mitigate this. This could be achieved through a large number of electrodes orientated in such a way so that shared junctions in their WTA is unlikely and when it does occur, contamination is minimal. The cross-contamination between memory states does have a novel application in neuromorphic devices as they are a means to achieve associative memory states, for example two paths, \overline{AB} and \overline{BC} , doubled in conductance as a result of the formation of the WTA. Associative memory states means that the development of one memory state has an impact on another, leading to a computational system of high complexity and computational capabilities. This point will be discussed further in the Conclusions and Future Work chapter.

5.5 CHAPTER SUMMARY

In section 5.1 a model was introduced that empirically captured the memristive properties of a nanowire junction as a Power-Law plus Cut-off (PL+C). The PL+C model was developed based of experimental measurements of nanowire junctions which showed a power law relationship between their conductance (Γ_j) and the

current compliance such that $\Gamma_j = A_j I^{\alpha_j}$ where the parameters A_j and α_j are determined from the experimental measurements. The upper bound for a junctions conductance was taken as the quantum of conductance, the conductance of a single channel connecting the nanowires, while the lower bound for conductance was set as 10^{-7}S . The dynamics of the conductance evolution of a nanowire junction was shown to depend sensitively on the parameters A_j and α_j , mainly through the current level at which their conductance starts increasing from Γ_{off} and when it ceases evolution at Γ_{on} .

A method to incorporate the dynamical junction resistance with Kirchhoff's circuit equations was presented in section 5.2 resulting in the capability of simulating the macro-scale memristance of a NWN based on the underlying memristive junctions. The network memristance was shown to have three main scaling dynamics depending on the value of the junction scaling exponent α_j , whether it is sub-linear, linear or supra-linear. In all three cases a self-similar power law was identified between the scaling of junctions and sections of network scalings wherein the network scaled as a power law with an exponent similar to that of the junctions. For supra-linear cases the emergence of highly conductive paths that display a winner-takes-all behaviour was evidenced by the appearance of a steady-state of the NWN's conductance where the network entered a period of inactivity at a conductance corresponding to a single path of fully evolved junctions funnelling all of the current along it. Current colour mappings were introduced in section 5.3 as a means to visualise the current flow through a NWN and showed that the winner-takes-all paths did indeed emerge.

A multi-electrode architecture for a NWN was introduced in section 5.4 such that several addressable inter-electrode paths could be interrogated while one of the paths was driven to a high conductance state. The main path saw an increase of over two orders of magnitude in its conductance as a winner-takes-all path was formed between the two driven electrodes. Other paths in the NWN did not see such a dramatic increase in conductance, no more than a factor of two. One path-

way did not increase in conductance whatsoever meaning that it was unaffected by the formation of the high conductance winner-takes-all. These results suggest that several independent addressable memory states could be stored in a NWN. The results also hint at a process to achieve associative memory states in a NWN through the use of shared electrodes, a remarkable property of a randomly connected set of Nanowires.

6

COMPARISON OF A CAPACITIVE AND MEMRISTIVE JUNCTION ACTIVATION PROCESS

In the previous chapter the memristive activation of a NWN undergoing electrical stressing was introduced. This junction activation is a current driven process requires increasing current levels through the NWN which causes the conductance of each junction to change in an analogue manner up until their final high conductance state. It was also shown that the MRM has activation patterns that are highly dependent on the properties of the junction, for supra-linear junction scaling the emergence of highly localised current flows through the networks emerges in a ‘winner-takes-all’ manner, while for linear and sub-linear exponents the junctions activate in a less localised manner. The MRM is not the only contemporary model that describes the dynamical activation of nanowire networks however. In recent publications the inter-wire junctions have been treated as a capacitor which breaks down when the potential across the junction reaches some critical value, causing an electrical connection between the nanowires^{80,89,102}. The capacitive junction model (CPM) has been used to identify the activation voltage of the network, i.e the voltage required to begin current flow through the network. At the point of network activation, a shorting path between two electrodes which facilitates current flow.

The expected response of the network to a capacitive junction breakdown activation model is hinted at in Passive Voltage Contrast (PVC) images performed at low leakage current levels. Figure 6.1 (c) presents a PVC image of a nanowire network at very low leakage current (100’s pA) that was experimentally captured. In this

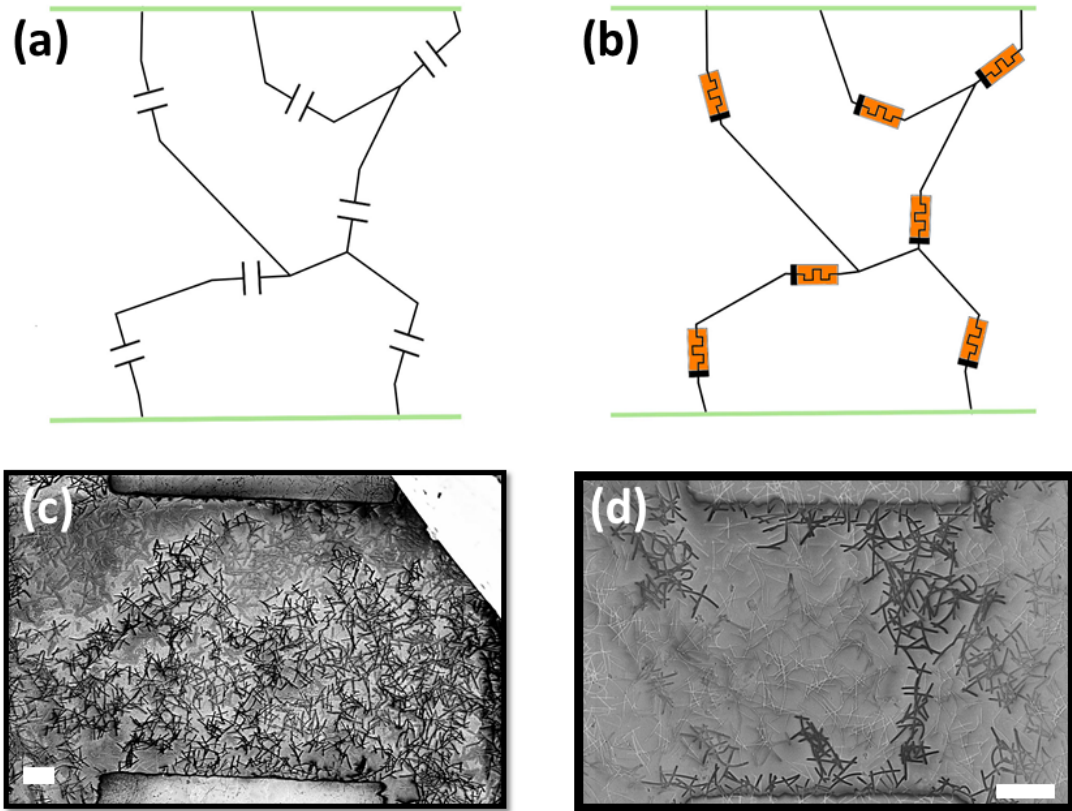


Figure 6.1: (Top panels) Circuit sketches representing a NWN being described by a (a) capacitive model (CPM) and a (b) MR model (MRM). Each lumped circuit element is assigned to model the electrical characteristics of the interwire junctions in their respective formation (capacitors) and adaptive conducting (memristors) modes. Horizontal green lines represent metallic electrodes. (Bottom panels) PVC SEM images of Ag NWN samples subjected to distinct I-V characterizations. In (c), the image was taken by holding the source voltage at 2 Volts and setting a leakage current of few hundreds of pA. The network dimensions are $200 \times 200 \mu\text{m}$ and the white scale bar corresponds to $20 \mu\text{m}$. In (d), the image was taken from a full I-V sweep with a limiting current compliance of 500 nA . The network dimensions are $100 \times 100 \mu\text{m}$ and the white scale bar corresponds to $2 \mu\text{m}$. Darker wires are grounded to the electrodes meaning that their junctions were optimized in response to the given excitation. Almost the whole network is featured in the capacitive/formation regime whereas a single WTA path is contrasted in the memristive/conducting regime. More details on this experiment can be found in⁷.

image the dark wires represent those that have the strongest electrical connection with the electrodes. This low leakage current is too low to begin the memristive evolution of junctions and corresponds to a capacitive junction response. Figure 6.1(d) is a PVC image performed at 500 nA , a level at which memristive evolution

has begun and here a localised electrical connection is depicted by the dark wires and is a manifestation of the WTA behaviour shown in the previous chapter. These images suggest that networks will behave differently in the CPM and MRM, these behaviours will be compared in this chapter.

The aim of this chapter is to introduce and characterise certain traits associated with the CPM and contrast this with the dynamics of networks undergoing memristive activation. This is achieved by applying the CPM and MRM to an identical network geometry, as sketched in Figures 6.1(a) and (b). Nanowires connected by either capacitive or MR junctions are complementary models whose applicability depends on how the networks are interrogated. The capacitive response is dominant when the network is interrogated by extremely low currents (\sim pA); in this regime, each junction is represented by a capacitor which breaks down if the voltage drop across it exceeds its characteristic threshold voltage making an electrical contact between the wires. Once this occurs, the junction becomes a memristor at a high-resistance state (HRS) and sufficiently small currents can flow through it. As more current is adiabatically sourced onto the network, the MR state of these junctions can be continuously evolved up to their respective low-resistance state (LRS).

This chapter will highlight the main difference between the activation of a network with binary state junctions (CPM) and analogue state junctions (MRM). The layout of this chapter is as follows. The capacitive junction model along with the computational framework to apply it to a NWN is introduced in section 6.1. The activation patterns of the CPM is illustrated in section 6.2 and here it is contrasted with that of the MRM by applying both to an identical network geometry. In section 6.3 the CPM is shown to have a scale free response to network perturbation resulting in mass junction activation events that can propagate through across the entire network. The fault tolerance of networks in both activation models are contrasted in section 6.4 by examining junction activations and network performance after a junction that is central to the networks performance ‘fails’, or is removed

from the mathematical graph for the NWN. There is a chapter summary presented in section 6.5.

6.1 CAPACITIVE JUNCTION MODEL

The capacitive model is relevant to negligible current flows through the network such that the capacitive response of junctions dominates the network's properties. In this scheme, the nanowires are treated as equipotential wire segments and their connections as binary capacitors. This modeling scheme is similar to the JDA approach introduced in chapter 3 in that the junctions define the connectivity profile, this assumption was taken as charge can easily move through the conductive nanowire but not across the insulating barrier in a junction. Depending on the voltage drop across the capacitive junction, it can be either non-activated ($|0\rangle$) or activated ($|1\rangle$). The capacitance state of a junction can flip from $|0\rangle \rightarrow |1\rangle$ if the voltage drop across it is larger than its associated breakdown voltage (V_b), hence a given junction connecting a pair of wires (n, m) can be activated if $|V_n - V_m| \geq V_b$ where V_n (V_m) is the potential at wire n (m). The capacitor activation is characterized by a modification in the capacitance value of the junction as $C_{nm}^0 \rightarrow C_{nm}^1$ where C_{nm}^0 is an estimated quantity determined uniquely by the characteristics of the wires and $C_{nm}^1 \rightarrow 0$ meaning that the junction has lost its capacitive properties and charge will start to flow through it. The values of C_{nm}^0 are estimated by considering interwire junctions as parallel-plate capacitors with $C_{nm}^0 = C^0 = \epsilon_r \epsilon_0 A/d \forall (n, m)$ pairs for the sake of simplicity. In the equation, ϵ_r is the relative permittivity of the dielectric, ϵ_0 is the permittivity of the air, A is the plate area, and d is the plate separation. For our PVP coated Ag NWs, we used $\epsilon_r \approx 2.5$, $d \approx 8$ nm and the area of the plates can be estimated from the NW diameters which range $D \sim 60 - 80$ nm. Assuming an ideal square area projected from two superimposed soft-body wires, $A = D^2$ and $C^0 \approx 18$ attoFarads (aF). The capacitance of wire sections is not

considered by the CPM due to it being negligible for metallic core nanowires. If the CPM was applied to non-metallic wires the CPM should be extended to account for the coupling capacitance of the wires themselves

CPM simulation¹⁰² begins by placing the whole capacitor network in contact with electrodes that source and drain a certain amount of charge Q , representing the charge that builds up due to the applied bias voltage. The applied charge is incremented from an initial value Q_i up to a pre-defined maximum value of Q_{\max} in steps of ΔQ . At Q_i , all junctions are set at $|0\rangle$ -state and at each charge increment the electric potential of each wire is calculated and the potential difference across each junction is checked against the breakdown voltage. A capacitance matrix \hat{M}_c is built taking into account the network connectivity and the potential on each wire is obtained by solving the system of equations $\hat{M}_c \hat{V} = \hat{Q}$ self-consistently. This means that charge on the electrodes is only incremented once all $|0\rangle \rightarrow |1\rangle$ transition activity on the network ceases. A work-flow schematic is shown in Figure 6.2.

At low current levels corresponding to the OFF-threshold in MRM, one can expect to find a capacitive response from the individual NW junctions coupled with some leakage current since their dielectric coating are not expected to be an ideal insulator; a small DC current can always leak through the dielectric material. For example in the passive voltage contrast image in Figure ??(c) the leakage current was of the order of hundreds of pA (10^{-7}A). To account for this dual response, CPM is modified to incorporate leakage current in capacitive networks by considering a parallel RC circuit as a proxy for low current flow in NWNs. A potential difference that is placed across both elements then links the charge accumulated on the NWN with a leakage current through the resistor. The size of the leakage resistor is chosen in order to give leakage currents of the order of hundreds of pA.

The Memristive model follows the algorithm that was laid out in Chapter 5. For the sake of consistency, CPM and MRM were employed on the same NWN skeletons. By using an identical network geometry for both MRM and CPM simulations, the spatial fluctuations can be removed allowing a more direct compar-

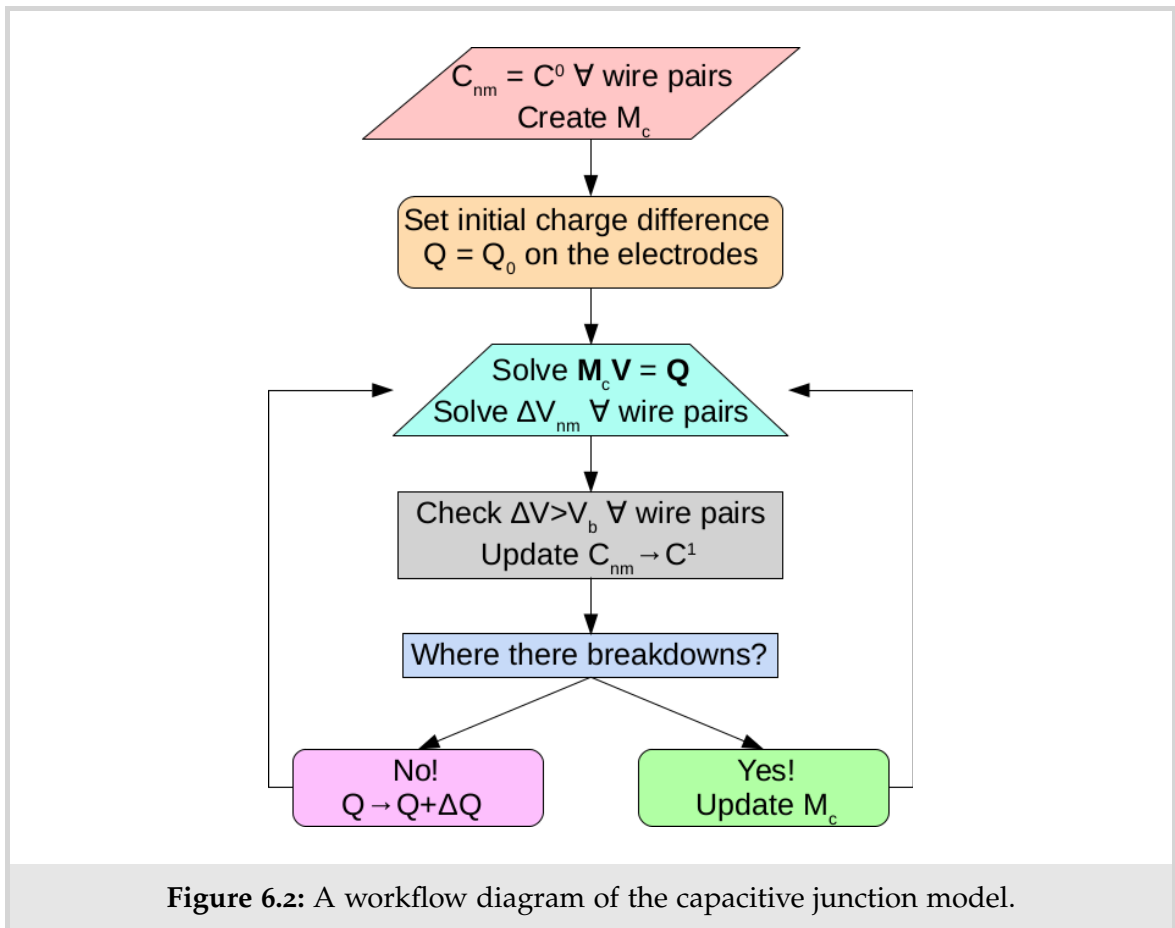


Figure 6.2: A workflow diagram of the capacitive junction model.

son between the activation dynamics of both models. Figure 6.3(a) is a scanning-electron-microscope image of one of our NWN sample made with Ag/PVP core-shell nanowires. This NWN has a wire density of $0.47 \text{ NWs}/\mu\text{m}^2$ and the average length of the wires is approximately $7 \mu\text{m}$. After digitally capturing the geometry of this network using the method introduced in chapter 3, we estimate that this network contains a total of 963 junctions. Figure 6.3(b) shows a stick representation of (a) which was built from the resultant graph⁷⁹.

The CPM model is meant to capture the dynamics of the network at extremely low current levels while the MRM is applicable at higher levels. That being said the two models are mutually exclusive in this thesis, they do not interact and there is no consideration of a dual memcapacitive and memristive response. There are reports of a memcapacitive and memristive response existing on nanoscale junctions^{103–106} but as the models are applied to current regimes orders of magnitude in difference

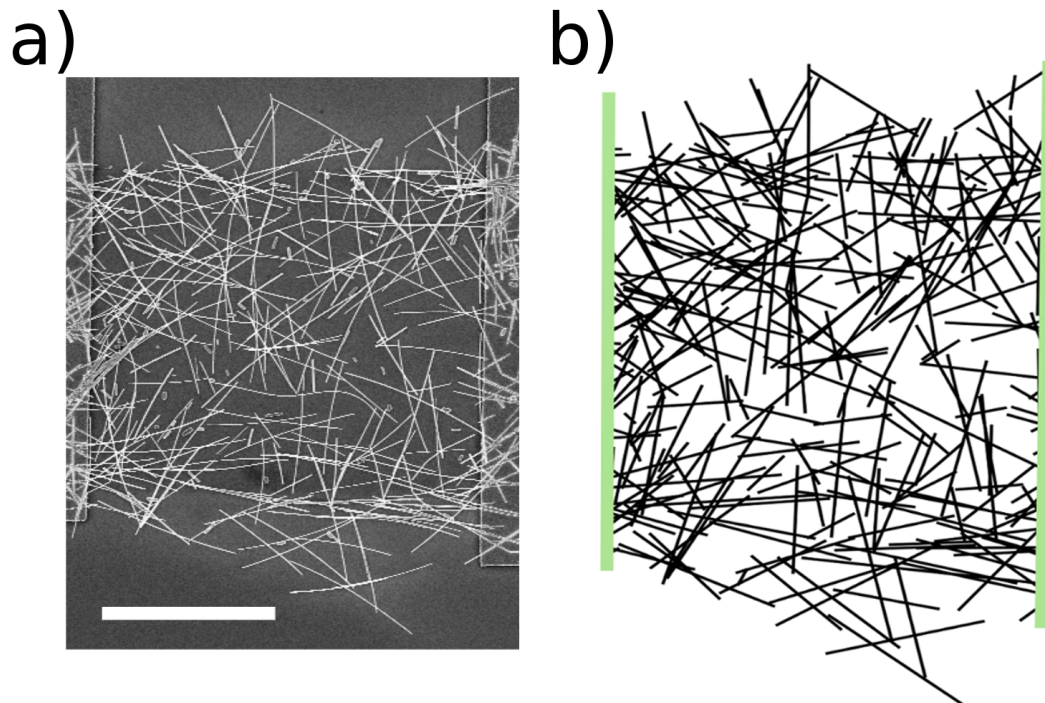


Figure 6.3: (a) An SEM image of an Ag NWN with a wire density of $0.47 \text{ NWs}/\mu\text{m}^2$ and average wire length of $7\mu\text{m}$. Electrodes are located at either sides of the network and the white scale bar at the bottom represents $10\mu\text{m}$. (b) Stick representation of an Ag NWN sample taken from (a). Black sticks represent the Ag NWs whereas the vertical thick green lines represent the electrodes.

in this chapter they were studied in isolation. The dual memcapacitive/memristive properties of a nanowire junction is a potentially fruitfull area worth investigating and will be a subject of future work.

6.2 PATH FORMATION IN CAPACITIVE AND MEMRISTIVE MODELS

Recall from chapter 5 that the hallmark of supra-linear junction scaling was the emergence of winner-takes-all paths between the electrodes. The network geometry shown in Figure 6.3 was set to evolve in accordance to the MRM model outlined

in chapter 5 from which $\Gamma_{nt} \times I$ curves were obtained. Figure 6.4(a) presents the evolution of the network conductance where junctions scale as

$$\Gamma_j = A_j I^{\alpha_j} \quad (6.2.1)$$

with $A_j = 0.05$ and $\alpha_j = 1.1$. The four scaling regimes identified in chapter 5 are labeled in this plot, the initial OFF state, the transient growth (TG) where the network finds the winner-takes-all path and begins its power-law (PL) scaling. As discussed in chapter 5 the network conductance scales as $\Gamma_{nt} = A_{nt} I^{\alpha_{nt}}$ in a self-similar manner to the junctions, i.e. $\alpha_{nt} \approx \alpha_j$. Finally the network enters the post-power-law (PPL) regime where the winner-takes-all path is fully developed and additional paths are fully activated as the current flowing through the network continues to increase.

A visualisation of the activated wires at the end of the PL regime is shown in Figure 6.4(b). An activated wire is one who has a junction driven to the quantum of conductance and is depicted as a black thick wire compared with the light gray thin wires that have no activated junctions associated with them. This WTA path contains 7 junctions evolved to the LRS meaning that just 0.72% of the junctions handle most of the current-flow workload in the PL regime. As more current is sourced onto the electrodes, other conducting paths are enabled in a discrete fashion. The device gradually acquires a two-dimensional character due to the formation of parallel conductive paths. About 80 supra-linear junctions reach their optimum conductive state at $I = 30$ u.c. allowing the network to distribute the input current through multiple conducting paths. This is roughly 8.3% of the junctions taking part in the conduction process. A visualisation of the activated wires at $I = 30$ u.c. is depicted in Figure 6.4(c).

As stated in the previous section the CPM applies to low current levels that are not strong enough to begin the memrisitive evolution of the junctions, this is the OFF scaling regime of a network which is depicted in Figure 6.4(a) and is labeled as such at the top of the plot. Figure 6.5(a) is the gradual breakdown of a capacitive

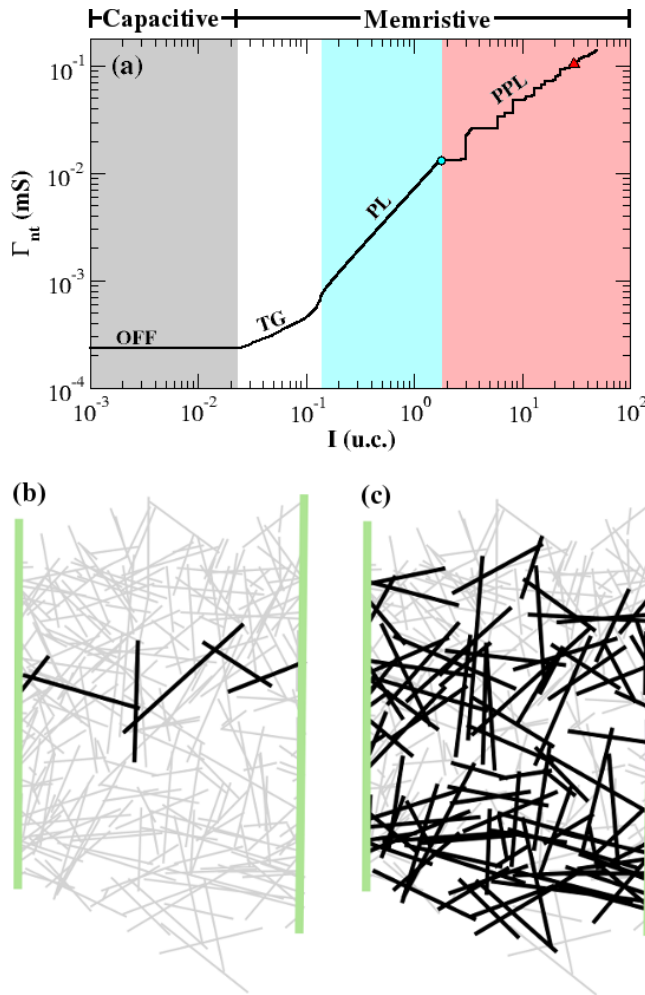


Figure 6.4: (a) Simulated conductance versus current obtained for the image processed Ag NWN shown in Figure 6.3. The curve was taken MRM. All four distinct transport regimes discussed on the main text is depicted on panel and highlighted in different colours: (OFF) OFF-threshold, (TG) transient growth, (PL) power law, and (PPL) post-power-law. Currents are expressed in units of current (u.c.). The junction characteristics are set at $\alpha_j = 1.1$ and $A_j = 0.05$. The blue circle marks the point in the curve in which the junctions comprising the WTA paths are fully optimised at $I = 1.77$ u.c. and $\Gamma_{nt} = 0.013$ mS. This point marks the disruption of the PL conducting regime. (b-c) NWN skeleton in which NWs connected by junctions at the LRS are highlighted in black and in light grey otherwise. The NWN snapshot depicted in (c) was taken at the PPL stage at $I = 30$ u.c.. The OFF conductance region is characterised by no junction resistance change and so it is this region that the CPM is applied to, once the junctions begin to change the network is best described by the memristive model.

network by visualising the leakage current flow required to cause an increasing charge build-up across the capacitor that is in a parallel circuit with the leakage

resistor of $10^{10}\Omega$. One can identify a sudden increase in the required leakage current flow at 6.22 aC. A visualisation of activated wires in the NWN at this point is presented in Figure 6.5(b) where black wires represent those with an activated junction thus giving the wire an electrical connection with either of the electrodes. Junctions that are in contact or are near the electrodes activate easily as the potential difference builds quickest in these areas. Figure 6.5(c) shows the activated wires at the point when a continuous electrical path between the two electrodes has formed. The current levels through the resistor at this point is $1.3 \times 10^{-7}\text{A}$.

A striking difference between both models can be seen here, the number of junctions that are activated before path formation in CPM is much greater than in path formation in MRM. In the CPM there are 61 junctions activated at path formation, i.e. 6.33% of junctions compared with 0.72% of junctions in the WTA path captured in MRM. Not only are activated junctions less concentrated in the CPM at path formation the regions of activations are slightly different. The CPM seems to favour the lower half of the network for activations while the WTA emerges in the center of the network in the MRM. Figure 6.5(d) is a visualisation of the network at a late stage of activation. A large swathe of the network has been activated at this stage, much like the MRM PPL regime depicted in Figure 6.4(c). Note the sudden jumps in the required leakage-current flow associated with clusters of breakdown events that are crucial for the development of the MR properties of the NWN during its adiabatic electrical stress. These jumps correspond to the sudden activation of wires in the network causing the effective capacitance of the network to drop suddenly. The current level through the resistor during capacitive activation is in the order of 10^{-7} A which compares favourably with current levels of hundreds of pA measured in the PVC image shown in Figure 6.1(c) and yet well below the current levels required for junction evolution in the MR regime. As with the memristive response of a NWN, the junctions that are activated and the order in which they do so are determined by the Network connectivity. The CPM cannot be applied

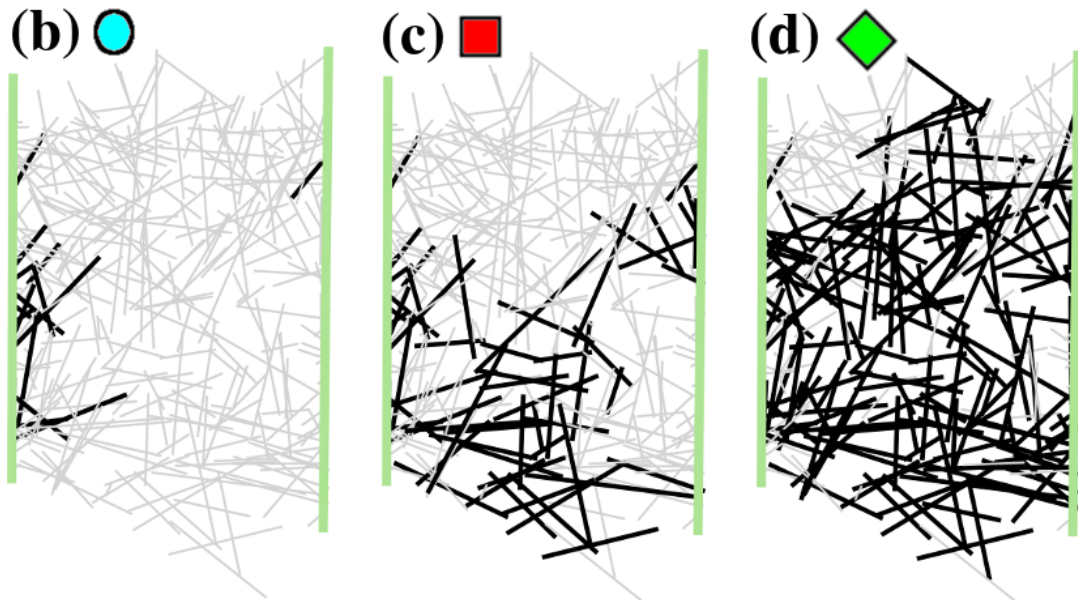
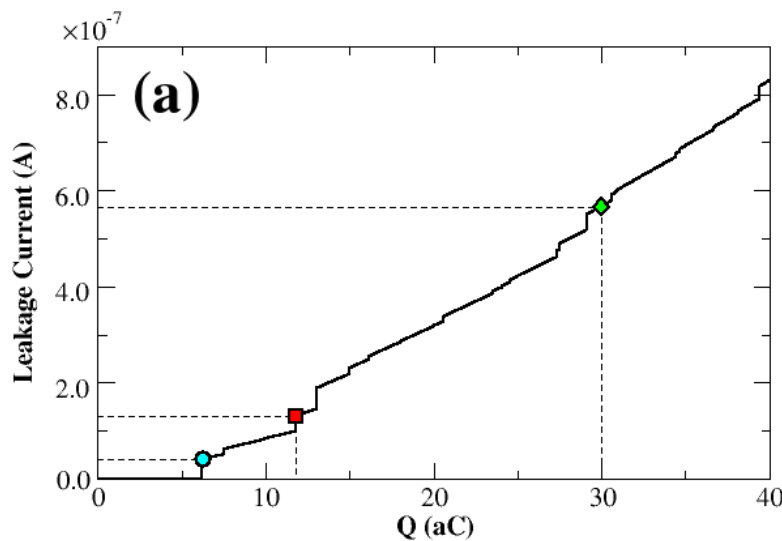


Figure 6.5: (a) Leakage current through the parallel RC circuit as a function of the charge accumulation of the capacitive NWN. Steep jumps in current levels are clear at certain charge values and correspond to sudden activations of capacitive junctions. (b) Visualisation of the network at the first set of junction activations at 6.22 aC and leakage current of $4.2 \times 10^{-8} \text{ A}$. Wires with an activated junction are in black and inactivated wires are in light grey. Figure (c) presents the activated wires when an electrical path between the electrodes is formed at $1.3 \times 10^{-7} \text{ A}$ and 11.78 aC . (d) Activated wires at a relatively high leakage current level at $5.7 \times 10^{-7} \text{ A}$ and 30 aC . Almost all junctions in the network underwent breakdown and the system is now MR at the HRS.

to NWNs where percolation has not occurred as a continuous line of junctions between electrodes are required to induce voltage differences across NWN junctions.

The dynamics of linear and sub-linear are different to the super-linear and are presented in Figure 6.6 for completeness. A smoother conductance curve is seen in Figure 6.6(a) for the linear exponent compared with the super-linear simulation. This is indicative of less selectivity in the emergence of low resistance paths which was shown by colour contour maps in chapter 5. Figure 6.6(b) shows activated junctions in blue at the point where the initial low resistance path is fully optimised. The same initial low resistance path that emerged in the supra-linear case is activated along with additional junction activations along a second low resistance path connecting the electrodes at the bottom of the network. Figure 6.4(c) represents the activated junctions at 30 u.c. in the linear exponent case and shows much less activated junctions than in the supra-linear simulation shown in Figure 6.4(c). The sub-linear exponent simulations result in the smoothest conductance curve out of the three and is shown in Figure 6.6(d). The low resistance path that emerges in the super-linear and linear case is evident in the sub-linear regime at path formation in Figure 6.6(e). Note that the required current flow for path formation is much higher (≈ 16 u.c.) compared with that needed in the linear (≈ 5.8 u.c.) and the supra-linear case (≈ 2 u.c.) due to the increasing dispersion of current through the network with decreasing exponent. The second low resistance path that is emerging in the linear case can also be seen and is much more developed than in the linear case with additional activated junctions in surrounding regions. This is a characteristic of sub-linear dynamics, where current flow is more distributed through the network. Figure 6.6(e) shows the fewest junctions activated at 30 u.c. compared to the linear and super-linear cases.

Qualitatively the regions that are activated in the CPM are also activated in the MRM, however the overlap between the two is not perfect. This non-perfect overlap is essentially a manifestation of the different activation processes, binary in the case of CPM and analogue for the MRM. The difference in activation patterns for path formation is a key contrast between the two models that have been applied to the exact same geometry and has been seen in all other networks that both MRM

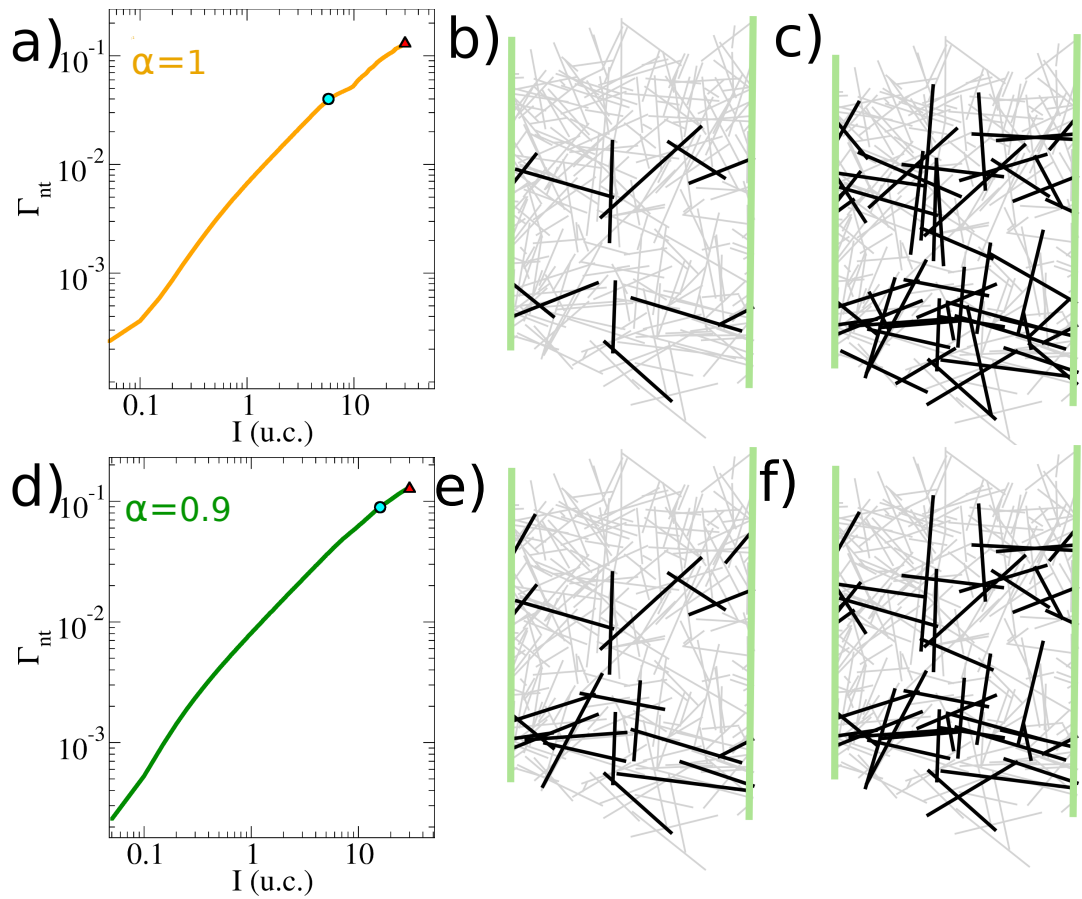


Figure 6.6: (a) $\Gamma_{nt} \times I$ curve for the network depicted in Figure 6.3 with a linear scaling exponent $\alpha_j = 1$. (b) The activated wires at the moment where the electrodes are bridged by a path of fully activated nanowire junctions. Note that this path lies in the center, the WTA path that emerged in the supra-linear simulation in Figure 6.4 and a second path has begun to emerge but is not fully activated at this point. (c) Activated wires at $I = 30$ u.c. occupy a large swath of the network, slightly less wires are activated here than in the supra-linear simulation Figure 6.4(c). (d) $\Gamma_{nt} \times I$ curve for the sub-linear simulation $\alpha_j = 0.9$. The activated wires at path formation are visualised in (d), a large amount of activations are required for a fully activated path to emerge. The activated wires at $I = 30$ u.c. are shown in (e), again there are less activated wires than in the linear case.

and CPM have been applied to. For a more quantitative comparison between the models, the amount of activated junctions (Φ) in all network diagrams appearing in Figure 6.4 & 6.6 and at path activation in the CPM, Figure 6.5(b), can be found in Figure 6.7. Note that the net difference $\Delta\Phi = \Phi(\text{PPL}) - \Phi(\text{PL})$ increases with respect to α_j , meaning that the higher exponent systems are more efficient at creat-

ing low resistance paths. But more importantly, this result captures the essence of the experimental observations presented in Figure 6.1(c-d); it contrasts the highly selective activation pattern of memristive (supra-linear) NWNs with the more assembled response obtained when the capacitive properties of these materials are probed. The number of activations needed for path formation in the CPM is much greater than the each of the MRM models pointing to the network wide participation of the CPM in path formation.

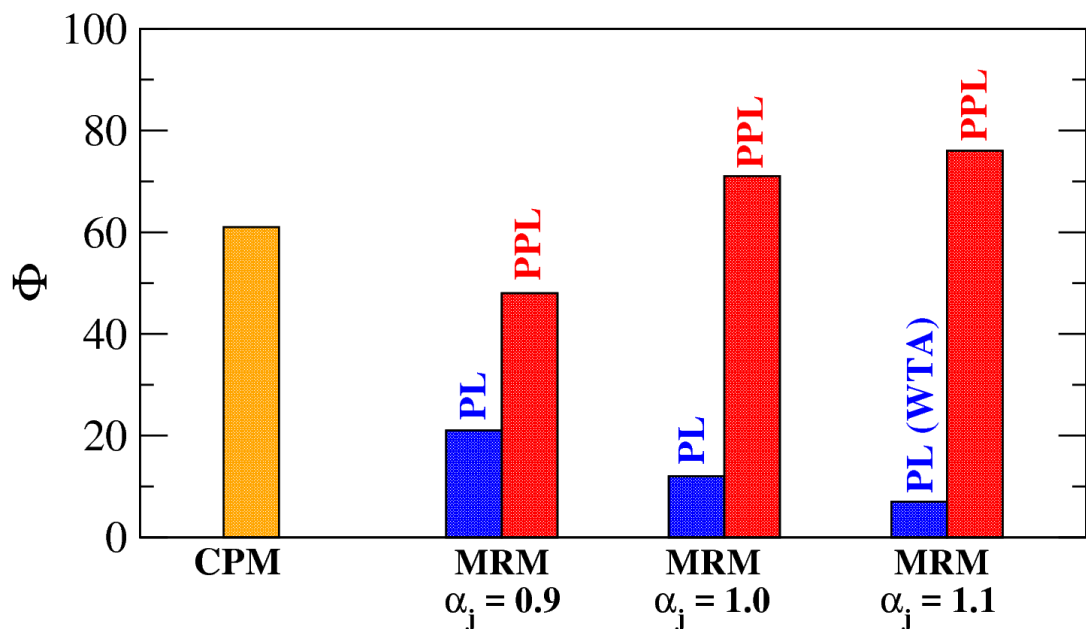


Figure 6.7: Number of activated junctions (Φ) predicted by the capacitive (CPM) and the memristive (MRM) descriptions. Note that an activated junction in the CPM picture corresponds to a capacitor having its state flipped as $|0\rangle \rightarrow |1\rangle$ whereas in the MRM picture it corresponds to a memristor reaching its most optimized conductive state with a resistance value of R_{on} . 61 capacitors were activated in order to create a shorting path between the electrodes. The activated junctions in the MRM is determined by those that reach their ultimate conductivity state at the moment of path formation (red) and at $I = 30\mu\text{A}$ (blue) for each of the distinct exponents α_j .

6.3 SCALE FREE DYNAMICS IN CAPACITIVE ACTIVATIONS

The sudden and large amount of junction activations, or avalanches, that give rise to the steps in leakage current flow in Figure 6.5(a) offer much insight into the scale-free response of NWNs in the CPM model. Of particular interest is the distribution in avalanche sizes and their respective relaxation times recorded during the CPM evolution (cf. Figure 6.8). The size of an avalanche (s) is defined as the number of junctions that break down at a given input charge Q . When at least one junction breaks down, the network self-organizes by redistributing its built-up charge throughout its remaining capacitive elements which can trigger subsequent avalanche events at the same charge input. The amount of iteration steps the network takes to relax its avalanche activity up to the point where $s = 0$ is defined as the avalanche lifetime or relaxation time (τ). Figure 6.8(a)&(b) are the normalised avalanche (f_s) and lifetime (f_τ) distributions taken for an ensemble containing 3000 randomly generated NWN samples of fixed wire density 0.4 NWs/ μm^2 and lengths 7 μm . Three difference network sizes are simulated to investigate if finite sized effects have an impact on the scaling of f_s and f_τ , 55 $\mu\text{m} \times 55 \mu\text{m}$ (blue diamonds), 60 $\mu\text{m} \times 60 \mu\text{m}$ (green squares), and 70 $\mu\text{m} \times 70 \mu\text{m}$ (orange triangles). One can observe that both distributions have a power-law trend which is indicative of scale-free critical behaviour, where a small perturbation can cause changes across the entire network ¹. Both power law trends are heavily affected by finite size effects caused by the closed boundaries of the device, f_s diverges from the power law for each of the network sizes. Yet, we can say that nanowire meshes operating in the capacitive mode exhibit a collective integrated response to electrical stimuli that is independent of the device size, i.e. the emerging collective dynamics of capacitive NWN systems is scale-invariant at least within certain

¹ Need to get a good citation for this

length scales. MRM dynamics do not give rise to scale-free network wide perturbations as current perturbations propagate through the network immediately and critical states do not occur.

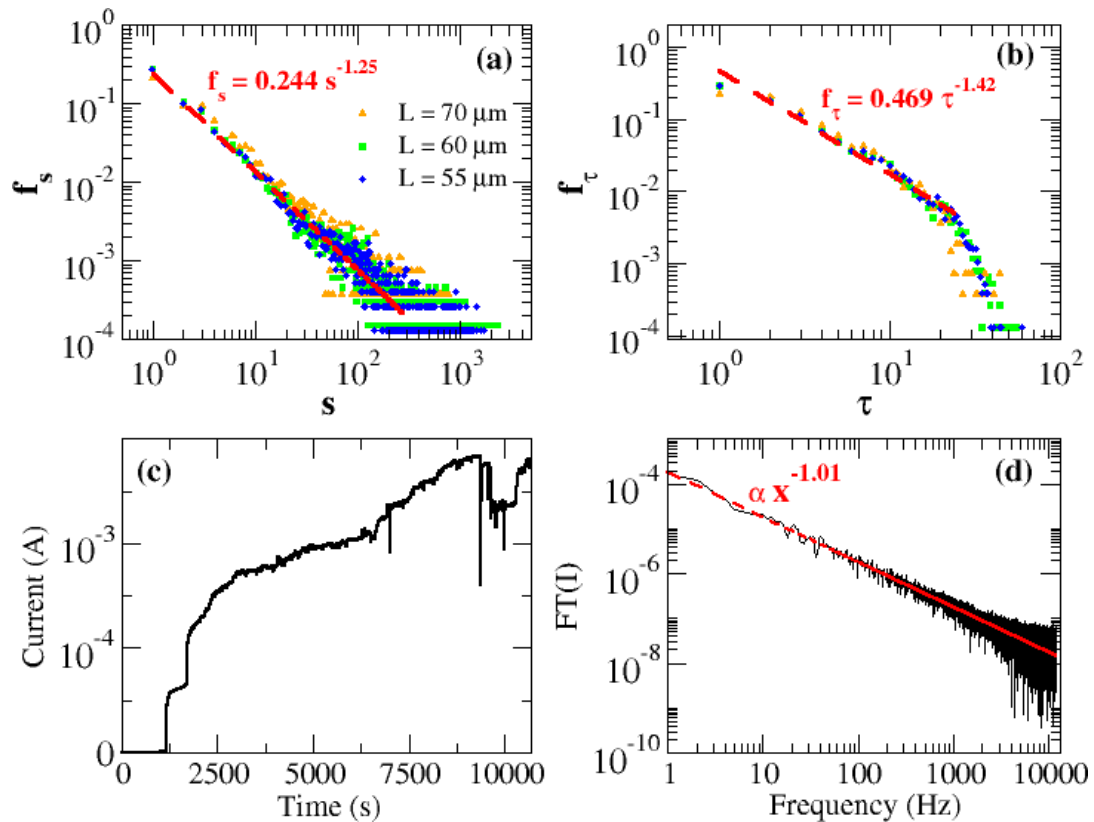


Figure 6.8: (a) Avalanche (s) and its respective (b) lifetime (τ) frequency distributions in log-log scale taken for a random NWN ensemble containing over 3000 network samples of fixed wire density of $0.4 \text{ NWs}/\mu\text{m}^2$ and distinct sizes of 55×55 , 60×60 , and $70 \times 70 \mu\text{m}$. Note that for this result to acquire statistical significance, it needs to be taken for a large ensemble of random NWN samples rather than applying CPM onto the solely image-processed NWN sample of Figure 6.3. The dashed lines are power law fittings that give exponents of $\beta_s = -1.25$ for the avalanche distribution sizes and $\beta_\tau = -1.42$ for the lifetime distribution. Finite size effects play an important role in cutting off the power law trend specially in the lifetime results. (c) Fourier transform (in log-log scale) of the time traces of DC current response shown on panel (d). The power-law fit gives a $1/f^\beta$ scaling with an exponent $\beta = 1.01$. (d) Time traces of current response (black curve) to 10.5 V DC bias measured in an Ag NWN sample of dimensions $1 \times 1 \text{ mm}$. The triangular bias sweep (red curve) shows the fine voltage range ($10.4998 - 10.5002 \text{ V}$) around 10.5 V - marked by the dashed grey line - that the network experiences for almost three hours.

In addition to the avalanche characterization provided by the computational model, experimental evidence of the collective dynamics of NWNs operating at minimal leakage currents was found, similar to works of Avizienis et al.¹⁰⁷ and Demis et al.¹⁰⁸. The experiment consists of measuring time traces of leakage current in a NWN sample experiencing a DC bias voltage for a large period of time. By performing a Fourier transform on the measured fluctuations in current, one can unveil complex emergent behaviours related to the activation process of the network and its recurrent connectivity structure. An Ag/PVP NWN of dimensions 1×1 mm was connected to a 10.5 V bias for 20 hours in total, recording the current throughout. Only the first three hours of current data is required to analyse the leakage-current response of the sample because, after three hours of measurement, sufficiently high currents levels were recorded indicating that the network had surpassed leakage conduction. These results are shown in Figure 6.8(c-d). The presence of a power-law trend in the power spectrum points to a network-wide activation that is scale-free with a $1/f^\beta$ noise scaling with $\beta = 1.01$. As argued by Avizienis et al.¹⁰⁷, such persistent current fluctuations at DC bias indicate the capacity of the network in avoiding the formation of a single dominant high-conductivity pathway between electrodes. This view agrees with the picture captured by our CPM (with a leakage term) of a scale-free clustering activation process in NWNs operating at a sufficiently low-current domain.

The CPM bears similarity to the circuit-breaker model developed by Chae et al in which the resistance of elements in a lattice switched resistance states instantaneously with an applied voltage crossing a certain threshold. Unlike the CPM model however the change in resistance was reversible, able to switch between high and low resistance states depending on its current state and the associated critical voltage. They too reported avalanche behaviour but did not report the power-law analysis such as that presented in Figures 6.8(a)&(b). This suggests that the scale free avalanche behaviour is a result of the binary nature of junctions and

will be a focus of future work as it has important implications to the neuromorphic computing capabilities of NWNs.

6.4 FAULT TOLERANCE

As so far demonstrated, disordered NWNs can exhibit scale-free capacitive activation or self-similar selective memristive dynamics depending on which current range the network is being probed. In particular, such MR random networks are very attractive for probing collective features that are typical of biological neural systems such as adaptability, parallel processing, and fault-tolerance capabilities. Contrary to regular patterned devices - such as crossbar arrays^{72,109} - where each unit has a singular role, computation in random memristive networks relies on the non-deterministic action of their nonlinear elements distributed in a highly disordered manner. The disordered and dynamical natures of these networks make them ideal candidates to probe novel fault-tolerant computing paradigms. In other words, the massively parallel processing power characteristic of disordered interconnects combined with the adaptability of their building-blocks enables self-organization, reconfiguration, and self-healing to mitigate device shortcomings¹¹⁰. To illustrate such robustness to variability in random memristive NWNs, the role played by defects on their conduction and capacitive response is presented in this section.

A defect is made on a network composed of supra-linear junctions exhibiting WTA conduction by the removal of a junction from this key path before any current is applied to the network and junction evolution begins. This is a striking perturbation to consider since in principle it can destroy the current flow through the most important network path. MRM simulations were carried out to monitor the network conductance as a function of current for the defective system and compared with the original $\Gamma_{nt} \times I$ curve shown in Figure 6.4(a). Figure 6.9(b) is a

visualisation of the WTA path in the unperturbed network, identical to that shown in Figure 6.4(b). Figure 6.9(c) represents the new WTA path that is formed in the perturbed network with the destroyed junction represented by the red star. The conductance evolution for both original and defective NWN is almost identical at least until the first stages of the PPL regime as shown in Figure 6.9(c). The self-healing properties embedded in the dynamics of memristive NWNs are clear in this example; the disruption of paths forces the junctions to re-adapt and this causes a redistribution of current across the network frame. The system then reconfigures into another least-resistance-path that does not adversely impact its overall conductance using hence just a little extra power to stress this second WTA path.

A second type of junction failure was also simulated where the network evolves unperturbed until the formation of the WTA path and at a point in the first plateau the junction ‘fails’ and is removed from the Kirchhoff matrix. When the junction fails, the magnitude of the applied current will not alter but the current flow through the network will dramatically reorder itself. Associated with this re-ordering the conductance of each junction will be allowed to either decay to a value given by $\Gamma_{jxn} = A_j I_j^{\alpha_j}$ representing a fast decay of the memristive junctions or it will not, representing a system with very slow or no decay of the memristive state. Figure 6.10(a) presents the $\Gamma_{nt} \times I$ curves for the system with a fast memristive junction. The black dashed line represented the conductance curve of the original NWN, i.e. with no defect. The red line is the conductance curve of the defective Nw. The dramatic spike downwards in conductance seen at $I = 2$ u.c. corresponds to the point at which the defective junction failed. Immediately after the spike the conductance recovers to a value just below that before the junction failure. The conductance oscillates around a steady state until $I \approx 2.7$ u.c. where there is a spike in conductance. The rise and subsequent fall in conductance corresponds to the gradual reduction in current flow through the junctions in the original WTA, reducing theirs and the sheets conductance. A visualization of the Nw at $I = 3$ u.c presents the activated junctions and the wires involved in the new WTA path.

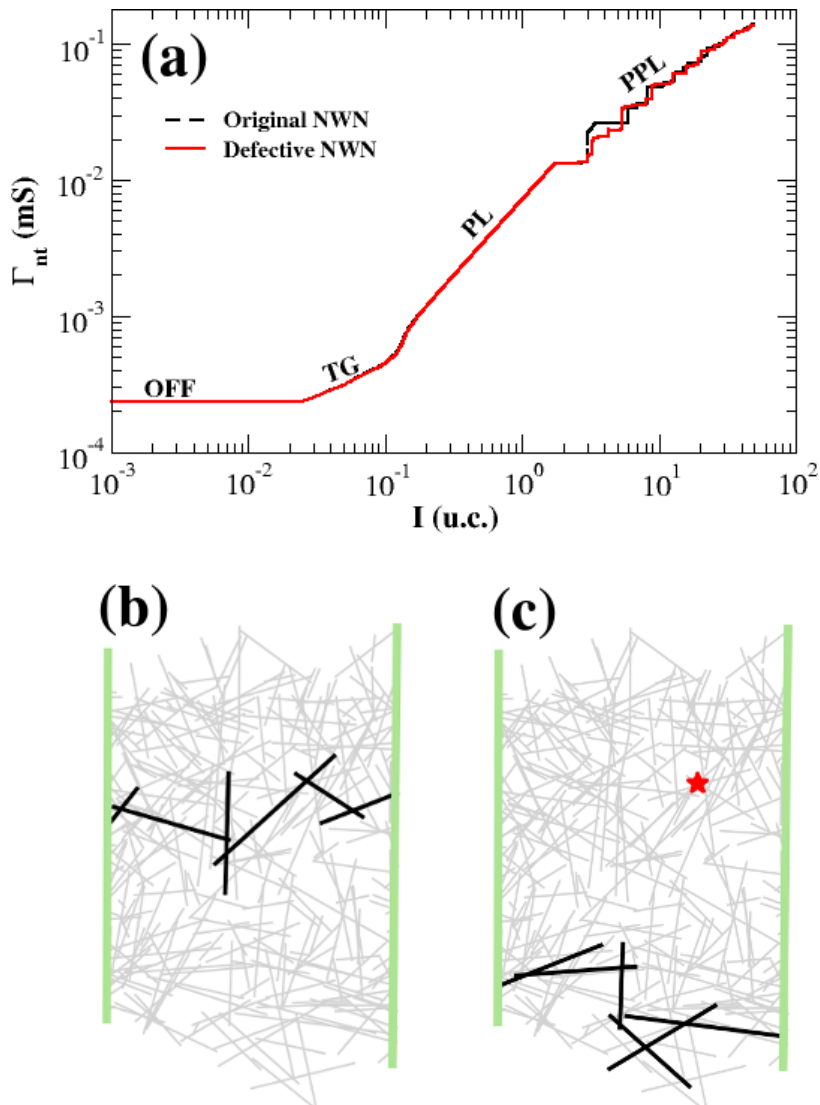


Figure 6.9: (a) $\Gamma_{nt} \times I$ curves obtained for the original (black dashed line) and the defective network (red line). The junction characteristics in these simulations are $\alpha_j = 1.1$ and $A_j = 0.05$. The curves only differ at the PPL regime. (b) Network diagram depicting wires in the WTA (black sticks) at $I = 1.77$ u.c. obtained using MRM in the original NWN. (c) A junction in this path was deleted and it is highlighted by a red star symbol. The network self-organizes the current transmission to another WTA path located at its bottom part. This path contains the same amount of junctions as in the original network, i.e. 7 junctions. Wires carrying residual or no current at all appear in light grey. Vertical green lines represent the electrodes that source current onto the network.

A shift in the WTA path away from the original is clear, with no junctions in the original WTA remaining activated.

Figure 6.10(c) presents the conductance curve of the faulty network where no decay in junction conductance occurs in the original WTA junctions apart from the failed junction. Again an immediate spike downwards is seen after junction failure at $I = 2$ u.c and current flow is redistributed through the NWN. Incredibly, the conductance of the NWN actually increases beyond its conductance prior to junction failure. This may due be to the development of new junctions joining the original WTA and a second WTA path emerging. The conductance then increases at a steady rate afterwards towards the second plateau. Interestingly in the visualisation of the activated junctions in at $I = 3$ u.c. there are no additional junctions activated compared meaning that a new WTA has not fully developed yet. This means that the the majority of current is still being funneled through the remnants of the original WTA path and then bleeding into the undeveloped network surrounding it when it reaches the failed junction. Both junction failure simulations show that there is an abrupt redistribution of current-flow through a NWN where a junction in the WTA fails soon after its formation. The abrupt redistribution of current-flow when a junction fails under a current load a clear indication of the potential fault tolerance of a NWN. The conduction levels return to near the unperturbed systems levels and their subsequent evolution is much in line with the pristine networks.

It should be noted that here the memristive model is meant to capture the gradual increase in conductance levels associated with a gradual increase in sourced current on the network. The sudden junction failures presented in Figure 6.10 cause a sudden redistribution of current flow that may not be properly captured by the MRM. Future investigation of the of the fault-tolerance of memrsitive networks will require the implementation of a modeling scheme that accounts for the materials response to large current flow changes at an atomistic level.

In the capacitive regime it was demonstrated that small perturbations can have a significant effect on the network dynamics as depicted in Figure 6.8(a-b). Here the network is perturbed by deleting a key junction that is involved in forming the

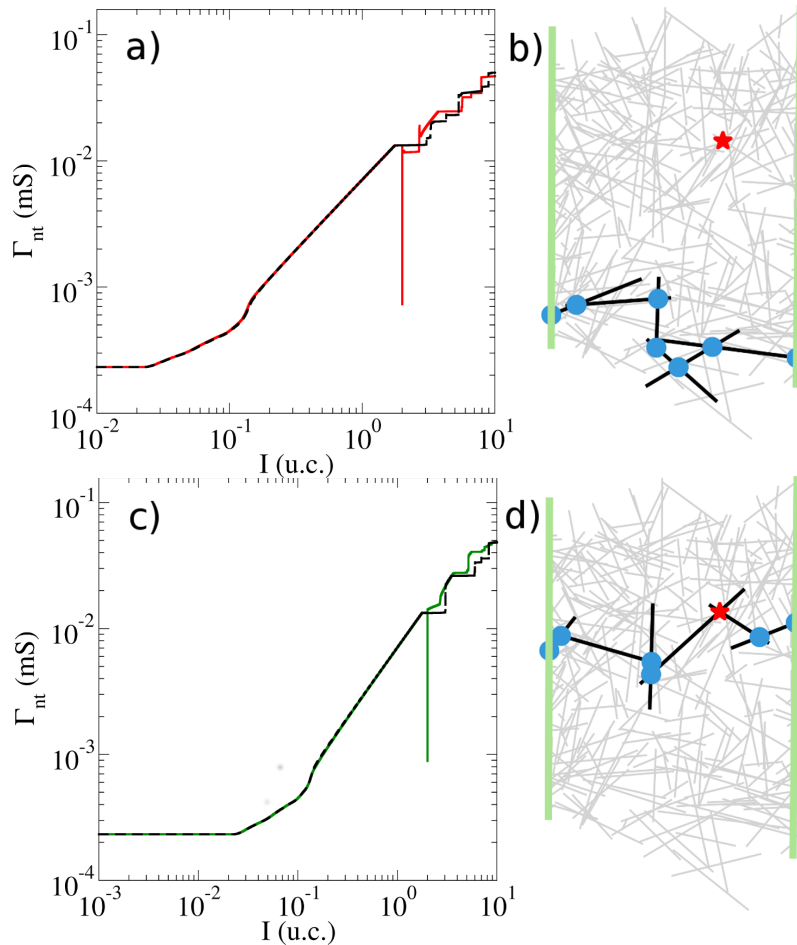


Figure 6.10: (a) $\Gamma_{nt} \times I$ curves obtained for the original (black dashed line) and the defective network (red line) where the defect was introduced during the first plateau and junction conductances are allowed to decay. (b) Network diagram depicting activated junctions at $I = 3$ u.c. with junction conductance decay. The defective junction is represented by a red star, activated junctions are blue dots and wires with activated junctions on them are in Black. (c) $\Gamma_{nt} \times I$ curves obtained for the original (black dashed line) and the defective network (red line) where the defect was introduced during the first plateau and junction conductances cannot decay. (d) Network diagram depicting activated junctions at $I = 3$ u.c. with junction conductance decay. The defective junction is represented by a red star, activated junctions are blue dots and wires with activated junctions on them are in black. When junction conductances cannot decay no shift in WTA takes place.
 NOTE: REMOVE BLUE JUNCTION CIRCLES?

path between electrodes in the CPM model before any charge has begun accumulating on the electrodes. In Figure 6.11(a) the unperturbed network is presented when the leakage path between electrodes has been formed for the first time and

this occurs at the charge of 11.77 aC. Figure 6.11(b) shows the activated wires at the moment of path formation for the perturbed network with one of its crucial junctions being destroyed from the start of the simulation (represented by the red star). This junction plays a pivotal role in the dynamics of path formation in the capacitive network which is evident when we compute the number of activated wires for both pristine and perturbed cases. The unperturbed network activates 61 wires and junctions whereas the defective one mobilizes 95 wires and 126 junctions, an increase of 56% of activated wires and over 100% for junctions with respect to the benchmark pristine system. The charge required to form the electrode-electrode path also points to the sensitivity of the network to perturbations: 13.05 aC for the defective NWN compared with 11.77 aC for the unperturbed one.

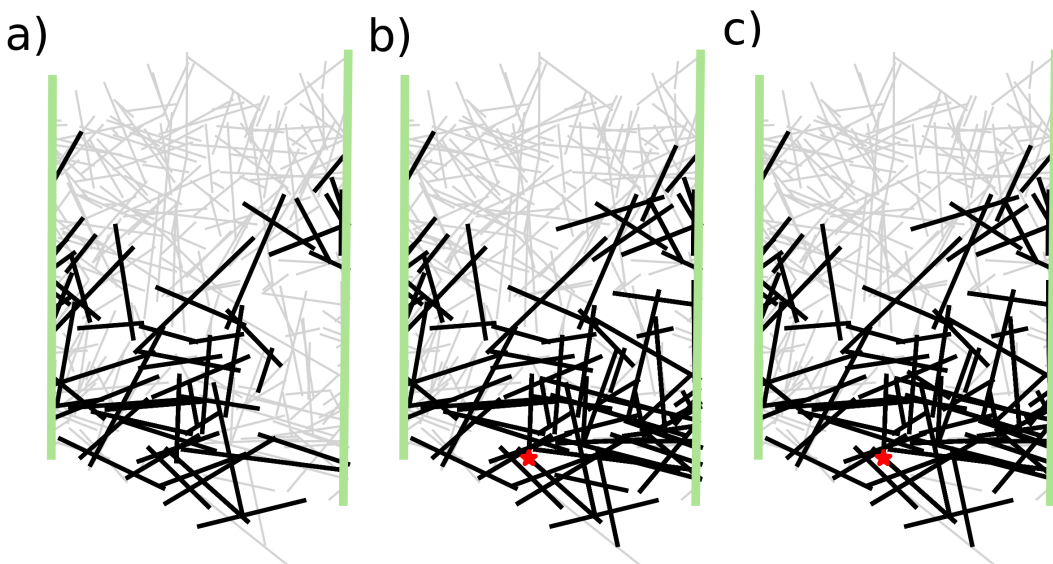


Figure 6.11: (a) Network diagram depicting activated wires (black sticks) in the original NWN described as a capacitive system via CPM. The simulation ends when a continuous path of grounded wires is formed between the electrodes. 61 junctions and wires are activated in this simulation. (b) The same activation simulation as in (a) but with a defective junction marked with a red star symbol. The defective junction does not play any role in the simulation as it is a failed junction from the start. The simulation ends when a path is formed between electrodes, requiring 126 junction activations or 95 wire activations. (c) The same activation simulation as in (a) but with a defective junction that fails immediately after path formation. 124 junction activations or 95 wire activations occur for path reformation.

A second failure method that was simulated was the failure of a key junction immediately after a continuous path is formed for the first time. The same junction as that failed in 6.11(b) was taken as the failure point. The junction was chosen to fail at $Q = 11.77$ a.c, the same point at which a path is formed in the pristine NWN. The junction is then removed from the Kirchoff matrix but both wires remain activated and the simulation continues until a new path is formed between the two electrodes. Here the path reforms at 12.06 u.c, less than that required for the network in 6.11(b). Again 95 wires are activated in this network but there are 124 junctions activated, two less than in the case of the prior junction failure. A visualisation of the activated wires is shown in ??(c) and looks very similar to panel (b). There is however a slight difference between the two, with one wire in each case not activated in the other.

The fact that both failure mechanisms provide very similar activation behaviours may be due to the fact that the CPM is a network wide activation procedure, unlike the MRM. Contrasting the fault-tolerant results captured by CPM and MRM, one can conclude that the CPM shows a greater sensitivity to network geometry and connectivity profile. Perturbations to the connectivity profile results in wildly different activation patterns in the NWN and destruction of key junctions involved in path formation results in a large increase in the required junction activations and acquired electrode charge. The MRM however is much more robust; while the WTA path may completely re-route when a fault is encountered it does so in an efficient manner with little change in the global conductance of the network.

6.5 CONCLUSION

In this chapter a model that describes nanowire junctions as a binary state capacitor that transitions to an activated state once a critical potential difference across the junction was introduced in section 6.1. A computational routine to apply the

capacitive model to a nanowire network with an incrementally increasing applied voltage was described in section 6.1. In this chapter the path formation dynamics, scale-free response to network perturbations, and the fault-tolerance of the CPM was compared with the MRM that was introduced in the previous chapter.

In section 6.2 path formation in the capacitive model was compared with that of the memristive junction model. The two successfully model the leakage capacitive and memristive responses of NWNs perturbed at distinct transport regimes, the capacitive to extremely low current levels (\sim pA) and the memristive to currents in the range \sim nA- μ A. By applying both models to an identical network geometry the contrasting dynamics of both models were highlighted. The MRM was previously shown to develop highly selective current flow paths in a winner-takes-all manner for certain junction parameters. The CPM on the other hand displayed a network wide activation pattern before a continuous path of activated junctions existed between electrodes. Not only were the activation patterns different between the two, the emergent paths between electrodes were located in entirely different areas of the network.

The CPM was shown to move between periods of idleness to abrupt cascades of mass activations of junctions in the network as the potential difference across the device was increased in section 6.3. The size frequency distribution of these activation events, or avalanches of activations, were shown to follow a power-law relationship which is indicative of scale-free complex network dynamics, i.e. the effect of perturbations to the network is only limited by the size of the network. Experimental evidence for the complex dynamics of a physical nanowire network with negligible current flow was presented and corroborates the scale-free nature of the CPM in simulations.

The fault-tolerance of the CPM and MRM models were shown through demonstrating the response of network to a junction failure in the main inter-electrode path in section 6.4. In the MRM two types of failures were simulated. First a key junction in the WTA was destroyed before any current was sourced on the network

and the current level and sheet conductance required to achieve a new WTA path were observed. It was found that only a slight drop in sheet conductance occurred at the formation of a WTA and a negligible increase in required current was observed in the perturbed network. A second failure simulation saw a key junction in the WTA path fail when the network had already achieved a WTA path, while continuing to increase the current sourced through the network. Two junction responses to the redistribution of current through the NWN were simulated, either the junction's conductance state was allowed to decay to a lower conductance value or it was not allowed to decay but only increase with increasing current levels. In both simulations the network experienced a large and sudden drop in conductivity but quickly recovered as a new WTA was formed. Where junction conductivities were able to decay the networks conductivity recovered to a level just below the unperturbed network's. The simulation with irreversible conductive states saw that of the networks actually increase after the failure. This highlights the robustness of massively parallel memristive networks in the MRM regime.

The sensitivity of the CPM to junction faults was also presented in section 6.4, with two junction failure types similar to those examined for the MRM. Again a key junction in the formation of the shorting path in the CPM was destroyed from the beginning of the simulation and the number of activation processes required was recorded. In this particular example 126 junctions were activated at the formation of the shortening path compared with the 61 activations that occurred in the unperturbed network. The second junction failure simulation saw the same key junction fail once the shortening path between electrodes formed. Here the path reformation occurred with 124 junction activations, two less than the network perturbed from the start of the simulation. The CPM required more than double the junction activations to reform a shorting path between the electrodes showing that junction failure in the CPM has a large effect in the capacitive properties of a network compared to the response of the memristive model where failures had a minor effect on the network conductivity.

A

DIGITISED NETWORK PARAMETERS

The calculated parameters for thirty experimental samples of Ag/PVP nanowire networks are listed in Table A.1. The wire density (n_w) was obtained by digitising SEM images of the physical sample as described in chapter 3, the experimental sheet resistance was physically determined and listed under R_s^{EXP} , and the remaining parameters were obtained through applying JDA and MNR simulations to the digitised network geometry as outlined in chapter 3. The contribution of inner-wire resistances to the network resistance was isolated in simulations and listed under R_0 . The contribution of junction resistances to that of the network is captured by $\Delta = R_s^{\text{EXP}} - R_0$. The slope of the linear relationship between junction resistance and sheet resistance outlined in equations 3.2.1 and 3.2.2. The characteristic MNR junction resistance $R_j^{\text{MNR}} = \Delta/a$ and the characteristic JDA junction resistance $R_j^{\text{JDA}} = R_s^{\text{EXP}}/a$ represent the simulated junction resistance to achieve the measured sheet resistance for each sample. The optimization-capacity coefficient (γ) for each sample is also listed. See section 3.3 for a further discussion of the listed parameters.

Network	n_w	R_s^{EXP}	R_0	Δ	α	R_j^{MNR}	R_j^{JDA}	γ
1	0.28	84.42	46.43	37.99	1.37	27.73	61.62	0.45
2	0.16	159.95	92.05	67.9	2.47	27.52	64.83	0.42
3	0.16	177.14	60.99	116.15	1.93	60.07	91.61	0.65
4	0.49	18.8	12.86	5.94	0.44	13.38	42.35	0.31
5	0.64	23.77	12.09	11.67	0.27	43.39	88.38	0.49
6	0.35	180.5	32.91	147.58	0.97	152	185.91	0.82
7	0.63	14.85	8.9	5.94	0.17	35.03	87.58	0.4
8	0.47	29.89	9.3	11.58	0.22	52.52	135.56	0.55
9	0.17	56.2	37.9	18.28	1.20	15.28	46.98	0.32
10	0.39	67.27	32.85	34.42	1.01	33.96	66.37	0.51
11	0.2	233.15	71.42	161.72	2.31	69.89	100.76	0.69
12	0.57	51.06	20.93	30.13	0.59	51.01	86.44	0.59
13	0.17	220.54	52.14	168.4	1.34	125.88	164.85	0.76
14	0.37	33.98	22.03	11.95	0.53	22.71	64.58	0.35
15	0.14	194.33	77.15	117.18	1.90	61.57	102.11	0.6
16	0.26	54.54	26.39	28.14	0.73	38.33	74.29	0.51
17	0.24	50.38	28.18	22.2	0.83	26.6	60.37	0.44
18	0.12	109.12	42.7	66.42	0.98	67.47	110.85	0.61
19	0.21	61.88	58.68	3.19	1.40	2.28	44.23	0.05
20	0.29	42.15	20.78	21.36	0.56	38.28	75.54	0.51
21	0.28	54.17	35.44	18.73	0.80	23.33	67.47	0.34
22	0.14	103.62	70.48	33.14	2.10	15.76	49.28	0.32
23	0.35	34.65	21.97	12.68	0.42	29.92	81.76	0.36
24	0.29	41.49	19.19	22.3	0.51	43.68	81.27	0.54
25	0.37	58.31	19.81	38.5	0.68	56.78	86.00	0.66
26	0.36	42.93	17.68	25.24	0.48	53.03	90.20	0.59
27	0.43	39.33	16.23	23.1	0.48	48.18	82.03	0.59
28	0.35	56.12	32.02	24.1	1.10	21.92	51.04	0.43
29	0.19	188.04	66.52	121.52	2.35	51.75	80.08	0.65
30	0.22	76.68	38.04	38.64	1.00	38.54	76.48	0.5

Table A.1

B

MULTI-NODAL ELECTRODES IN A SQUARE LATTICE

¹ In this section the Inter-nodal Resistance Green's Function is generalised to a system with extended electrodes and where lattice is infinite in the \vec{a}_1 direction but finite in the \vec{a}_2 direction. The width of the system in this direction is N_y nodes. The injection electrode is represented by a strip of nodes at positions $\vec{r}_{in} = x_{in}\vec{a}_1 + m\vec{a}_2$, $0 \leq m < N_y$. Similarly the extraction electrode is represented by a strip of nodes at positions $\vec{r}_{out} = x_{out}\vec{a}_1 + n\vec{a}_2$, $0 \leq n < N_y$. In order to simplify notation, let $x_{in} = 0$ and $x_{out} = N_x$. The number of nodes in each electrode (or the width of the electrode) is N_y nodes, the same as the width of the system. See Fig.?? for a schematic of the system.

Following the derivation for the Inter-nodal Green's Function, one begins by describing the current at lattice point \vec{r} . A total current I is injected at one of the electrode with a current $i_0 = \frac{I}{N_y}$ injected at each of the nodes in this injection electrode. Consider a current i_0 is injected at position $(0, m)$ and i_0 is extracted from the entire extraction electrode. We define the current extracted at each individual node (N_x, n) as i_{mn} . In other words i_{mn} is the current extracted from the node at position (N_x, n) when a current i_0 is injected at node $(0, m)$. We make the assumption that a current of i_0 is extracted from each node in the extraction electrode

¹ This section needs to be adjusted and properly linked in with chapter 4. May not include it

when a total current I is injected into the injection electrode. The total extracted current must match the injected current and so

$$\sum_{n=0}^{N_y-1} i_{mn} = \sum_{m=0}^{N_y-1} i_{mn} = i_0 \quad (\text{B.o.1})$$

The current equation in this case of a single injection node and multiple extraction nodes is

$$I(\vec{r}) = I(x\vec{a}_1 + y\vec{a}_2) = \delta(x)\delta(y-m)i_0 - \sum_{n=0}^{N_y-1} \delta(x-N_x)\delta(y-n)i_{mn} \quad (\text{B.o.2})$$

By summing contributions of current i_0 injected at each point $(0, m)$ on the injection electrode, one can write the current equation of a system with two electrodes of width N_y nodes separated by N_x nodes as

$$I(\vec{r}) = I(x\vec{a}_1 + y\vec{a}_2) = \sum_{m=0}^{N_y-1} \left(\delta(x)\delta(y-m)i_0 - \sum_{n=0}^{N_y-1} \delta(x-N_x)\delta(y-n)i_{mn} \right) \quad (\text{B.o.3})$$

The voltage function from Eq.(??) is now:

$$V(\vec{r}) = R \sum_{m=0}^{N_y-1} \left(G(\vec{r} - m\vec{a}_2)i_0 - \sum_{n=0}^{N_y-1} G(\vec{r} - N_x\vec{a}_1 - n\vec{a}_2)i_{mn} \right) \quad (\text{B.o.4})$$

In order to calculate the resistance between the two electrodes, we calculate the difference between the average voltage on the electrode where current is injected and the average voltage on the electrode where current is extracted. We then divide by the total amount of current that was injected/extracted.

$$R_e(N_x) = \frac{1}{N_y I} \left(\sum_{b=0}^{N_y-1} V(0, b) - \sum_{b=0}^{N_y-1} V(N_x, b) \right) \quad (\text{B.o.5})$$

Consider finite electrodes in one of two systems. If the network is infinite in both \vec{a}_i directions then one performs a continuous Fourier transform in both \vec{k} directions for the greens function G_i .

$$G_i(\vec{r} = x\vec{a}_1 + y\vec{a}_2) = \int \frac{dk_1}{2\pi} \frac{dk_2}{2\pi} \frac{e^{i(k_1 x + k_2 y)}}{2 - \cos(k_1) - \cos(k_2)} \quad (\text{B.o.6})$$

The

Due to the finite size of the network in the \vec{a}_2 direction, k_2 is discretised with values $k_2 = \frac{b}{N_y}$, $b = 0, 1, \dots, N_y - 1$. The discrete Fourier transform and its inverse has been used in this direction.

$$G(\vec{r} = x\vec{a}_1 + y\vec{a}_2) = \frac{1}{N_y} \sum_{b=0}^{N_y-1} \int \frac{dk_1}{2\pi} \frac{e^{i(k_1 x + \frac{2\pi b}{N_y} y)}}{2 - \cos(k_1) - \cos(\frac{2\pi b}{N_y})} \quad (\text{B.o.7})$$

Using the fact that $i_0 = I/N_y$ one can write the resistance equation as:

$$R_e(N_x, N_y) = R \int \frac{dk_1}{2\pi} \sum_{b,l,m=0}^{N_y-1} \frac{1}{N_y^3} e^{\frac{i2\pi bm}{N_y}} e^{\frac{-i2\pi bl}{N_y}} \left(\frac{1 - e^{ik_1 N_x}}{2 - \cos(k_1) - \cos(\frac{2\pi b}{N_y})} \right) \quad (\text{B.o.8})$$

One can single out a dirac-delta function using an inverse discrete fourier transform

$$\frac{1}{N_y} \sum_{m=0}^{N_y} e^{\frac{i2\pi bm}{N_y}} = \delta(b) \quad (\text{B.o.9})$$

Subbing this in and summing over b

$$R_e(N_x, N_y) = R \int \frac{dk_1}{2\pi} \sum_{l=0}^{N_y-1} \frac{1}{N_y^2} \left(\frac{1 - e^{ik_1 N_x}}{1 - \cos(k_1)} \right) \quad (\text{B.o.10})$$

The remaining integral can be performed using the residue theorem leaving us with

$$R_e(N_x, N_y) = R \frac{N_x}{N_y} \quad (\text{B.o.11})$$

This seemingly complicated derivation has a straightforward interpretation. Consider chains of N_x resistors of resistance R connected in series, and there are N_y of these chains connected in parallel.

The dependence of R_e on N_x and N_y are explored using computational simulations in Figure ???. Figure ?? a) presents the effect of changing the lead separation in a square lattice where $N_y = 30$ and each resistor in the network $R = 1\Omega$. A clear linear relationship is evident between the two matching the analytical expression outlined in Equation B.0.11. Figure ?? b) presents the effect of changing N_y with $N_x = 30$ and fixed resistance $R = 1\Omega$.

BIBLIOGRAPHY

- [1] A. P. Alivisatos, "Semiconductor clusters, nanocrystals, and quantum dots," *science*, vol. 271, no. 5251, pp. 933–937, 1996.
- [2] R. Adelung, L. Kipp, J. Brandt, L. Tarcak, M. Traving, C. Kreis, and M. Skibowski, "Nanowire networks on perfectly flat surfaces," *Applied physics letters*, vol. 74, no. 20, pp. 3053–3055, 1999.
- [3] S. Iijima, "Helical microtubules of graphitic carbon," *nature*, vol. 354, no. 6348, p. 56, 1991.
- [4] K. S. Novoselov, A. K. Geim, S. V. Morozov, D. Jiang, Y. Zhang, S. V. Dubonos, I. V. Grigorieva, and A. A. Firsov, "Electric field effect in atomically thin carbon films," *science*, vol. 306, no. 5696, pp. 666–669, 2004.
- [5] K. F. Mak, C. Lee, J. Hone, J. Shan, and T. F. Heinz, "Atomically thin mos₂: a new direct-gap semiconductor," *Physical review letters*, vol. 105, no. 13, p. 136805, 2010.
- [6] J. Jadwiszczak, C. O'Callaghan, Y. Zhou, D. S. Fox, E. Weitz, D. Keane, C. P. Cullen, I. O'Reilly, C. Downing, A. Shmeliiov, *et al.*, "Oxide-mediated recovery of field-effect mobility in plasma-treated mos₂," *Science advances*, vol. 4, no. 3, p. eaao5031, 2018.
- [7] A. R. Rathmell, S. M. Bergin, Y.-L. Hua, Z.-Y. Li, and B. J. Wiley, "The growth mechanism of copper nanowires and their properties in flexible, transparent conducting films," *Advanced materials*, vol. 22, no. 32, pp. 3558–3563, 2010.

- [8] Y. Chen, Z. Ouyang, M. Gu, and W. Cheng, "Mechanically strong, optically transparent, giant metal superlattice nanomembranes from ultrathin gold nanowires," *Advanced Materials*, vol. 25, no. 1, pp. 80–85, 2013.
- [9] S. De, T. M. Higgins, P. E. Lyons, E. M. Doherty, P. N. Nirmalraj, W. J. Blau, J. J. Boland, and J. N. Coleman, "Silver nanowire networks as flexible, transparent, conducting films: extremely high dc to optical conductivity ratios," *ACS nano*, vol. 3, no. 7, pp. 1767–1774, 2009.
- [10] Y. Wu, H. Yan, M. Huang, B. Messer, J. H. Song, and P. Yang, "Inorganic semiconductor nanowires: rational growth, assembly, and novel properties," *Chemistry—A European Journal*, vol. 8, no. 6, pp. 1260–1268, 2002.
- [11] C. Aguirre, S. Auvray, S. Pigeon, R. Izquierdo, P. Desjardins, and R. Martel, "Carbon nanotube sheets as electrodes in organic light-emitting diodes," *Applied Physics Letters*, vol. 88, no. 18, p. 183104, 2006.
- [12] D. Hecht, L. Hu, and G. Grüner, "Conductivity scaling with bundle length and diameter in single walled carbon nanotube networks," *Applied Physics Letters*, vol. 89, no. 13, p. 133112, 2006.
- [13] R. C. Tenent, T. M. Barnes, J. D. Bergeson, A. J. Ferguson, B. To, L. M. Gedvilas, M. J. Heben, and J. L. Blackburn, "Ultrasmooth, large-area, high-uniformity, conductive transparent single-walled-carbon-nanotube films for photovoltaics produced by ultrasonic spraying," *Advanced Materials*, vol. 21, no. 31, pp. 3210–3216, 2009.
- [14] Y. Lu and K. Chou, "Tailoring of silver wires and their performance as transparent conductive coatings," *Nanotechnology*, vol. 21, no. 21, p. 215707, 2010.
- [15] V. Scardaci, R. Coull, P. E. Lyons, D. Rickard, and J. N. Coleman, "Spray deposition of highly transparent, low-resistance networks of silver nanowires over large areas," *Small*, vol. 7, no. 18, pp. 2621–2628, 2011.

- [16] E. M. Doherty, S. De, P. E. Lyons, A. Shmeliov, P. N. Nirmalraj, V. Scardaci, J. Joimel, W. J. Blau, J. J. Boland, and J. N. Coleman, "The spatial uniformity and electromechanical stability of transparent, conductive films of single walled nanotubes," *Carbon*, vol. 47, no. 10, pp. 2466–2473, 2009.
- [17] D. Leem, A. Edwards, M. Faist, J. Nelson, D. D. C. Bradley, and J. C. de Mello, "Efficient organic solar cells with solution-processed silver nanowire electrodes," *Advanced Materials*, vol. 23, no. 38, 2011.
- [18] C.-H. Liu and X. Yu, "Silver nanowire-based transparent, flexible, and conductive thin film," *Nanoscale research letters*, vol. 6, no. 1, p. 75, 2011.
- [19] D. J. Finn, M. Lotya, and J. N. Coleman, "Inkjet printing of silver nanowire networks," *ACS applied materials & interfaces*, vol. 7, no. 17, pp. 9254–9261, 2015.
- [20] D.-J. Kim, H.-I. Shin, E.-H. Ko, K.-H. Kim, T.-W. Kim, and H.-K. Kim, "Roll-to-roll slot-die coating of 400 mm wide, flexible, transparent ag nanowire films for flexible touch screen panels," *Scientific reports*, vol. 6, p. 34322, 2016.
- [21] D. Langley, G. Giusti, C. Mayousse, C. Celle, D. Bellet, and J.-P. Simonato, "Flexible transparent conductive materials based on silver nanowire networks: areview," *Nanotechnology*, vol. 24, no. 45, p. 452001, 2013.
- [22] A. Kumar and C. Zhou, "The race to replace tin-doped indium oxide: which material will win?," *ACS nano*, vol. 4, no. 1, pp. 11–14, 2010.
- [23] D. P. Langley, M. Lagrange, G. Giusti, C. Jimenez, Y. Brechet, N. D. Nguyen, and D. Bellet, "Metallic nanowire networks: effects of thermal annealing on electrical resistance," *Nanoscale*, vol. 6, pp. 13535–13543, 2014.
- [24] M. Song, D. S. You, K. Lim, S. Park, S. Jung, C. S. Kim, D.-H. Kim, D.-G. Kim, J.-K. Kim, J. Park, Y.-C. Kang, J. Heo, S.-H. Jin, J. H. Park, and J.-W. Kang, "Highly efficient and bendable organic solar cells with solution-processed

- silver nanowire electrodes," *Advanced Functional Materials*, vol. 23, no. 34, pp. 4177–4184, 2013.
- [25] M. Lagrange, D. Langley, G. Giusti, C. Jiménez, Y. Bréchet, and D. Bellet, "Optimization of silver nanowire-based transparent electrodes: effects of density, size and thermal annealing," *Nanoscale*, vol. 7, no. 41, pp. 17410–17423, 2015.
- [26] P.-C. Hsu, S. Wang, H. Wu, V. K. Narasimhan, D. Kong, H. R. Lee, and Y. Cui, "Performance enhancement of metal nanowire transparent conducting electrodes by mesoscale metal wires," *Nature communications*, vol. 4, p. 2522, 2013.
- [27] D. Bellet, M. Lagrange, T. Sannicolo, S. Aghazadehchors, V. H. Nguyen, D. P. Langley, D. Muñoz-Rojas, C. Jiménez, Y. Bréchet, and N. D. Nguyen, "Transparent electrodes based on silver nanowire networks: From physical considerations towards device integration," *Materials*, vol. 10, no. 6, p. 570, 2017.
- [28] S. Gong and W. Cheng, "One-dimensional nanomaterials for soft electronics," *Advanced Electronic Materials*, vol. 3, no. 3, p. 1600314, 2017.
- [29] X.-Y. Zeng, Q.-K. Zhang, R.-M. Yu, and C.-Z. Lu, "A new transparent conductor: silver nanowire film buried at the surface of a transparent polymer," *Advanced Materials*, vol. 22, no. 40, pp. 4484–4488, 2010.
- [30] Z. Yu, Q. Zhang, L. Li, Q. Chen, X. Niu, J. Liu, and Q. Pei, "Highly flexible silver nanowire electrodes for shape-memory polymer light-emitting diodes," *Advanced Materials*, vol. 23, no. 5, pp. 664–668, 2011.
- [31] F. S. Morgenstern, D. Kabra, S. Massip, T. J. Brenner, P. E. Lyons, J. N. Coleman, and R. H. Friend, "Ag-nanowire films coated with zno nanoparticles as a transparent electrode for solar cells," *Applied Physics Letters*, vol. 99, no. 18, p. 242, 2011.
- [32] X. Lan, J. Bai, S. Masala, S. M. Thon, Y. Ren, I. J. Kramer, S. Hoogland, A. Simchi, G. I. Koleilat, D. Paz-Soldan, *et al.*, "Self-assembled, nanowire network

- electrodes for depleted bulk heterojunction solar cells," *Advanced Materials*, vol. 25, no. 12, pp. 1769–1773, 2013.
- [33] D. Angmo, T. R. Andersen, J. J. Bentzen, M. Helgesen, R. R. SÃžndergaard, M. JÃžrgensen, J. E. CarlÃ©, E. Bundgaard, and F. C. Krebs, "Roll-to-roll printed silver nanowire semitransparent electrodes for fully ambient solution-processed tandem polymer solar cells," *Advanced Functional Materials*, vol. 25, no. 28, pp. 4539–4547, 2015.
- [34] A. R. Madaria, A. Kumar, F. N. Ishikawa, and C. Zhou, "Uniform, highly conductive, and patterned transparent films of a percolating silver nanowire network on rigid and flexible substrates using a dry transfer technique," *Nano Research*, vol. 3, no. 8, pp. 564–573, 2010.
- [35] S. De and J. N. Coleman, "The effects of percolation in nanostructured transparent conductors," *MRS Bulletin*, vol. 36, pp. 774–781, 10 2011.
- [36] C. Celle, C. Mayousse, E. Moreau, H. Basti, A. Carella, and J.-P. Simonato, "Highly flexible transparent film heaters based on random networks of silver nanowires," *Nano Research*, vol. 5, no. 6, pp. 427–433, 2012.
- [37] S. Sorel, D. Bellet, and J. N. Coleman, "Relationship between material properties and transparent heater performance for both bulk-like and percolative nanostructured networks," *ACS nano*, vol. 8, no. 5, pp. 4805–4814, 2014.
- [38] O. Ergun, S. Coskun, Y. Yusufoglu, and H. E. Unalan, "High-performance, bare silver nanowire network transparent heaters," *Nanotechnology*, vol. 27, no. 44, p. 445708, 2016.
- [39] K. Takei, T. Takahashi, J. C. Ho, H. Ko, A. G. Gillies, P. W. Leu, R. S. Fearing, and A. Javey, "Nanowire active-matrix circuitry for low-voltage macroscale artificial skin," *Nature materials*, vol. 9, no. 10, p. 821, 2010.
- [40] J. Wang, J. Jiu, T. Araki, M. Nogi, T. Sugahara, S. Nagao, H. Koga, P. He, and K. Suganuma, "Silver nanowire electrodes: conductivity improvement

- without post-treatment and application in capacitive pressure sensors," *Nano-Micro Letters*, vol. 7, no. 1, pp. 51–58, 2015.
- [41] I. Chang, T. Park, J. Lee, H. B. Lee, S. H. Ko, and S. W. Cha, "Flexible fuel cell using stiffness-controlled endplate," *international journal of hydrogen energy*, vol. 41, no. 14, pp. 6013–6019, 2016.
- [42] I. Chang, T. Park, J. Lee, H. B. Lee, S. Ji, M. H. Lee, S. H. Ko, and S. W. Cha, "Performance enhancement in bendable fuel cell using highly conductive ag nanowires," *international journal of hydrogen energy*, vol. 39, no. 14, pp. 7422–7427, 2014.
- [43] I. Chang, T. Park, J. Lee, M. H. Lee, S. H. Ko, and S. W. Cha, "Bendable polymer electrolyte fuel cell using highly flexible ag nanowire percolation network current collectors," *Journal of Materials Chemistry A*, vol. 1, no. 30, pp. 8541–8546, 2013.
- [44] C. Pozrikidis, *An Intrdution to Grids, Graphs and Networks*. Oxford University Press, 2014.
- [45] J. Cserti, "Application of the lattice green's function for calculating the resistance of an infinite network of resistors," *Am. J. Phys.*, vol. 68, p. 896, 2000.
- [46] G. E. Pike and C. H. Seager, "Percolation and conductivity: A computer study. i," *Phys. Rev. B*, vol. 10, pp. 1421–1434, Aug 1974.
- [47] S. R. Broadbent and J. M. Hammersley, "Percolation processes: I. crystals and mazes," in *Mathematical Proceedings of the Cambridge Philosophical Society*, vol. 53, pp. 629–641, Cambridge University Press, 1957.
- [48] J. Li and S. Zhang, "Finite-size scaling in stick percolation," *Phys. Rev. E*, vol. 80, p. 040104, Oct 2009.

- [49] M. Žeželj and I. Stanković, "From percolating to dense random stick networks: Conductivity model investigation," *Phys. Rev. B*, vol. 86, p. 134202, Oct 2012.
- [50] H. G. Manning, A. T. Bellew, C. G. Rocha, F. Niosi, C. O'Callaghan, S. Biswas, P. Flowers, B. J. Wiley, J. T. Holmes, M. S. Ferreira, and J. J. Boland, "Emergence of winner-takes-all connectivity paths in random nanowire networks," *to appear*, 2017.
- [51] L. Chua, "Memristor-the missing circuit element," *IEEE Trans. Circuit Theory*, vol. 18, p. 507, 1971.
- [52] L. Chua, "Resistance switching memories are memristors," *Applied Physics A*, vol. 102, no. 4, pp. 765–783, 2011.
- [53] L. O. Chua and S. M. Kang, "Memristive devices and systems," *Proceedings of the IEEE*, vol. 64, no. 2, pp. 209–223, 1976.
- [54] D. B. Strukov, G. S. Snider, D. R. Stewart, and R. S. Williams, "The missing memristor found," *Nature*, vol. 453, no. 7191, p. 80, 2008.
- [55] J. J. Yang, D. B. Strukov, and D. Stewart R., "Memristive devices for computing," *Nature Nanotechnology*, vol. 8, p. 13, 2013.
- [56] I. Valov and M. N. Kozicki, "Cation-based resistance change memory," *Journal of Physics D: Applied Physics*, vol. 46, no. 7, p. 074005, 2013.
- [57] E. W. Lim and R. Ismail, "Conduction mechanism of valence change resistive switching memory: a survey," *Electronics*, vol. 4, p. 586, 2015.
- [58] B. J. Choi, A. C. Torrezan, K. J. Norris, F. Miao, J. P. Strachan, M.-X. Zhang, D. A. A. Ohlberg, N. P. Kobayashi, J. J. Yang, and R. S. Williams, "Electrical performance and scalability of pt dispersed sio₂ nanometallic resistance switch," *Nano Letters*, vol. 13, no. 7, pp. 3213–3217, 2013. PMID: 23746124.

- [59] W.-C. Chien, Y.-C. Chen, F.-M. Lee, Y.-Y. Lin, E.-K. Lai, Y.-D. Yao, J. Gong, S.-F. Horng, C.-W. Yeh, S.-C. Tsai, *et al.*, "A novel ni/wox/w resistive random access memory with excellent retention and low switching current," *Japanese Journal of Applied Physics*, vol. 50, no. 4S, p. 04DD11, 2011.
- [60] X. Wang, Z. Fang, X. Li, B. Chen, B. Gao, J. Kang, Z. Chen, A. Kamath, N. Shen, N. Singh, *et al.*, "Highly compact 1t-1r architecture (4f 2 footprint) involving fully cmos compatible vertical gaa nano-pillar transistors and oxide-based rram cells exhibiting excellent nvm properties and ultra-low power operation," in *Electron Devices Meeting (IEDM), 2012 IEEE International*, pp. 20–6, IEEE, 2012.
- [61] M.-J. Lee, C. B. Lee, D. Lee, S. R. Lee, M. Chang, J. H. Hur, Y.-B. Kim, C.-J. Kim, D. H. Seo, S. Seo, U.-I. Chung, I.-K. Yoo, and K. Kim, "A fast, high-endurance and scalable non-volatile memory device made from asymmetric ta₂o₅-x/tao₂-x bilayer structures," *Nat Mater*, vol. 10, pp. 625–630, 2011.
- [62] R. Waser and M. Aono, "Nanoionics-based resistive switching memories," *Nature materials*, vol. 6, no. 11, p. 833, 2007.
- [63] R. Tetzlaff, ed., *Memristors and memristive systems*. Springer-Verlag New York, 2014.
- [64] D. S. Jeong, R. Thomas, R. Katiyar, K. H. Scott, J., A. Petraru, and C. S. Hwang, "Emerging memories: resistive switching mechanisms and current status," *Reports on Progress in Physics*, vol. 75, p. 076502, 2012.
- [65] H. G. Manning, S. Biswas, J. D. Holmes, and J. J. Boland, "Nonpolar resistive switching in ag@tio₂ core-shell nanowires," *ACS Applied Materials & Interfaces*, vol. 9, p. 38959, 2017.
- [66] R. Waser, R. Dittmann, G. Staikov, and K. Szot, "Redox-based resistive switching memories - nanoionic mechanisms, prospects, and challenges," *Advanced Materials*, vol. 21, no. 25-26, pp. 2632–2663, 2009.

- [67] Y. Yang, P. Gao, S. Gaba, T. Chang, X. Pan, and W. Lu, "Observation of conducting filament growth in nanoscale resistive memories," *Nature communications*, vol. 3, p. 732, 2012.
- [68] E. Gale, "Tio₂-based memristors and reram: materials, mechanisms and models (a review)," *Semiconductor Science and Technology*, vol. 29, no. 10, p. 104004, 2014.
- [69] D. Ielmini, R. Bruchhaus, and R. Waser, "Thermochemical resistive switching: materials, mechanisms, and scaling projections," *Phase Transitions*, vol. 84, no. 7, pp. 570–602, 2011.
- [70] B. Sengupta and M. B. Stemmler, "Power consumption during neuronal computation," *Proc. IEEE*, vol. 102, p. 738, 2014.
- [71] G. Indiveri, B. Linares-Barranco, R. Legenstein, G. Deligeorgis, and T. Prodromakis, "Integration of nanoscale memristor synapses in neuromorphic computing architectures," *Nanotechnology*, vol. 24, p. 384010, 2013.
- [72] M. Prezioso, F. Merrikh-Bayat, B. D. Hoskins, G. C. Adam, K. K. Likharev, and D. B. Strukov, "Training and operation of an integrated neuromorphic network based on metal-oxide memristors," *Nature*, vol. 521, p. 61, 2015.
- [73] D. Querlioz, O. Bichler, P. Dollfus, and C. Gamrat, "Immunity to device variations in a spiking neural network with memristive nanodevices," *IEEE Transactions on Nanotechnology*, vol. 12, pp. 288–295, May 2013.
- [74] A. Calimera, E. Macii, and M. Poncino, "The human brain project and neuromorphic computing," *Functional Neurology*, vol. 28, p. 191, 2013.
- [75] Z. Ye, S. H. M. Wu, and T. Prodromakis, "Computing shortest paths in 2d and 3d memristive networks," in *Memristor Networks*, pp. 537–552, Springer, 2014.

- [76] P. Gkoupidenis, D. A. Koutsouras, and G. G. Malliaras, "Neuromorphic device architectures with global connectivity through electrolyte gating," *Nature Communications*, vol. 8, p. 15448, 2017.
- [77] S. Kumar, J. P. Strachan, and R. S. Williams, "Chaotic dynamics in nanoscale nbo 2 mott memristors for analogue computing," *Nature*, vol. 548, no. 7667, p. 318, 2017.
- [78] S. Yu, B. Gao, Z. Fang, H. Yu, J. Kang, and H.-S. P. Wong, "Stochastic learning in oxide binary synaptic device for neuromorphic computing," *Frontiers in neuroscience*, vol. 7, p. 186, 2013.
- [79] C. G. Rocha, H. G. Manning, C. O'Callaghan, C. Ritter, A. T. Bellew, J. J. Boland, and M. S. Ferreira, "Ultimate conductivity performance in metallic nanowire networks," *Nanoscale*, vol. 7, p. 13011, 2015.
- [80] P. N. Nirmalraj, A. T. Bellew, A. P. Bell, J. A. Fairfield, E. K. McCarthy, C. J. O'Kelly, L. F. C. Pereira, S. Sorel, D. Morosan, J. N. Coleman, M. S. Ferreira, and J. J. Boland, "Manipulating connectivity and electrical conductivity in metallic nanowire networks," *Nano Letters*, vol. 12, p. 5966, 2012.
- [81] S. Kirkpatrick, "Percolation and conduction," *Rev. Mod. Phys.*, vol. 45, p. 574, 1973.
- [82] I. Balberg, N. Binenbaum, and C. Anderson, "Critical behavior of the two-dimensional sticks system," *Physical Review Letters*, vol. 51, no. 18, p. 1605, 1983.
- [83] S. M. Bergin, Y.-H. Chen, A. R. Rathmell, P. Charbonneau, Z.-Y. Li, and B. J. Wiley, "The effect of nanowire length and diameter on the properties of transparent, conducting nanowire films," *Nanoscale*, vol. 4, pp. 1996–2004, 2012.
- [84] J. Heitz, Y. Leroy, L. HÃ©brard, and C. Lallement, "Theoretical characterization of the topology of connected carbon nanotubes in random networks," *Nanotechnology*, vol. 22, no. 34, p. 345703, 2011.

- [85] C. O'Callaghan, C. G. da Rocha, H. G. Manning, J. J. Boland, and M. S. Ferreira, "Effective medium theory for the conductivity of disordered metallic nanowire networks," *Physical Chemistry Chemical Physics*, vol. 18, no. 39, pp. 27564–27571, 2016.
- [86] S. Sorel, P. E. Lyons, S. De, J. C. Dickerson, and J. N. Coleman, "The dependence of the optoelectrical properties of silver nanowire networks on nanowire length and diameter," *Nanotechnology*, vol. 23, no. 18, p. 185201, 2012.
- [87] J. Hicks, A. Behnam, and A. Ural, "Resistivity in percolation networks of one-dimensional elements with a length distribution," *Physical Review E*, vol. 79, no. 1, p. 012102, 2009.
- [88] R. M. Mutiso, M. Sherrott, A. Rathmell, B. Wiley, and K. Winey, "Integrating simulations and experiments to predict sheet resistance and optical transmittance in nanowire films for transparent conductors," *ACS Nano*, vol. 7, no. 9, pp. 7654–7663, 2013.
- [89] J. A. Fairfield, C. Ritter, A. T. Bellew, E. K. McCarthy, M. S. Ferreira, and J. J. Boland, "Effective electrode length enhances electrical activation of nanowire networks: Experiment and simulation," *ACS Nano*, vol. 8, no. 9, pp. 9542–9549, 2014. PMID: 25153920.
- [90] C. Pozrikidis, *An introduction to grids, graphs and networks*. Oxford University Press, 2014.
- [91] P. N. Nirmalraj, P. E. Lyons, S. De, J. N. Coleman, and J. J. Boland, "Electrical connectivity in single-walled carbon nanotube networks," *Nano letters*, vol. 9, no. 11, pp. 3890–3895, 2009.
- [92] A. T. Bellew, H. G. Manning, C. G. Rocha, M. S. Ferreira, and J. J. Boland, "Resistance of single ag nanowire junctions and their role in the conductivity of nanowire networks," *ACS Nano*, vol. 9, p. 11422, 2015.

- [93] B. Hwang, H.-A.-S. Shin, T. Kim, Y.-C. Joo, and S. M. Han, "Highly reliable ag nanowire flexible transparent electrode with mechanically welded junctions," *Small*, vol. 10, no. 16, pp. 3397–3404, 2014.
- [94] L. Hu, H. S. Kim, J.-Y. Lee, P. Peumans, and Y. Cui, "Scalable coating and properties of transparent, flexible, silver nanowire electrodes," *ACS Nano*, vol. 4, no. 5, pp. 2955–2963, 2010. PMID: 20426409.
- [95] L. Hu, D. Hecht, and G. Grüner, "Percolation in transparent and conducting carbon nanotube networks," *Nano letters*, vol. 4, no. 12, pp. 2513–2517, 2004.
- [96] A. Behnam and A. Ural, "Computational study of geometry-dependent resistivity scaling in single-walled carbon nanotube films," *Phys. Rev. B*, vol. 75, p. 125432, Mar 2007.
- [97] J. F. Ramaley, "Buffon's noodle problem," *The American Mathematical Monthly*, vol. 76, no. 8, pp. 916–918, 1969.
- [98] D. J. Watts and S. H. Strogatz, "Collective dynamics of 'small-world'networks," *nature*, vol. 393, no. 6684, pp. 440–442, 1998.
- [99] L. A. Braunstein, S. V. Buldyrev, R. Cohen, S. Havlin, and H. E. Stanley, "Optimal paths in disordered complex networks," *Physical review letters*, vol. 91, no. 16, p. 168701, 2003.
- [100] M. Lagrange, T. Sannicolo, D. Muñoz-Rojas, B. G. Lohan, A. Khan, M. Anikin, C. Jiménez, F. Bruckert, Y. Bréchet, and D. Bellet, "Understanding the mechanisms leading to failure in metallic nanowire-based transparent heaters, and solution for stability enhancement," *Nanotechnology*, vol. 28, no. 5, p. 055709, 2016.
- [101] J. Zhao, H. Sun, S. Dai, Y. Wang, and J. Zhu, "Electrical breakdown of nanowires," *Nano letters*, vol. 11, no. 11, pp. 4647–4651, 2011.

- [102] J. A. Fairfield, C. G. Rocha, C. O'Callaghan, M. S. Ferreira, and J. J. Boland, "Co-percolation to tune conductive behaviour in dynamical metallic nanowire networks," *Nanoscale*, vol. 8, p. 18516, 2016.
- [103] F. Hartmann, P. Maier, M. R. S. Dias, S. Göpfert, L. K. Castelano, M. Emmerling, C. Schneider, S. Höfling, M. Kamp, Y. V. Pershin, G. E. Marques, V. Lopez-Richard, and L. Worschech, "Nanoscale tipping bucket effect in a quantum dot transistor-based counter," *Nano Letters*, vol. 17, p. 2273, 2017.
- [104] P. Maier, F. Hartmann, M. R. S. Dias, M. Emmerling, C. Schneider, L. K. Castelano, M. Kamp, G. E. Marques, V. Lopez-Richard, L. Worschech, and S. Hofling, "Mimicking of pulse shape-dependent learning rules with a quantum dot memristor," *Journal of Applied Physics*, vol. 120, p. 134503, 2016.
- [105] T. Wakrim, C. Vallée, P. Gonon, C. Mannequin, and A. Sylvestre, "From memristor to memimpedance device," *Appl. Phys. Lett.*, vol. 108, p. 053502, 2016.
- [106] S. Liu, N. Wu, A. Ignatiev, and J. Li, "Electric-pulse-induced capacitance change effect in perovskite oxide thin films," *Journal of Applied Physics*, vol. 100, p. 056101, 2006.
- [107] A. V. Avizienis, H. O. Sillin, C. Martin-Olmos, H. H. Shieh, M. Aono, A. Z. Stieg, and J. K. Gimzewski, "Neuromorphic atomic switch networks," *PLoS One*, vol. 7, p. e42772, 2012.
- [108] E. C. Demis, R. Aguilera, K. Scharnhorst, M. Aono, A. Z. Stieg, and J. K. Gimzewski, "Nanoarchitectonic atomic switch networks for unconventional computing," *Japanese Journal of Applied Physics*, vol. 55, p. 1102B2, 2016.
- [109] K.-H. Kim, S. Gaba, D. Wheeler, J. M. Cruz-Albrecht, T. Hussain, N. Srinivasa, and W. Lu, "A functional hybrid memristor crossbar-array/cmos system for data storage and neuromorphic applications," *Nano Lett.*, vol. 12, p. 389, 2012.
- [110] G. S. Snider, "Self-organized computation with unreliable, memristive nanodevices," *Nanotechnology*, vol. 18, p. 365202, 2007.